INVESTIGATION OF HIGH-TEMPERATURE OXIDATION RESISTANCE MECHANISM OF CERAMIC COATINGS VIA MICROSTRUCTURE ANALYSIS

Yi Shen

Dissertation

In partial fulfillment for the Ph.D

degree in Materials Science and

Engineering at the University of Texas

at Arlington

August 2020

ABSTRACT

Recent developments of ceramic coatings deposited using magnetron reactive sputtering show that these films exhibited superior high-temperature oxidation resistance along with other desirable properties such as high hardness, optical transparency and good electrical conductivity. Detailed microstructure study of these films annealed to high temperatures using transmission electron microscopy (TEM) is deemed necessary as it provides an intuitive vision on the behavior of the materials at elevated temperature, which is essential to further improve their high-temperature oxidation resistance. In this study, Hf-B-Si-C-N films with various compositions that were annealed to various temperatures in both helium and air were subjected to detailed TEM study. The results showed that while as-deposited films exhibited amorphous structure, annealing in air resulted in the formation of an oxide layer on top and the original film underneath. Meanwhile, annealing in helium led to partial recrystallization of the film into a nanocrystalline composite structure without oxidation. It was also observed that the addition of nitrogen helped the amorphization of the film at high temperatures and could potentially improve the oxidation resistance. Further improved design of the Hf-B-Si-C-N films can be accomplished with the addition of rare earth elements including yttrium and holmium, as well as tuning of silicon and boron content. The effects of these changes were also subjected to TEM microstructure analysis, in an effort to uncover the high temperature oxidation resistance mechanism. It is concluded that $Hf_6B_{21}Si_{19}C_4N_{47}$ film, which exhibited superior thermal stability at high temperatures, had a relatively smooth and defect-

free interface between the oxide layer and bottom layer, which in turn offer the best oxidation resistance among the films we have studied.

Chapter 1

INTRODUCTION

1.1 Research Motivation

Ultra-high temperature ceramics (UHTCs) are usually referred as transition metal-based borides, carbides, nitrides and their composites as these materials exhibit a combination of desirable properties such as high hardness, high melting point, superior oxidation and corrosion resistance at high temperature and high thermal stability [1-10]. Recently, development of such materials has been focused on ZrB_2-SiC and HfB_2-SiC based UHTCs since they could provide possible solution to surface protection in severe environment due to their high hardness and good oxidation resistance at elevated temperatures (>1000 °C) [11-19], making them more promising candidates for applications including refractory linings, high-temperature electrodes, microelectronics, high-speed cutting tools and the wing leading edges and sharp noses of the hypersonic re-entry vehicles [2-5]. However, as the demand for surface protection against corrosion and oxidation in extreme environment keeps increasing, new types of UHTCs-based thin-film materials are required to meet the harsh requirement. One of the crucial aspects in the development of such materials is to understand the behavior of these materials as they are exposed to such extreme environment. Comprehensive microstructure analysis using high-resolution transmission electron microscopy (HRTEM) coupled with selected-area electron diffraction (SAED) could be a powerful tool to investigate this specific topic as it

extracts intuitive and detailed morphological and crystallographic information from annealed materials in the scale of a few nanometers. Such precise analysis enables better understanding of how different elements and phases from the original materials evolve to develop new microstructure at elevated temperatures in oxidizing environment, which would help develop the oxidation mechanism thus bridge the relation between coating deposition parameters and oxidation resistance. In this way, high-temperature oxidation resistance of the film could be improved by more precisely defining the coating composition.

1.2 Research Objectives

As mentioned above comprehensive microstructure analysis plays a fundamental role of developing new types of surface protective coatings with superior oxidation resistance. The overall objective of this research is to develop a better understanding of the impact that elemental composition, phase composition and microstructure in the coatings have on the thermal and chemical stability of the film at high temperatures (1500 ^{o}C or above) which could be used for further enhancing the coatings' performance. To reach this, several films based on the Hf-Si-B-C-N system that were deposited via magnetron reactive sputtering and annealed to various high temperatures in different gas atmospheres were subjected to TEM microstructure analysis. The objectives of this study are as follows:

1. To investigate the microstructure evolution of new multi-functional Hf-B-Si-C-N coatings annealed to various temperatures in air and helium.
2. To study the effect of elemental composition on the microstructure and various properties of the coating:
    a) To study the effect of nitrogen and silicon content on the microstructure and high-temperature oxidation resistance of new multi-functional Hf-B-Si-C-N coatings.
    b) To explore the possible impact of yttrium and holmium addition to the existing Hf-B-Si-C-N system on the microstructure and high-temperature oxidation resistance of the coatings, as these elements could contribute to better oxidation resistance in some UHTCs

applications.

3. Based on the findings, develop an overall understanding of the oxidation resistance mechanism for designing new types of coatings with better high-temperature oxidation resistance.

Chapter 2

LITERATURE REVIEW

2.1 Recent Development of UHTC coatings

Ultra-High Temperature Ceramics are usually defined as compounds that have melting points above 3000 ^{o}C [3, 4]. Very few materials are able to meet this extreme criterion, and for real-world engineering applications, melting point is only one of the properties that these materials have to meet. For example, mechanical strength of the material has to be good enough to maintain the structural integrity at both room temperature and high temperature. Oxidation resistance, describing how the material will react in an oxidizing environment to maintain the chemical and structural stability, also needs to be addressed. As a result, choices of UHTC materials are further narrowed. Silicon-based refractory materials such as SiC and Si_3N_4 have good oxidation resistance up to 1700 °C and see a wide variety of applications [3]. However, active oxidation, which is the direct formation of gaseous SiO instead of a protective SiO_2 layer, can occur at very high temperatures thus hinders the application at such temperatures. Furthermore, SiC and Si_3N_4 will undergo an oxidation and a volatilization reaction in a water-vapor-containing high-temperature environment described by Eq. 1 and 2 (using SiC as an example):

$$SiC + 3H_2O\ (g) = SiO_2 + 3H_2\ (g) + CO\ (g) \quad (1)$$

$$SiO_2 + 2H_2O\ (g) = Si\ (OH)_4\ (g) \quad (2)$$

and as a result, SiC and Si_3N_4 will lose the SiO_2 protection layer and erode continuously

[20-22]. A proposed solution to counter the issue involves the addition of rare earth element to form an environment barrier coating (EBC), which would be discussed in following paragraphs. On the other hand, oxides generally are considered suitable for oxidizing environment, however, they suffer from poor thermal shock resistance due to high thermal expansion and low thermal conductivity [3]. In some cases, materials with high melting point will form oxides with lower melting point and low melting viscosities, significant mass loss due to the vaporization of oxides would occur in these cases and limit the protective effect of oxide layer, an example of which is TiB_2 with melting point at 3230 °C and TiO_2 at 1840 °C [3].

Eventually, it turns out that borides, carbides and nitrides of some Group IV & V elements, as well as the mixture of these compounds, would satisfy the most requirement and become the most ideal candidates of UHTCs. Significant efforts have been put into the synthesis, characterization, and optimization of these materials. Among them, diborides of zirconium and hafnium (ZrB_2 and HfB_2) have attracted lots of attention since the development of UHTCs started to grow rapidly in the 1960s, driven by the demand for such materials in potential aerospace applications [2-4]. Both ZrB_2 and HfB_2 demonstrate a unique combination of properties including high melting point, good chemical stability, high electrical and thermal conductivities and good corrosion resistance, largely due to the fundamental aspect of crystal structures of these two diborides [2, 3]. ZrB_2 and HfB_2 crystals both exist in AlB_2 hexagonal structure, with Zr or Hf atoms forming hexagonal close-packed planes and boron atoms forming 2D-graphite like rings in-between, and strong B-B (boron-boron) and

M-B (metal-boron) bonds ensure the materials' high hardness and good thermal stability [2]. Apart from that, oxidation behavior of ZrB_2 and HfB_2 was also investigated extensively. at static oxidation environment, both diborides will undergo stoichiometric oxidation, described by Eq. 3 and 4:

$$ZrB_2\ (c) + \frac{5}{2}O_2\ (g) = ZrO_2\ (c) + B_2O_3\ (l) \qquad (3)$$

$$HfB_2\ (c) + \frac{5}{2}O_2\ (g) = HfO_2\ (c) + B_2O_3\ (l) \qquad (4)$$

and at temperatures below 1100 °C ZrO_2 (or HfO_2) and B_2O_3 will form a continuous protective layer that covers the surface of borides [8, 12, 23]. Oxidation rate is limited by the diffusion of O_2 through B_2O_3. When the temperature increases to between 1100 and 1400 °C, B_2O_3 evaporation starts to become rapid, leading to significant mass loss and a porous ZrO_2 (or HfO_2) oxide layer, and as temperature keeps increasing, the oxide layer loses its protective ability and rapid oxidation of diborides will commence [3, 10].

Numerous efforts were put into the improvement of oxidation resistance of Zr- and Hf-based diborides, and one of the most successful outcomes is the ZrB_2-SiC (or HfB_2-SiC) composite material [2, 5, 9-13, 16-19]. Experimental results showed that 20 vol% SiC in ZrB_2-SiC (or HfB_2-SiC) provides best oxidation resistance performance in conditions similar to hypersonic re-entry environment, compared to compositions with 5 to 50 vol% [2, 10]. The addition of SiC greatly enhances the oxidation resistance by forming a borosilicate glass layer at temperatures above 1350 °C. This borosilicate layer helps to reduce the diffusivity of oxygen and limit the release of B_2O_3 from the material due to its higher liquidus temperature and viscosity, offering superior protection up to at least 1600 °C compared to pure borides. A schematic illustration of

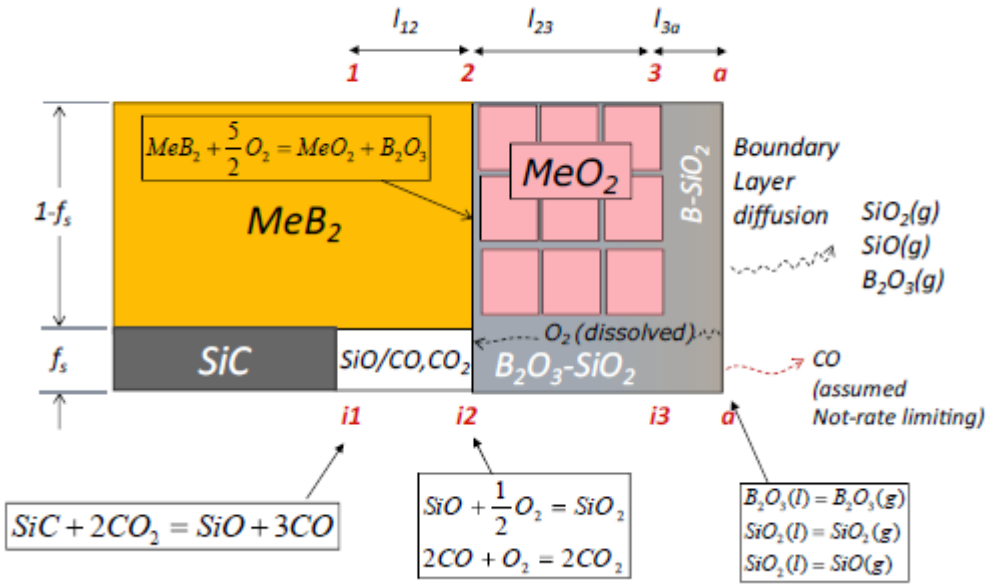

Fig. 1 A schematic illustration of oxidation reaction, product and morphology of MeB_2-SiC refractory material used by Parthasarathy *et al.* [24].

the morphology and oxidation products was offered by Parthasarathy *et al.* in their model trying to explain the oxidation kinetics of SiC-containing refractory diborides, as shown in Fig. 1 [24]. The base material is MeB_2-SiC (Me=Zr or Hf) on the left side, while f_s represents the volume fraction of SiC content. And the scale consists of separate (in cross-section) MeO_2 grains with continuous porous filled by borosilicate glass. Molecular oxygen from the ambient dissolves in borosilicate, diffuses across the glassy layer and through the channels in-between MeO_2 grains and eventually reacts with MeB_2 at interface *i2*, as well as SiC via CO and CO_2 medium. CO, which is the final gaseous product of SiC oxidation, will bubble through the glassy layer and release from the material. The open structure and viscosity of borosilicate glass enable the release of gaseous species (including CO and SiO) without catastrophic failure of the structure integrity.

Overall, ZrB_2-SiC (or HfB_2-SiC) exhibit superior oxidation resistance behavior,

especially in an environment similar to operating conditions of hypersonic re-entry vehicles. Other materials including zirconium and hafnium based carbides and nitrides were also investigated [3, 10]. Carbides, having extremely high melting temperatures exceeding even corresponding diborides due to strong interatomic bonds, exhibit excellent oxidation resistance at above 1800 °C, however, at temperatures lower than 1500 °C, the material is vulnerable to oxidizing environment due to the inability to form dense oxide scale on the surface. The oxides tend to spall off from the base material, causing a porous scale. Similar behavior was found on nitrides as they are unable to form a glassy protective layer that slows down the O_2 diffusion on top of the base material as well [3]. Carbides and nitrides see potential applications when higher thermal and mechanical loads are encountered like nozzle lines and throats. Adding nitrogen in borides also improves the tribological properties in thin-film applications [1].

2.2 Rare Earth Additives and Optimization of UHTCs

Extensive researches have demonstrated the superior oxidation resistance of ZrB_2-SiC (HfB_2-SiC) UHTCs. However, it never stops the efforts to further improve the performance of these materials. Both ZrB_2-SiC and HfB_2-SiC lose their excellent oxidation resistance at temperatures above 1800 °C [12, 25]. The reason behind is that the evaporation of B_2O_3 and SiO_2 becomes so violent that the borosilicate glassy layer starts to recede inwards, leaving refractory metal oxides with porous surface that is susceptible to oxygen permeation.

Various methods were investigated to improve the oxidation resistance and adding additives to the base materials is deemed to be a promising approach. Attempts were made to increase the temperature and viscosity of the glass scale by adding various additives such as CrB_2, TiB_2, TaB_2, NbB_2 and VB_2 [10, 26]. Increased viscosity, as well as increased temperature, will limit the boria evaporation, and also help decrease the diffusion rate of oxygen. The improvement eventually comes from the fact that at elevated temperatures, the aforementioned additives will oxidize and the borosilicate glass containing them will become immiscible. Strong tendency to phase transformation leads to increased liquid temperature and viscosity, effectively extends the temperature range of glass scale. Another promising approach of modifying UHTCs is to promote the densification of metal oxide porous structure by liquid phase sintering, which is done by adding WC or WB into the system. At temperatures above 1280 °C, liquidous WO_3 can form and enhance the densification of both HfO_2 and ZrO_2, effectively eliminating the fast diffusion path of oxygen [25, 27].

On the other hand, the proposal of developing solid refractory scale was also considered, and that's when rare earth elements come into play. LaB_6-containing ZrB_2-SiC was reported to have improved oxidation resistance due to the formation of a compact scale that reduce spalling and cracking [28]. Jayaseelan *et al.* also have demonstrated that by adding LaB_6, La_2O_3 and Gd_2O_3, the oxidation resistance of ZrB_2-SiC could be improved by formation of $RE_2Zr_2O_7$ which has pyrochlore structure and very high melting point (T_m > 2300 °C). Furthermore, formation of RE-zirconate is expansive and will be able to fill the pores generated by evaporation of glass scale and form a dense solid oxide scale which will help reduce the diffusivity of O_2 [29]. Other rare earth addition including Y and Yb was also reported to improve the densification of ZrB_2-SiC, as well as the mechanical properties of the material, but the oxidation resistance was not investigated [30, 31]. Meanwhile, extensive studies were carried out on the potential application of rare earth silicate (RE silicate) on EBCs to protect Si-based ceramics. RE silicates demonstrate some excellent mechanical and thermal properties including good phase and chemical stability, low thermal conductivity and coefficient of thermal expansion (CTE) at elevated temperatures in water-vapor containing environment [34-38]. Overall, it is a promising approach to add rare earth elements in UHTCs, especially in thin films, due to the effect of improving both the thermal properties and oxidation resistance of the material.

Chapter 3

RESEARCH PLAN

As a broad on-going project, the collaboration work between Professor Vlček's research group in the Department of Physics and NTIS – European Center of Excellence, University of West Bohemia, Czech Republic and SaNEL lab and CCMB in the Department of Materials Science and Engineering, UT Arlington have demonstrated that Hf-B-Si-C films could reach high hardness (up to 37 GPa), high electrical conductivity (electrical resistivity on the order of 10^{-6} Ωm) and good oxidation resistance in air (up to 800 °C) [39, 40]. It was also demonstrated that Si-B-C-N films, with the addition of nitrogen, maintained exceptional thermal stability in high temperature environment (up to 1700 °C) [41-45]. In a more recent work, nitrogen was incorporated into the Hf-B-Si-C system in order to limit the release of boron and improve the overall stability of the film beyond 1000 °C and the results showed that the new $Hf_7B_{23}Si_{17}C_4N_{45}$ films exhibited superior oxidation resistance in air up to 1600 °C [46, 47]. The films in these studies were deposited using magnetron reactive sputtering by professor Vlček's research group, while detailed microstructure analysis was conducted at UT Arlington. Research in this topic will carry on in this way and the present research will be divided into two phases: 1. Microstructure analysis of new multifunctional Hf-B-Si-C-N films. 2. Microstructure analysis of new Hf-B-Si-RE-C-N films.

3.1 Microstructure Analysis of New Multifunctional Hf-B-Si-C-N Films

In this phase, a series of new Hf-B-Si-C-N films were deposited by magnetron reactive sputtering using a single B_4C-Hf-Si target in an Ar-N_2 gas mixture. The target in use has a fixed fraction of 65% B_4C + 15% Hf + 20% Si in the erosion area and the working pressure was set at 0.5 Pa which contains 15% N_2, resulting the final film composition being $Hf_7B_{23}Si_{22}C_6N_{40}$ (determined by Rutherford backscattering spectroscopy). The films were then annealed to various temperatures in static air from room temperature to 1100, 1200, 1300, 1400, 1500 and 1600 °C, as well as in helium from room temperature to 1100, 1200, 1300 and 1400 °C. The original as-deposited film and the annealed films were subjected to comprehensive TEM and SAED study to investigate the microstructure evolution of $Hf_7B_{23}Si_{22}C_6N_{40}$ films at elevated temperatures in air and helium. This would help better understand the high-temperature behavior of Hf-B-Si-C-N thin-film system. The second goal is to investigate the effect of varying nitrogen fraction in the gas mixture on the microstructure and oxidation resistance of the film. The previously mentioned $Hf_7B_{23}Si_{22}C_6N_{40}$ film and a new $Hf_6B_{21}Si_{19}C_4N_{47}$ film, which was deposited using 25% N_2 in the gas mixture instead of 15%, were annealed to 1500 °C in air. Both films were subjected to XRD, TEM and SAED analysis. Results of the study are expected to contribute to better understanding of the oxidation mechanism and development of new high-temperature oxidation-resistant coatings.

3.2 Microstructure Analysis of New Hf-B-Si-RE-C-N Films

In phase two of the study, two films with rare earth element addition, $Hf_6B_{12}Si_{29}Y_2C_2N_{45}$ and $Hf_5B_{13}Si_{25}Ho_3C_2N_{48}$, together with two films without RE addition, $Hf_7B_{10}Si_{32}C_2N_{44}$ and $Hf_6B_{10}Si_{31}C_2N_{50}$, all of which were annealed to 1500 °C in air, were subjected to detailed microstructure analysis using TEM and SAED. The films without additions were deposited using a target that has 30% B_4C + 20% Hf + 50% Si in the erosion area and a gas mixture of 75% Ar + 25% N_2 (for $Hf_7B_{10}Si_{32}C_2N_{44}$ film) or 50% Ar + 50% N_2 (for $Hf_6B_{10}Si_{31}C_2N_{50}$ film). Compared to the previous $Hf_7B_{23}Si_{22}C_6N_{40}$ and $Hf_6B_{21}Si_{19}C_4N_{47}$ film, the new films were deposited with higher Si and lower B content in the target composition, which led to the corresponding difference in the film composition. One of the key objectives is to investigate the effect of Si vs B ratio on the oxidation resistance of Hf-B-Si-C-N films. Meanwhile, the films with rare earth addition were deposited using a target that has 30% B_4C + 15% Hf + 50% Si + 5% Y or Ho in the erosion area and a gas mixture of 75% Ar + 25% N_2. Rare earth monosilicates which contain Y and Ho are ideal candidates for thermal barriers [38]. Thus, the key objective of this study is to find out if such thermal barriers formed in the oxidation of Hf-B-Si-RE-C-N films and how it contributed to the oxidation resistance. Detailed microstructure of two films with additions was analyzed. In the end, by combining the data from the two phases of the study, we are to develop an oxidation mechanism of Hf-B-Si-C-N thin-film system and explain the impact of Si, N and RE element on the oxidation resistance.

Chapter 4

CURRENT RESULTS AND DISCUSSION

4.1 Microstructure Evolution of $Hf_7B_{23}Si_{22}C_6N_{40}$ Films Annealed to Various Temperatures in Air

4.1.1 As-deposited $Hf_7B_{23}Si_{22}C_6N_{40}$ Films

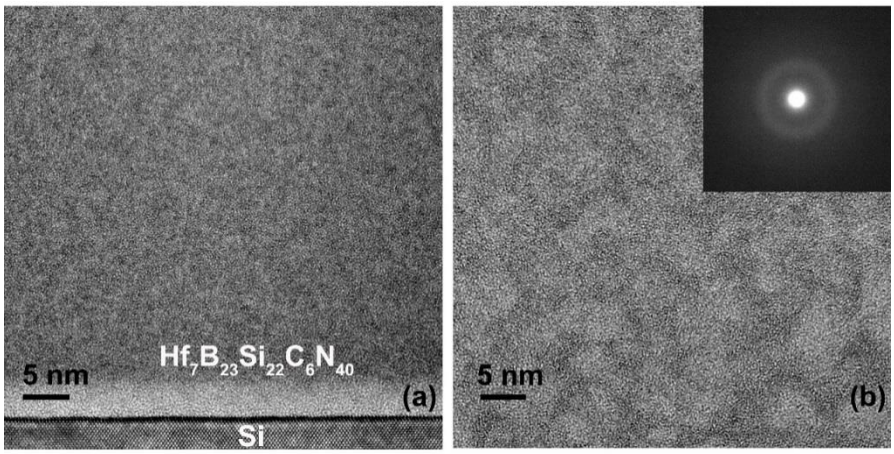

Fig. 2 Cross-section HRTEM image of as-deposited $Hf_7B_{23}Si_{22}C_6N_{40}$ film taken (a) near the Si substrate and (b) near the film surface and corresponding SAED pattern from the area.

Fig. 2 shows the microstructure of the original as-deposited $Hf_7B_{23}Si_{22}C_6N_{40}$ film as a reference for high-temperature behavior study. Figs. 2a and 2b are HRTEM images taken on a cross-section sample near the Si substrate and near the film surface, respectively. Both images reveal that the film had a rather homogeneous amorphous structure. In fact, the amorphous structure remained homogeneous across the whole film. The contrast difference in the amorphous film is probably due to the difference in electron absorption effect of different elements. Usually, heavy atoms (Hf) will absorb more electrons while lighter atoms (Si, B, C and N) will absorb less, resulting

Hf-rich area appear darker and light element-rich area appear brighter. The insertion of Fig. 2b on top right corner is the corresponding SAED pattern taken from the area. It shows a vague disc-like pattern instead of clear diffraction spots or rings, which is typical from a sample with amorphous structure.

4.1.2 $Hf_7B_{23}Si_{22}C_6N_{40}$ Films Annealed to 1100, 1200 and 1300 °C in Air

4.1.2.1 Cross-section Overview

Fig. 3 illustrates the overview of $Hf_7B_{23}Si_{22}C_6N_{40}$ films annealed to 1100, 1200 and 1300 °C in air. These films were compared with each other as they all had similar morphology: While the major part of the film remained amorphous, an oxide layer formed on top of the original unoxidized film and the thickness gradually increased with annealing temperature, resulting in a two-layer structure. Fig. 3a shows the cross-section of the whole $Hf_7B_{23}Si_{22}C_6N_{40}$ film annealed to 1100 °C and illustrates that the overall structure did not change significantly, a very thin oxide layer could be seen on the surface, which was examined by a zoom-in TEM image and shown in Fig. 3b. In fact, the thickness of the whole film was 1554 nm, while the thickness of the oxide layer was merely 30 nm. The oxide layer was formed by large numbers of crystalline particles appearing in dark and surrounded by amorphous matrix appearing bright, while the unreacted film remained amorphous. The interface between the oxide layer and the unreacted original film (denoted as “bottom layer” in the two-layer structure) was marked by a white line in Fig. 3b, while the actual film surface was marked by a black

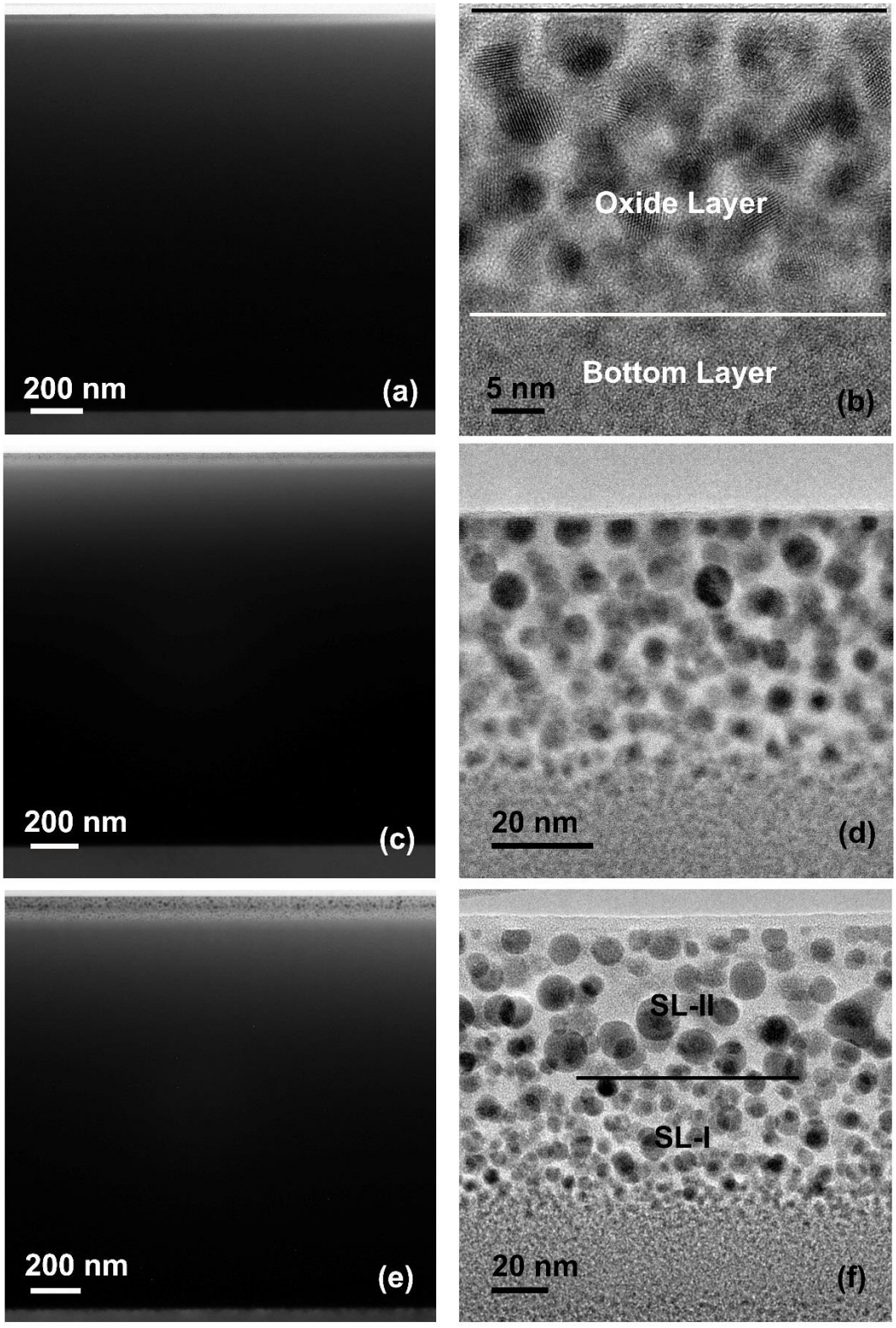

Fig. 3 Bright-field cross-section TEM image of $Hf_7B_{23}Si_{22}C_6N_{40}$ film (left) and the oxide layer on the film surface (right) annealed to (a) & (b) 1100 °C, (c) & (d) 1200 °C and (e) & (f) 1300 °C in air.

line. A high density of fine crystalline particles with a size ranging from 3 to 5 nm near the interface, and 4 to 6 nm near the film surface. There was a trend of size increase from the interface to the film surface but it's not immediately apparent. Detailed crystallographic information about both oxide layer and bottom layer is provided in Figs. 4 & 5 and will be discussed in the following paragraph. Fig. 3c shows the cross-section of $Hf_7B_{23}Si_{22}C_6N_{40}$ film annealed to 1200 °C. Compared to Fig. 3a, i.e., the film annealed to 1100 °C, the oxide layer had increased its thickness, to around 54 nm (see Fig. 3d), while the total thickness of the film increased to 1689 nm. Apart from the increase in thickness, the oxide layer had a clearer interface between itself and the bottom layer. The particles near the interface had similar morphology as the ones in Fig. 3b. However, as the film surface was approached, the particles became bigger and started to show spherical shape. Particle size increased to between 6 to 8 nm in the middle part of the oxide layer and reduced to between 4 to 6 nm at the surface. It is possible that the mass transfer between particles and surrounding matrix was restricted for those particles located at the surface while those positioned completely within the matrix could release and receive substance from all directions, which might explain the size reduction at the surface. Moreover, particles at the surface did not remain spherical as those in the volume. They were cut-off abruptly and formed incomplete spherical shape with cut-off surface exposed at the film surface. Similar phenomenon was observed during our previous study on the microstructure of annealed $Hf_7B_{23}Si_{17}C_4N_{45}$ films (not included within the present study). It was concluded that the cut-off happened at low-energy O-rich planes and was a result of

inability of particle growth to overcome the surface energy at this temperature [47]. Considering the similarities between the previous samples and this one, same conclusion may be applied. The particles could be identified as HfO_2, and the surrounding matrix most likely contained Si, O and B, forming a protective borosilicate glass layer. More evidence is shown in Figs. 6 and 7 and will be discussed later. Fig. 3e illustrates the cross-section of $Hf_7B_{23}Si_{22}C_6N_{40}$ film annealed to 1300 °C. The increase in oxide layer thickness continued along with temperature increase, which could be seen in a zoom-in TEM image of the oxide layer (Fig. 3f). The thickness across the film was measured as 1691 nm, very similar to the film annealed to 1200 °C, but the thickness of the oxide layer increased to around 95 nm. The oxide layer in this sample could be divided into two sublayers, as indicated by a black line in the approximate center of the oxide layer in Fig. 3f. Sublayer I (denoted as *SL-I*) contained large numbers of smaller particles while sublayer II (denoted as *SL-II*) consisted of coarser and more dispersed particles. Particle size in *SL-I* was generally less than 5 nm, with a few of them being as large as 10 nm. *SL-I* was probably where the initial particle growth happened after the nucleation at the interface. Particle size in *SL-II* bumped up significantly to between 9 and 18 nm. Compared to samples annealed to lower temperature, higher temperatures enabled higher diffusion rate for mass transfer from smaller particles to larger particles through the matrix, resulting in growth of larger particles at the expense of the smaller ones nearby. The process resulted in fewer larger particles. This so-called Ostwald ripening is an interfacial energy driven process that can take place in a two-phase mixture [48, 49]. Average particle size at

the film surface dropped to between 5 to 11 nm and cut-off of particles at the surface could be observed in this sample, similar to the one at 1200 °C. More TEM images and SAED analysis will be given in Figs. 8 and 9.

4.1.2.2 $Hf_7B_{23}Si_{22}C_6N_{40}$ Film Annealed to 1100 °C in Air

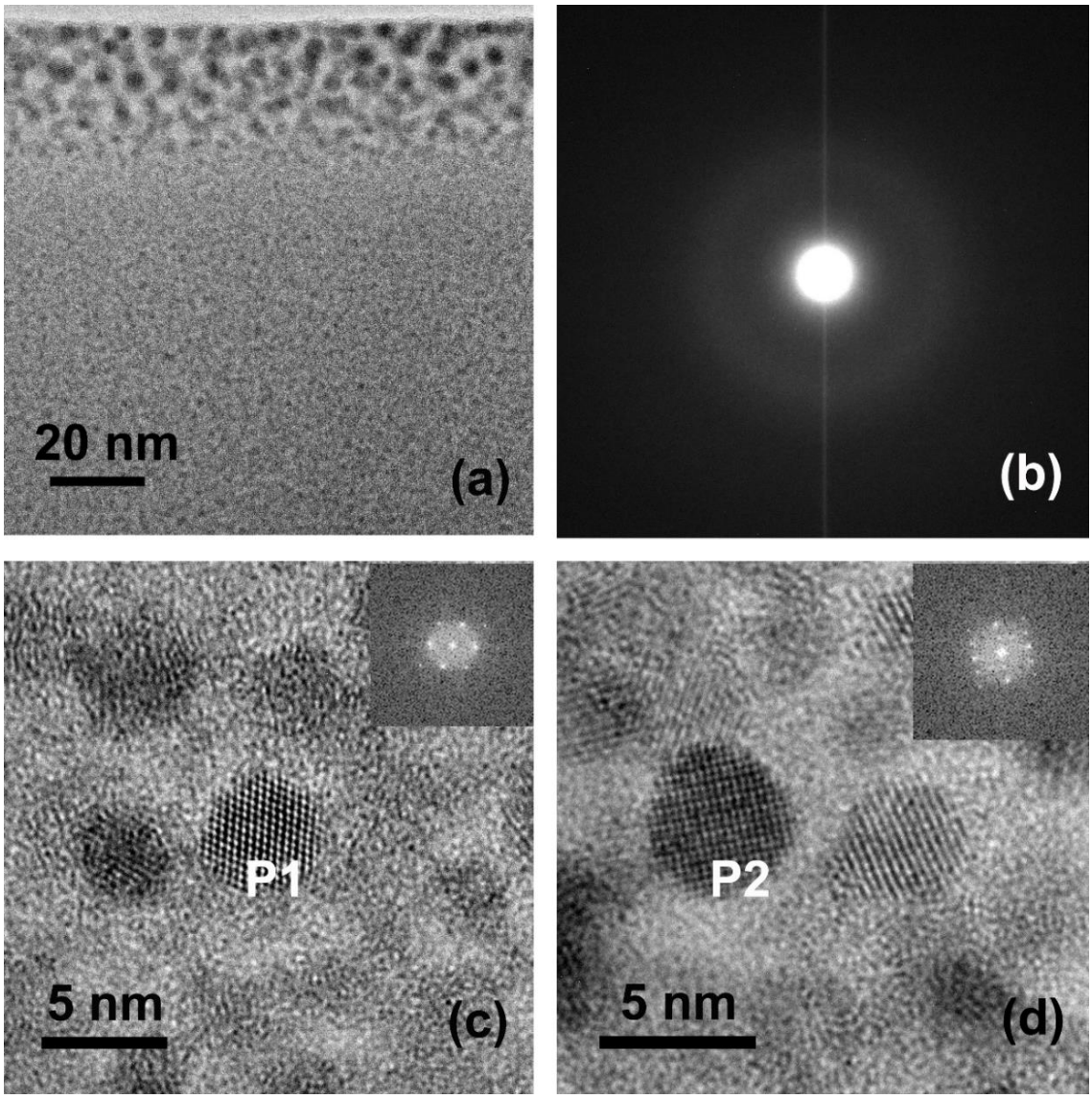

Fig. 4 (a) Bright-field cross-section TEM image of the oxide layer and part of the bottom layer in $Hf_7B_{23}Si_{22}C_6N_{40}$ film annealed to 1100 °C in air, (b) SAED pattern taken from the area covering the whole oxide layer and upper part of bottom layer and (c) & (d) HRTEM images taken from the oxide layer.

Fig. 4 illustrates details of the oxide layer in $Hf_7B_{23}Si_{22}C_6N_{40}$ film annealed to 1100 °C. Fig. 4a shows the overview of the oxide layer and the upper part of the

amorphous bottom layer, and the corresponding SAED pattern is shown in Fig. 4b. The SAED pattern did not reveal any existing crystalline structure within the area, which might be due to the following reasons: first, the relatively small crystalline particles and rather poor crystallinity could not provide strong electron diffraction. What's more, the area of interest to provide SAED pattern is limited by the physical size of the selected area aperture (SAA) and the minimal area is a circle with diameter of about 300 nm. However, the thickness of the oxide layer is about 30 nm, which means even the smallest area of interest could not cover the oxide layer only and had to include part of the amorphous bottom layer. The HRTEM images of the oxide layer were taken and two of them are shown as Figs. 4c and 4d. Particle denoted as P1 in Fig. 4c and P2 in Fig. 4d displayed clear crystalline fringes and corresponding Fast Fourier Transformation (FFT) of the crystalline structure is shown as the insertion in the corresponding figures. Particle P1 could be identified as either orthorhombic or tetragonal HfO_2 with $[1\bar{1}0]$ zone axis parallel to the electron beam. Two sets of lattice planes were measured. One with a d-spacing of 2.95 Å, could be identified as o-HfO_2/t-HfO_2 (111), while the other one with a d-spacing of 2.62 Å, could be identified as o-HfO_2/t-HfO_2 (002). Meanwhile in Fig. 4d, particle P2 could be identified as HfO_2 with [100] zone axis parallel to the beam. It was difficult to determine the exact crystalline structure due to the similarity of monoclinic, orthorhombic and tetragonal HfO_2 along [100] zone axis. Two sets of lattice planes were measured, one with a d-spacing of 2.60 Å and the other one with a d-spacing of 2.57 Å. The first one matches with m-HfO_2/o-HfO_2/t-HfO_2 (002) and the second one matches with m-HfO_2 (020), or t-HfO_2 (200), or

o-HfO_2 (020)/(200). Due to poor crystallinity of the particles, no further information was obtained from the oxide layer. However, by combining the analysis from the other samples, we were able to draw more conclusions, which would be discussed in the following paragraph.

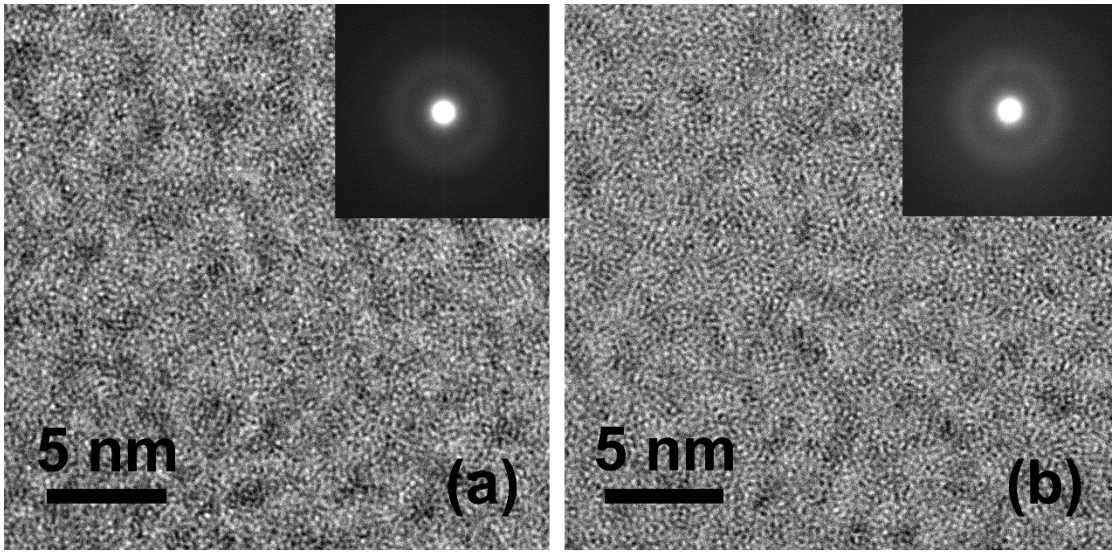

Fig. 5 HRTEM images and SAED patterns of the bottom layer in the $Hf_7B_{23}Si_{22}C_6N_{40}$ film annealed to 1100 °C in air taken (a) close to substrate and (b) in the middle part.

Fig. 5 displays the microstructure of the bottom layer in $Hf_7B_{23}Si_{22}C_6N_{40}$ film annealed to 1100 °C in air. The bottom layer maintained amorphous structure, both in the area close to substrate (Fig. 5a) and in the middle (Fig. 5b). The insertion in each figure is the corresponding SAED pattern taken from the same area. Both patterns show amorphous halos and match with the HRTEM image. However, compared to the amorphous structure in the as-deposited film, the contrast difference between the Hf-rich area and light element-rich area were strengthened. Some small black spots could be observed in HRTEM images which could be Hf-containing clusters. Despite that, the overall structure of the film did not undergo significant changes, showing good thermal stability of the film at this temperature.

4.1.2.3 $Hf_7B_{23}Si_{22}C_6N_{40}$ Film Annealed to 1200 °C in Air

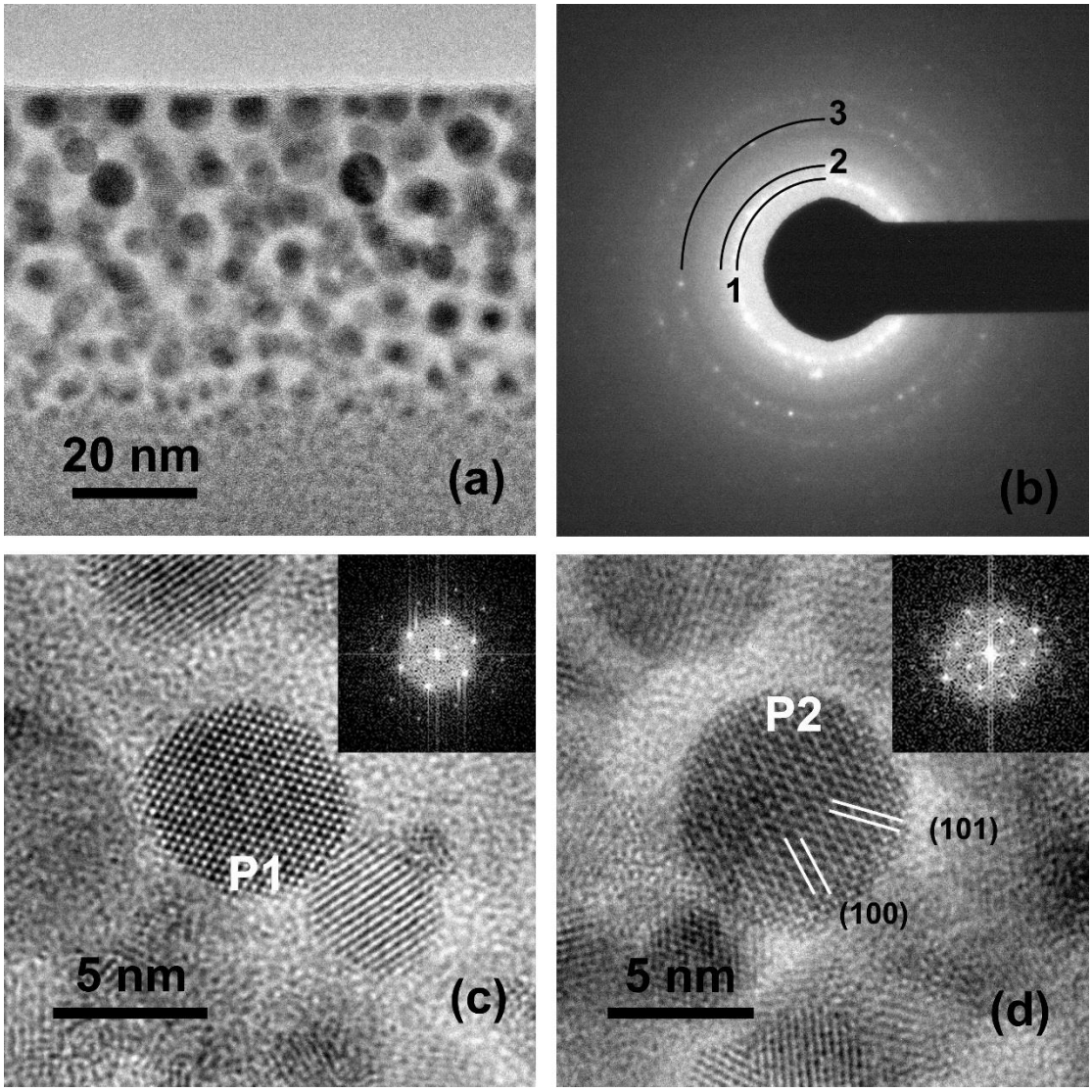

Fig. 6 (a) The bright-field cross-section TEM image of the oxide layer and upper part of the bottom layer in the $Hf_7B_{23}Si_{22}C_6N_{40}$ film annealed to 1200 °C in air, (b) the corresponding SAED pattern and (c) & (d) HRTEM images taken from the oxide layer.

Fig. 6 shows detailed microstructure of the oxide layer in $Hf_7B_{23}Si_{22}C_6N_{40}$ film annealed to 1200 °C in air. The overall structure of the oxide layer, along with part of the bottom layer underneath, is illustrated in Fig. 6a and the corresponding SAED pattern of the area in Fig. 6b. Unlike the film annealed to 1100 °C, this sample had a thicker oxide layer that also contained particles with better crystallinity, which was demonstrated by a clearer polycrystalline diffraction ring pattern as shown in Fig. 6b.

A total of 3 rings were identified which correspond to d-spacing of 3.02, 2.57 and 1.83 Å, respectively. The first one could be identified as o-HfO_2/t-HfO_2 (111), and the second one is close to t-HfO_2 (020)/(200), or m-HfO_2 (200)/(020)/(002), or o-HfO_2 (200)/(020). Likewise, the third ring could be either t-HfO_2 (220)/(202), or o-HfO_2 (202)/(022), or m-HfO_2 (220)/(022). The HRTEM images of the oxide layer are presented as Figs. 6c and 6d. In Fig. 6c, the particle P1 could be identified as either t-HfO_2 or o-HfO_2 with $[1\bar{1}0]$ zone axis parallel to the electron beam. Two sets of lattice planes were analyzed. The first one is close to t-HfO_2 or o-HfO_2 (111), with a d-spacing of 3.02 Å, while the second one corresponds to t-HfO_2 or o-HfO_2 (002), with a d-spacing of 2.62 Å. The particle P2 in Fig. 6d was identified to be o-HfO_2 or t-HfO_2 as its (100) and (101) planes were marked. They have lattice spacing of 5.06 and 3.68 Å, respectively.

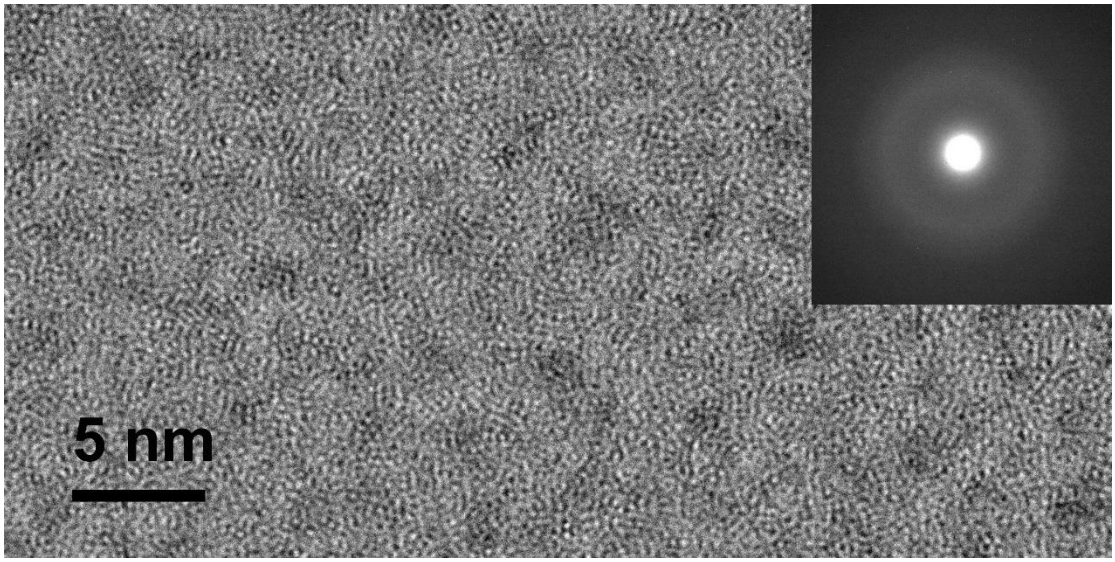

Fig. 7 HRTEM image of the bottom layer in the $Hf_7B_{23}Si_{22}C_6N_{40}$ film annealed to 1200 °C in air and (insertion) the corresponding SAED pattern.

Meanwhile, Fig. 7, which illustrates a typical HRTEM images taken from the bottom layer demonstrates that it mostly remained amorphous with some possibly Hf-rich nanoclusters. No crystalline structure could be identified from the SAED pattern.

Overall, there was no significant changes in microstructure compared to the film annealed to 1100 °C.

4.1.2.4 $Hf_7B_{23}Si_{22}C_6N_{40}$ Film Annealed to 1300 °C in Air

Fig. 8 shows the details of the microstructure of oxide layer in $Hf_7B_{23}Si_{22}C_6N_{40}$ film annealed to 1300 °C. As mentioned above the oxide layer could be divided into two sublayers. HRTEM images taken from both sublayers are presented. Fig. 8a is the SAED pattern taken from the oxide layer including *SL-I* and *SL-II*. It contains several visible diffraction rings and the first three were analyzed. They correspond to lattice spacing of 2.94, 2.58 and 1.83 Å, respectively. The result is similar to that for the film annealed to 1200 °C. The first ring is the diffraction of o-HfO_2/t-HfO_2 (111), while the second one comes from the diffraction of t-HfO_2 (020)/(200), or m-HfO_2 (200)/(020)/(002), or o-HfO_2 (200)/(020), and the third one is the diffraction ring of t-HfO_2 (220)/(202), or o-HfO_2 (202)/(022), or m-HfO_2 (220)/(022). Oxide particles in both *SL-I* and *SL-II* were studied by HRTEM images and two images were selected as Figs. 8b and 8c. Fig. 8b was taken in *SL-I*, the particle in view is about 10 nm in diameter and could be identified as m-HfO_2 with [100] zone axis parallel to the beam. Both (011) and (002) planes were marked in Fig. 8b. The corresponding lattice spacing is 3.63 and 2.60 Å, respectively. Higher annealing temperature enabled the faster growth and better crystallinity of HfO_2 particles, resulting larger and highly crystallized HfO_2 in *SL-II*. For example, Fig. 8c was taken from *SL-II* and the two particles in view (designated as P1 and P2) both have diameters around 12 nm. P1 was identified as orthorhombic or tetragonal HfO_2. Its (111) plane was marked in the figure and has a d-spacing of 2.93

Å. This lattice parameter does not appear in monoclinic HfO_2. Similarly, particle P2 was identified as monoclinic HfO_2 as the lattice fringes matches with m-HfO_2 $(\bar{1}11)$ uniquely, which has a d-spacing of 3.13 Å.

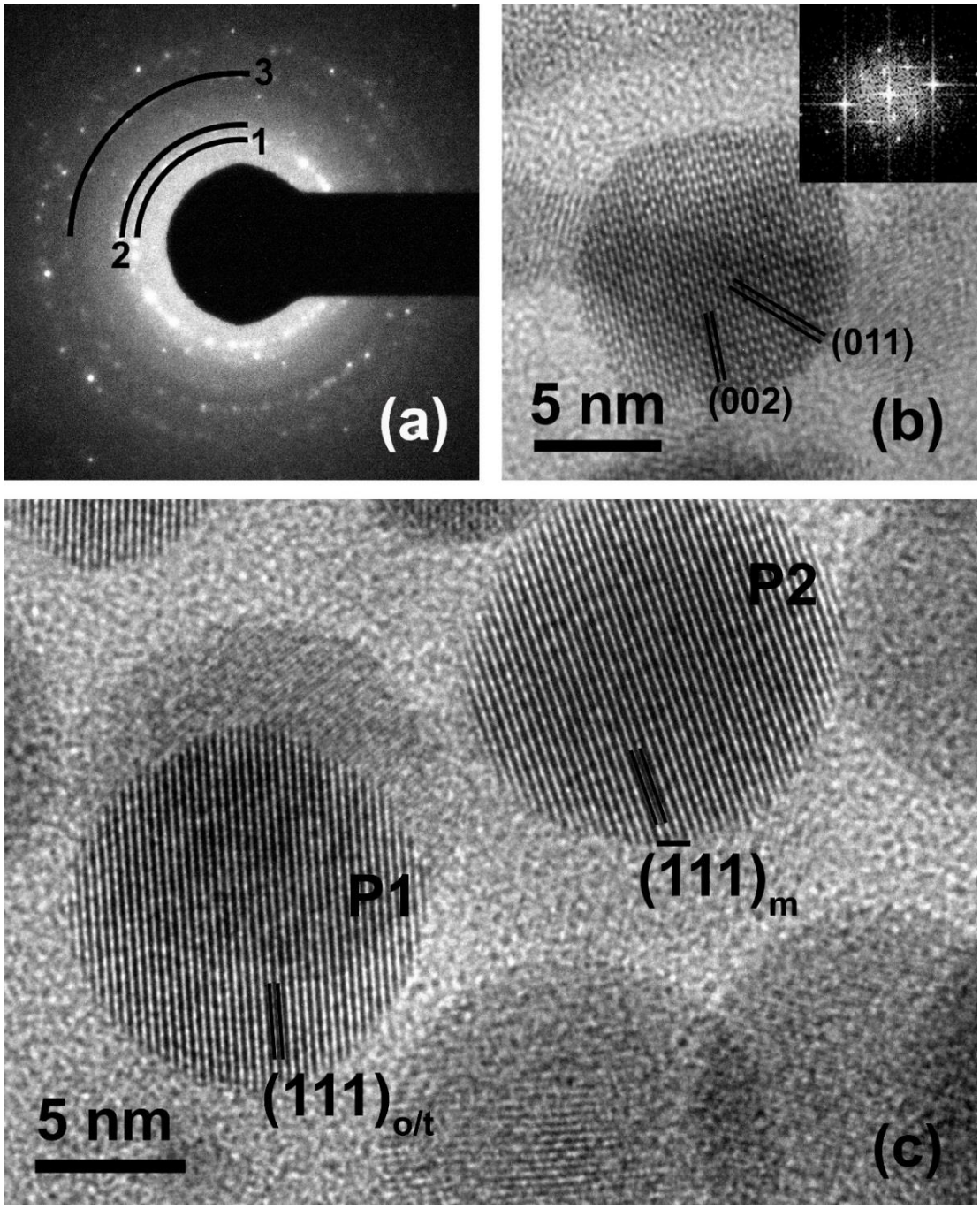

Fig. 8 (a) The SAED pattern taken from the oxide layer in the $Hf_7B_{23}Si_{22}C_6N_{40}$ film annealed to 1300 °C in air and HRTEM images taken from (b) *SL-I* and (c) *SL-II*, respectively.

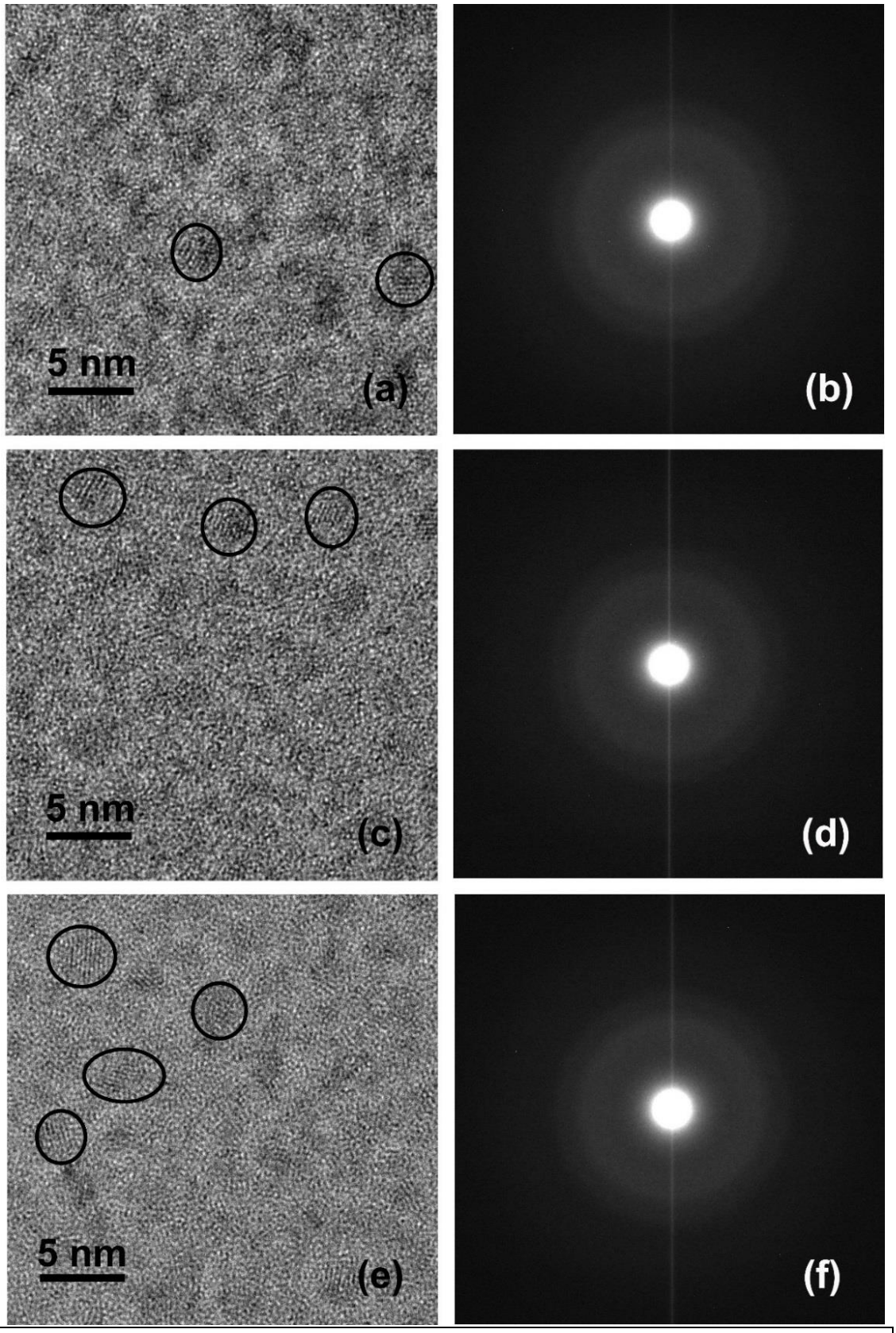

Fig. 9 HRTEM images and the corresponding SAED pattern taken from different part of the bottom layer in the $Hf_7B_{23}Si_{22}C_6N_{40}$ film annealed to 1300 °C in air: (a) & (b) from the area close to top layer, (c) & (d) from the area roughly in the middle and (e) & (f) from the area close to substrate.

HRTEM image analysis suggested that annealing to 1300 °C had some visible influence on the microstructure of the bottom layer, which no longer remained purely amorphous. The results are presented in Fig. 9. Three HRTEM images taken from different areas of the bottom layer were selected. They were taken along with the SAED patterns from the upper part of the bottom layer which was close to the oxide layer (Figs. 9a and 9b), roughly in the middle (Figs. 9c and 9d) and from the lower part of the bottom layer which was close to substrate (Fig. 9e and 9f). In all three images small nanocrystalline particles could be observed, which were marked in white circles. These particles had average size of 2 nm and crystalline structure during the initial forming stage could be seen. A similar phenomenon could be observed in the sample annealed to 1200 °C, but it was much less obvious. It is because in samples annealed to lower temperatures there were only contrast changes. Hf-rich area which appeared in darker contrast shrank in size and deepened in contrast compared to the original as-deposited film, suggesting possible Hf atom agglomeration. But in this sample, signs of recrystallization started to appear aside from the contrast changes. Due to the limited size of crystalline structure, the SAED patterns do not exhibit signs of recrystallization as illustrated in Figs. 9b, 9d and 9f. Overall, the microstructure of the bottom layer shifted to a transition state between a completely amorphous structure and a nanocrystalline composite structure, and the analysis of the nanocrystalline particles carried on in the film annealed to 1400 °C and will be discussed in the following paragraph.

4.1.3 $Hf_7B_{23}Si_{22}C_6N_{40}$ Films Annealed to 1400 °C in Air

4.1.3.1 Oxide Layer

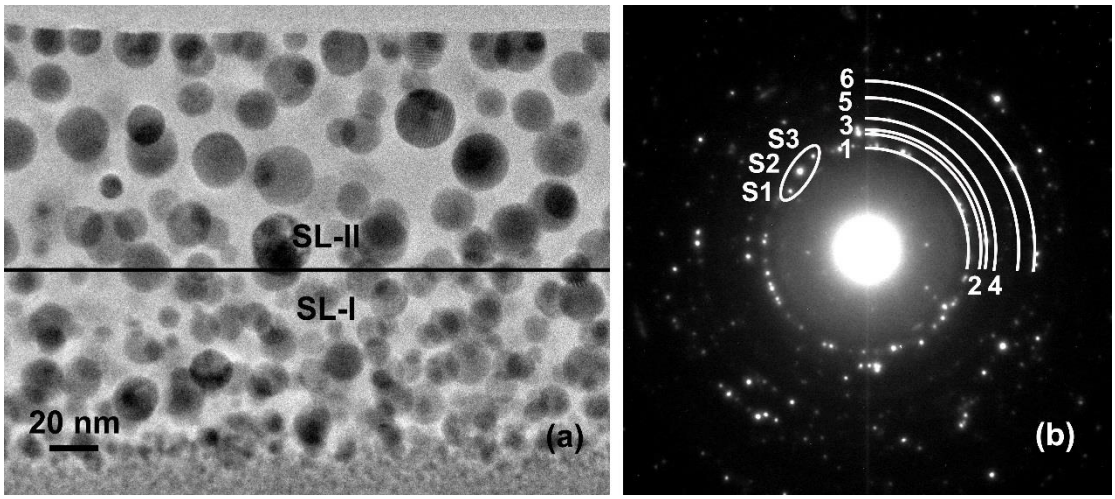

Fig. 10 (a) The bright-field TEM image taken from the cross-section of the oxide layer from the $Hf_7B_{23}Si_{22}C_6N_{40}$ film annealed to 1400 °C in air and (b) the corresponding SAED pattern.

Annealing the $Hf_7B_{23}Si_{22}C_6N_{40}$ film to 1400 °C led to significant changes in microstructure, both in oxide layer and bottom layer. Fig. 10a illustrates an overview on the cross-section of the oxide layer, which had a thickness of 180 nm. It could be divided into two sublayers similar to the ones of 1300 °C. *SL-I* contained large numbers of spherical nanoparticles placed close to each other. The size of these particles varied which could be as small as 5 nm, or as large as 20 nm. In *SL-II*, particles were generally larger and more dispersed, the smallest ones had a diameter of 10 nm, and the larger ones could be as big as 30 nm. The total number of particles reduced, and more space were left between them, filled by amorphous matrix. Despite growth in thickness, the overall structure of the oxide layer was still intact and dense without porous structure and fast oxygen diffusion channel. Fig. 10b is the corresponding SAED pattern taken from the oxide layer, including both sublayers. The Clear diffraction ring pattern

suggests the formation of crystalline structure. It is worth noticing that most of the rings are split into multiple diffraction spots, which is related to the more dispersed particle distribution in the oxide layer, especially in *SL-II*. While the area of interest, i.e. the selected area aperture size remained the same, increased particle size and distance between individual particles meant the total number of particles which could be included within the area of interest reduced. Nevertheless, clearer diffraction rings offered more detailed information on the microstructure of the oxide layer. A total of 6 diffraction rings were analyzed in a similar manner to the previous analysis. Ring 1 is a superimposed diffraction ring that consists of at least three sets of electron diffraction spots from three individual lattice planes, which were marked, from bottom to top, S1, S2 and S3 within the while circle. S1 corresponds to a lattice parameter of 3.17 Å, which is the d-spacing of m-HfO_2 $(\bar{1}11)$. S2, on the other hand, is the diffraction of o-HfO_2/t-HfO_2 (111). It corresponds to the lattice spacing of 2.98 Å. S3 corresponds to a lattice parameter of 2.87 Å, which is the unique diffraction of m-HfO_2 (111). Ring 2 and Ring 3 are very close to each other, they correspond to d-spacing of 2.64 and 2.58 Å, respectively. Ring 2 is the possible diffraction of m-HfO_2/t-HfO_2/o-HfO_2 (002), while Ring 3 is m-HfO_2 (200)/(020), or o-HfO_2 (020), or t-HfO_2 (200). Ring 4 corresponds to a d-spacing of 2.34 Å. There are a number of planes that could be related to it. Monoclinic HfO_2 (120)/(021)/(012) all have lattice parameters that are close, and o-HfO_2/t-HfO_2 (102) have similar lattice parameters as well. Ring 5 corresponds to m-HfO_2 (112)/(121), they both have the lattice parameter close to 2.01 Å. There is no plane in orthorhombic or tetragonal HfO_2 that can produce this diffraction ring. Ring 6

is corresponding to the d-spacing of 1.82 Å and several lattice parameters from different HfO_2 structure are reasonably close to this number. They are t-HfO_2 (220)/ (202), or o-HfO_2 (202)/ (022), or m-HfO_2 (220)/ (022).

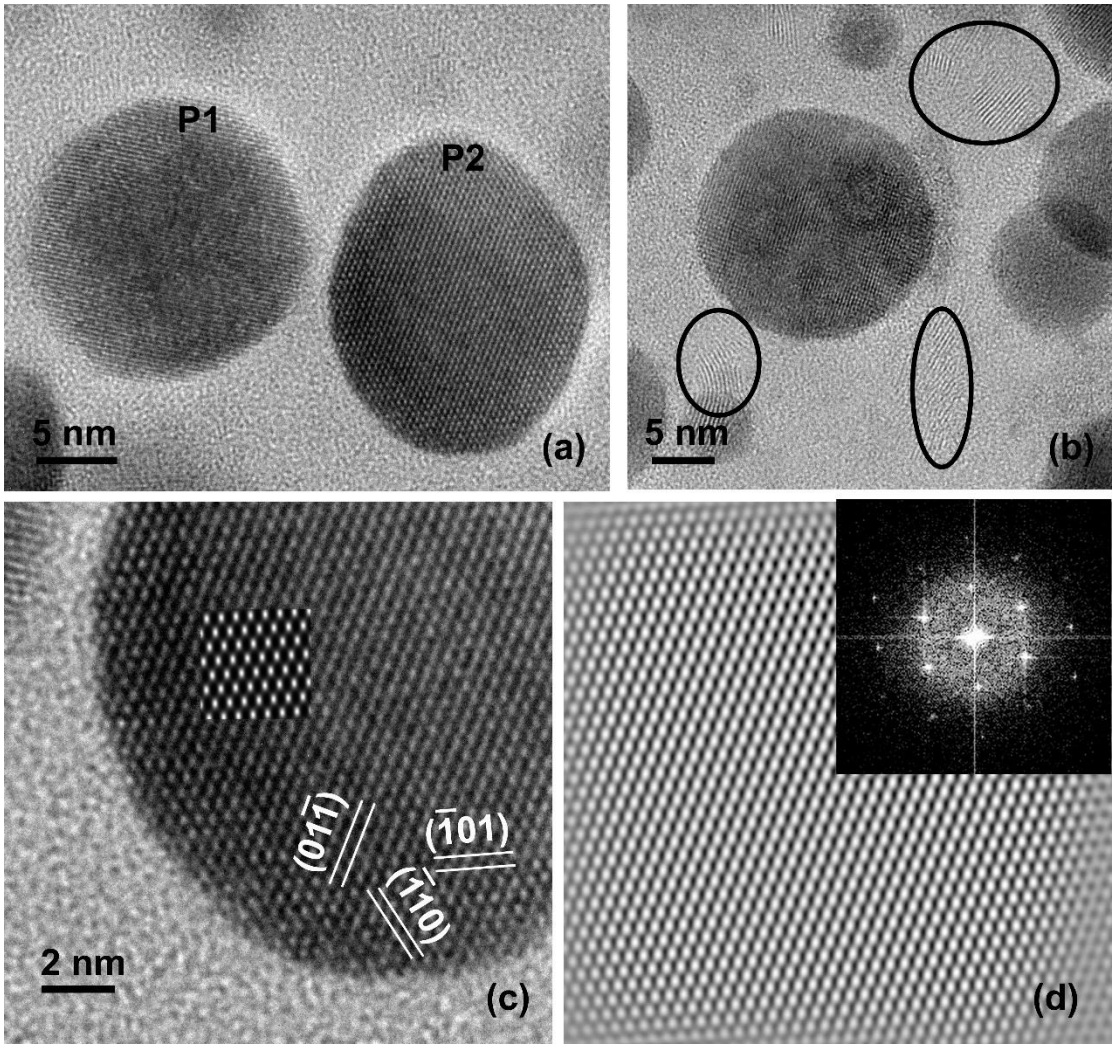

Fig. 11 The HRTEM images illustrate (a) the HfO_2 particles and (b) partially recrystallized glass matrix in *SL-I* of the oxide layer in the $Hf_7B_{23}Si_{22}C_6N_{40}$ film annealed to 1400 °C in air, (c) zoom-in HRTEM image of the particle P2 in Fig. 11a and (insertion) the corresponding simulation result, (d) the inversed FFT image representing the m-HfO_2 crystalline structure viewing from $[\bar{1}\bar{1}\bar{1}]$ direction based on (insertion) the FFT of the original image.

Detailed microstructure of *SL-I* is presented in Fig. 11 and some interesting findings were made. Fig. 11a illustrates two typical particles in *SL-I*, which have similar size of 17 nm. Particle P1 had spherical shape, and the lattice fringes observed have a

d-spacing of 2.97 Å, which is close to o-HfO_2/t-HfO_2 (111). Particle P2 on the other hand, had eclipse shape, it was identified as monoclinic HfO_2 viewing from $[\bar{1}\bar{1}\bar{1}]$ zone axis. The conclusion was made upon the FFT of the original crystalline structure, the inversed FFT and the HRTEM image simulation, which are presented in Fig. 11d and the insertion of Fig. 11c, respectively. Monolinic HfO_2 ($\bar{1}10$), ($01\bar{1}$) and ($\bar{1}01$) were identified and marked in Fig. 11c according to their relation in the lattice space, and the measured d-spacing are 3.57, 3.61 and 3.93 Å, respectively. The first two are close to their respective theoretical value based on X-ray Powder Diffraction File (PDF #65-1142, a=5.12 Å, b=5.17 Å, c=5.30 Å, β=99.18˚, $P2_1/C$). HRTEM image simulation was conducted to validate the results. The insertion in Fig. 11c (the center of the particle) is a simulated HRTEM image of m-HfO_2 viewing from $[\bar{1}\bar{1}\bar{1}]$ zone axis using the condition of a defocus of 46 nm and a thickness of 7.6 nm. The HfO_2 unit cell used for the simulation was constructed according to Ref. [51]. The final result was able to fit well into the actual HRTEM image. The glass matrix, while mostly amorphous, could be observed partially recrystallized, which was marked using the black circle in Fig. 11b. Partial recrystallization did not appear in lower-temperature samples and the product could be identified as high quartz SiO_2, having (101) plane oriented parallel to the electron beam, with a d-spacing of 3.4 Å. The formation of quartz SiO_2 in the amorphous matrix was found only near the interface between oxide layer and bottom layer. During the previous analysis of the $Hf_7B_{23}Si_{17}C_4N_{45}$ films. Similar quartz SiO_2 was also observed.

Fig. 12 presents the *SL-II* of the oxide layer in the $Hf_7B_{23}Si_{22}C_6N_{40}$ film annealed to

1400 °C in air. Fig. 12a is a HRTEM image taken at the film surface. The particle in view was characterized as orthorhombic HfO_2 with its [010] zone axis parallel to the beam.

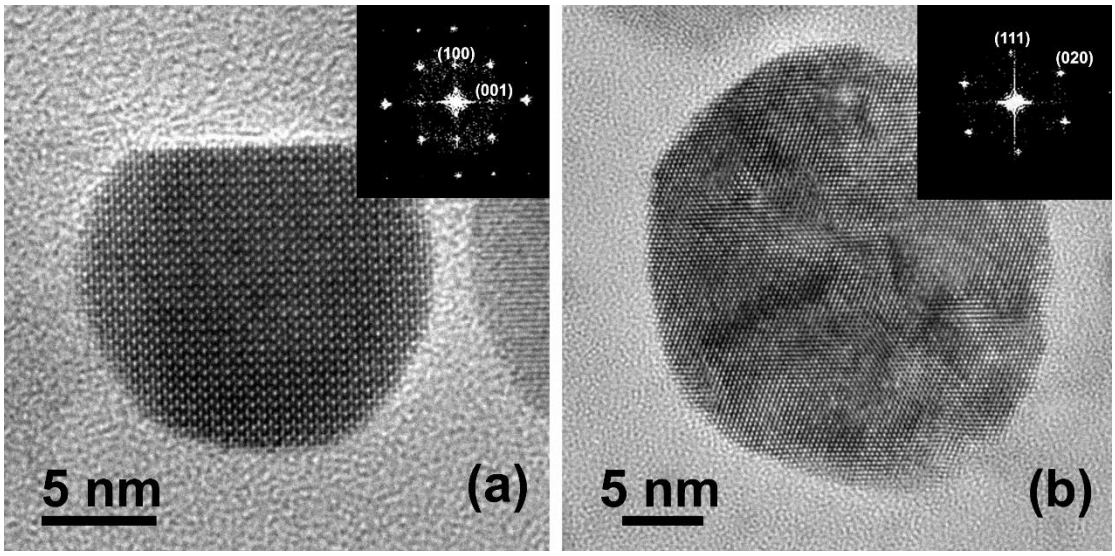

Fig. 12 HRTEM image of (a) orthorhombic HfO_2 viewing from [010] zone axis and (b) orthorhombic HfO_2 viewing from $[10\bar{1}]$ zone axis and the corresponding FFT taken from *SL-II* of the oxide layer in the $Hf_7B_{23}Si_{22}C_6N_{40}$ film annealed to 1400 °C.

Better crystallinity at higher annealing temperatures enabled us to identify the microstructure more accurately and reliably. For example, o-HfO_2 (100) and (001) were identified using FFT and the results were marked in the insertion of Fig. 12a. Their lattice spacing were measured as 5.05 and 5.22 Å, respectively. Among these two, 5.05 Å is a lattice parameter that uniquely belongs to orthorhombic HfO_2 as o-HfO_2 has a significantly shorter a-axis when compared to b- and c-axis, which is also smaller than rather large unit cell dimensions of tetragonal and monoclinic HfO_2. It is also safe to conclude that at lower annealing temperatures some particles that we were unable to distinguish between orthorhombic and tetragonal are also o-HfO_2. Tetragonal HfO_2, while maintaining higher order symmetry, requires higher energy to form. In fact, the transition between monoclinic to tetragonal HfO_2 happens at 1700 °C which is higher

than the current annealing temperature, while the formation of orthorhombic HfO_2 requires an appropriate combination of temperature (not as high as 1700 °C) and pressure [52]. Considering various gaseous species evolving in the system during high-temperature oxidation, it is entirely possible. Fig. 12b is another orthorhombic HfO_2 in *SL-II* viewing from $[10\bar{1}]$ zone axis. No partial recrystallization in the surrounding matrix was observed in *SL-II*.

4.1.3.2 Bottom Layer

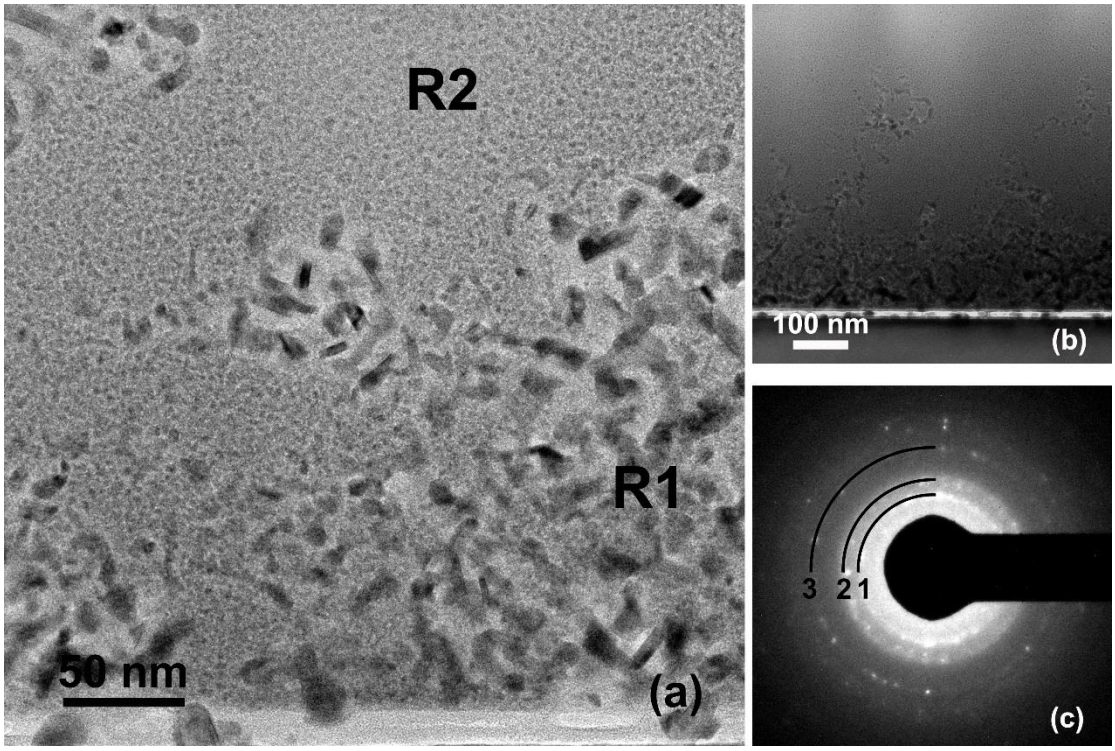

Fig. 13 (a) & (b) Bright-field TEM images and (c) SAED pattern taken from the bottom layer close to substrate in the $Hf_7B_{23}Si_{22}C_6N_{40}$ film annealed to 1400 °C in air.

In previous samples, the bottom layer showed more and more obvious trace of nucleation and recrystallization as annealing temperature increased. However, the main structure remained homogeneous and crystallinity of nanocrystalline particles was poor. It was not the case in the sample annealed to 1400 °C in air. Figs. 13a and 13b illustrate part of the bottom layer that was close to substrate. The morphology

changed significantly as nanocrystalline particles with various shapes formed in this region. This recrystallization process did not happen homogeneously throughout the whole bottom layer, instead, it was only observed extensively in the area close to substrate. The measurement showed that the almost fully recrystallized region (denoted as R1) had a thickness of about 150 nm, while in some area it could extend further into the film for as long as 400 nm, as seen in Fig. 13b. The rest part of the bottom layer exhibited a partially recrystallized nanocrystalline composite structure mostly (denoted as R2). Numerous small nanoparticles could be seen formed as a result of continuous nucleation that was observed vaguely in the sample annealed to 1300 °C. SAED pattern taken from the area illustrates that HfB_2 and HfN formed in this region, as shown in Fig. 13c. Among the three diffraction rings, the first one corresponds to a d-spacing of 2.71 Å. This lattice parameter does not match any plane in HfO_2, instead, it matches well with HfB_2 (100). Ring 2 corresponds to 2.19 Å and it could be identified as HfB_2 (101). Ring 3 corresponds to a d-spacing of 1.64 Å. It could be identified as HfN (220). Due to the overall poor crystallinity, the conclusion was made based on matching results with HRTEM images and comparing with samples annealed to higher temperatures, which will be discussed separately.

More HRTEM images were taken from the area, including both the almost fully recrystallized region (R1) and the partially recrystallized nanocrystalline composite region (R2), as illustrated in Fig. 14. Among the presented images, Fig. 14b and 14c display two nanocrystalline particles and the surrounding matrix in R1. The formation of independent HfN nanoparticles in R1 could be confirmed as one of them was

presented in Fig. 14b. It was in view from one of its [110] zone axis. HfN (111), with a measured d-spacing of 2.64 Å, and HfN (200), with a measured d-spacing of 2.28 Å were marked in FFT of the original lattice structure. Fig. 14c illustrates a combined

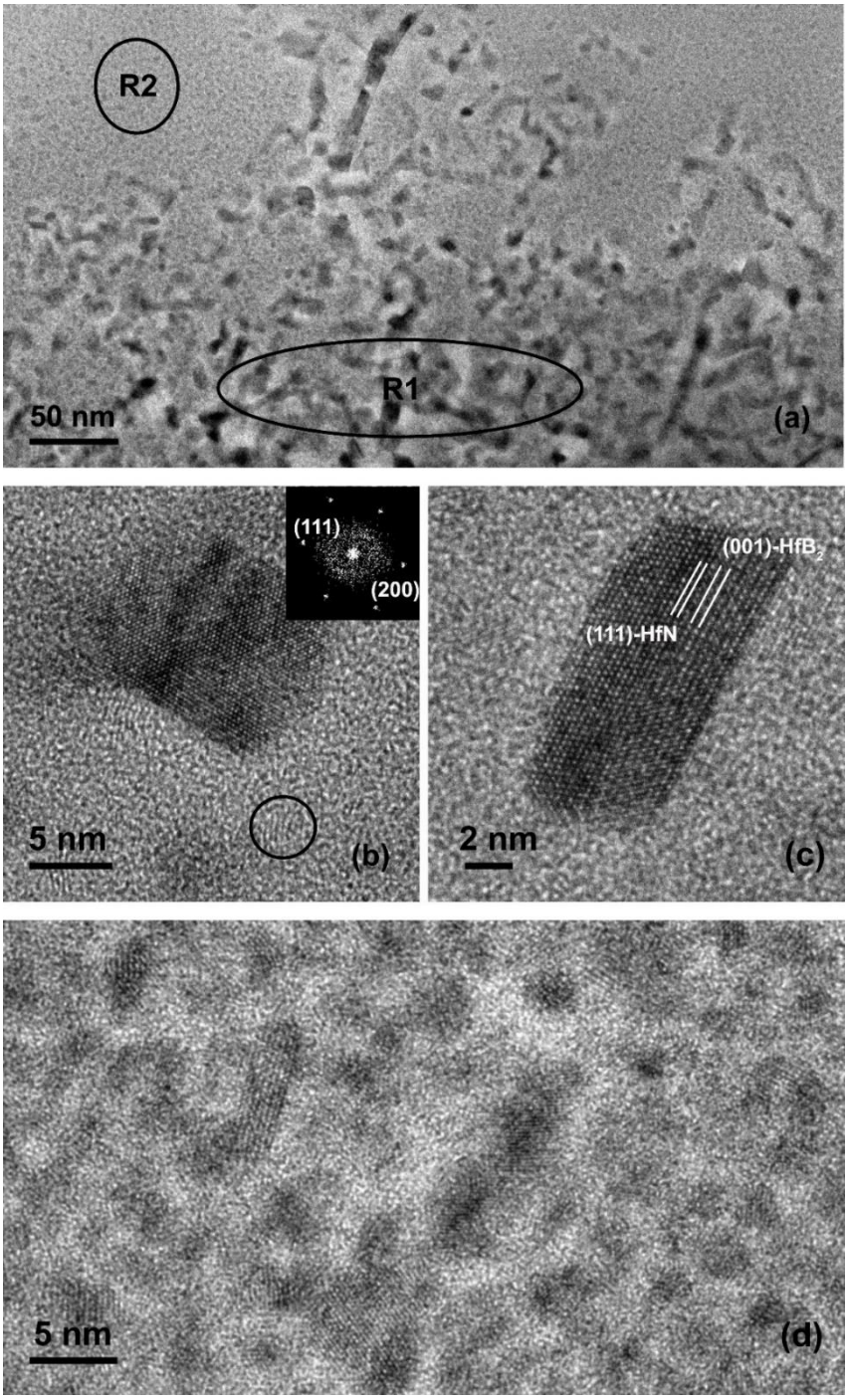

Fig. 14 HRTEM images taken from the the bottom layer close to substrate in the $Hf_7B_{23}Si_{22}C_6N_{40}$ film annealed to 1400 °C: (a) an overview of the area of interest, (b) a HfN particle and the surrounding matrix in R1, (c) a combined HfB_2-HfN particle in R1 and (d) the nanocrystalline composite structure of R2.

HfB_2-HfN particle that joined coherently via their corresponding close-packed Hf atomic plane, which is (001) for HfB_2, and (111) for HfN. HfB_2 has a hexagonal structure (P6/mmm, a=3.14 Å, c=3.47 Å) while HfN has a cubic structure (Fm-3m a=4.55 Å). The difference in lattice structure and parameters between these two could be observed with ease. This particular combination of HfB_2-HfN was observed only in samples annealed to 1400 °C or higher. A more detailed explanation of this structure will be given in the analysis of the film annealed to 1500 °C. On the other hand, boundary areas surrounding Hf-containing particles were not completely amorphous. Recrystallization on very small scale could be observed as seen in the black circle in Fig. 14b. Very limited information could be extracted due to their small size. Meanwhile, the microstructure of region R2 is shown in Fig. 14d. Compared to samples annealing to lower temperatures, agglomerated Hf-rich clusters had grown in size and exhibited clearly visible crystallinity, while Hf-depleted areas remained amorphous, forming nanocrystalline composite structures.

More HRTEM images were taken from various other areas in the bottom layer. For example, Figs. 15a and 15b were taken from the area just underneath the top layer and the area in the middle part of the bottom layer respectively. Both areas showed similar microstructure as R2 in Fig. 14d. However, the nanocrystalline particles were generally smaller and only showed limited degree of crystallinity. The difference between Figs. 15a and 15b is relatively small. The SAED patterns of the corresponding areas are inserted in each figure. Both SAED patterns look almost identical to each other: the previous disc-like, halo patterns which correspond to amorphous structure

split into vague diffraction rings. Measurement was performed on both patterns, producing the same result. For example, Ring 1 in Fig. 15a corresponds to the d-spacing of 2.76 Å, while ring 2 corresponds to the d-spacing of 2.16 Å. These two are diffractions of HfB_2 (100) and (101), respectively. The formation of HfB_2 nuclei matched with the previous analysis. However, there was no solid proof of crystalline HfN formation from either SAED pattern or HRTEM images in these areas. It is possible that during the recrystallization process of the bottom layer, HfB_2 formed first, followed by the recrystallization of HfN either by forming independent nuclei or by joining the close-packed Hf atomic plane (001) of HfB_2.

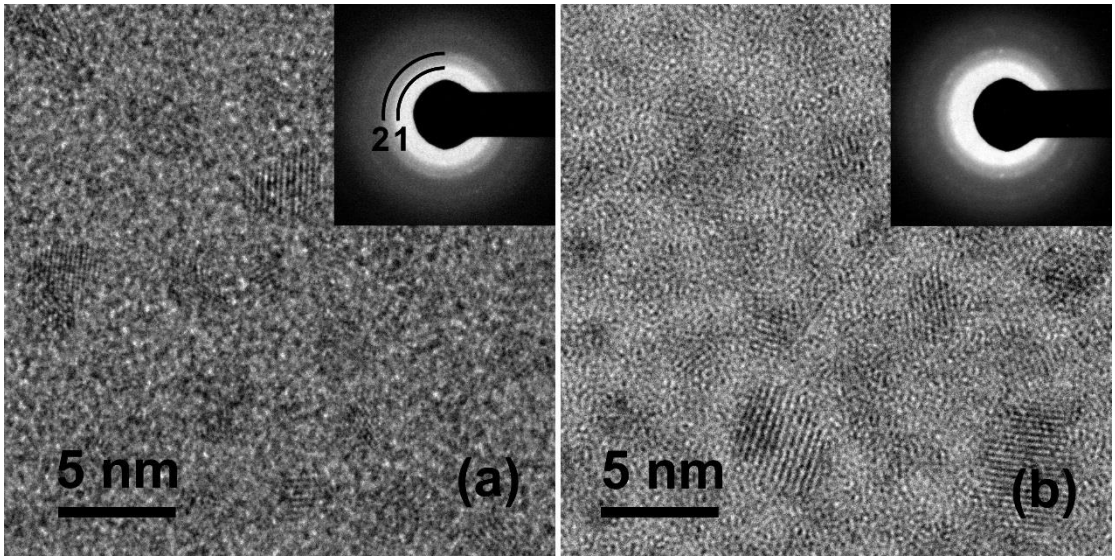

Fig. 15 HRTEM images and the corresponding SAED patterns taken from (a) the part of bottom layer just underneath the top oxide layer and (b) the part of bottom layer roughly in the middle.

4.1.4 $Hf_7B_{23}Si_{22}C_6N_{40}$ Films Annealed to 1500 and 1600 °C in Air

4.1.4.1 Overview

The growth of oxide layer and the recrystallization of the bottom layer continued

when samples were exposed to higher annealing temperatures. Fig. 16 illustrates the overall view of the whole cross-section of two $Hf_7B_{23}Si_{22}C_6N_{40}$ films that were annealed to 1500 and 1600 °C. Both samples maintained good structure integrity and formed the familiar two-layer structure. For the film annealed to 1500 °C, the total thickness was 1610 nm, while the thickness of the oxide layer was 356 nm. For the film annealed to 1600 °C, the total thickness was 1900 nm, and the oxide layer was just over 1000 nm thick. The oxide layers in both films were dense and intact, despite significant growth in thickness as a result of rapid oxidation, especially for the film annealed to 1600 °C. The bottom layers of both films fully recrystallized into a polycrystalline structure. Previous study on the oxidation kinetics of the $Hf_7B_{23}Si_{17}C_4N_{45}$ films annealed to various temperatures in air revealed that the oxide growth, as indicated by the thickness of oxide layer (x), followed a parabolic oxidation law and oxygen diffusion was the rate-limiting factor of the oxidation process [47]. Similar study was conducted on $Hf_7B_{23}Si_{22}C_6N_{40}$ films. Fig. 17 is a plot of lnx^2 vs the reciprocal of annealing temperatures (T). A linear curve was fitted using the data from the film annealed to 1200, 1300, 1400 and 1500 °C. It is clear that the data from the film annealed to 1100 °C and 1600 °C do not fit well with the relationship. For the film annealed to 1100 °C in air, the oxide layer is only 28 nm thick, which falls into the range of thin regime (<500 Å). It was reported that oxidation of Si is significantly boosted which adds an enhancement term to the linear-parabolic relationship between oxide thickness and oxidation time. The enhancement term decays exponentially as thickness increases [53-55]. Several theories were proposed to explain the

phenomenon including space-charge effect and silicon surface defects. Since there is considerable amount of silicon present in the film, this enhancement theory could play an important role. For the film annealed to 1600 °C, the increase in oxidation rate could be explained by the microstructure changes at the interface which was caused by the recrystallization of the bottom layer. As a result, the oxidation rate became faster at the interface. A detailed explanation will be given in a later chapter. Also, in the oxide layer, the elimination of two sublayers that appeared in low-temperature samples would reduce the consumption of oxidizing species as it diffused through. The result matched well with this explanation, as we could observe a slight increase of the oxidation rate for the film annealed to 1500 °C, and a significant boost for the film annealed to 1600 °C, depicturing from the original parabolic relationship. Details of the microstructure changes and how these changes affected the oxidation kinetics will be discussed further in the upcoming paragraphs.

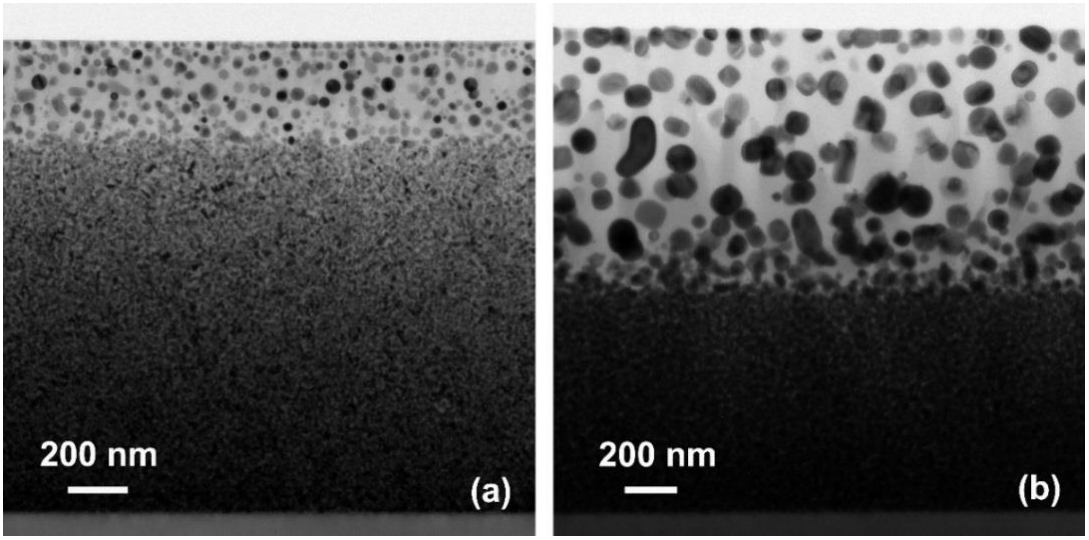

Fig. 16 The bright-field cross-section TEM image of $Hf_7B_{23}Si_{22}C_6N_{40}$ films annealed to (a) 1500 °C and (b) 1600 °C in air.

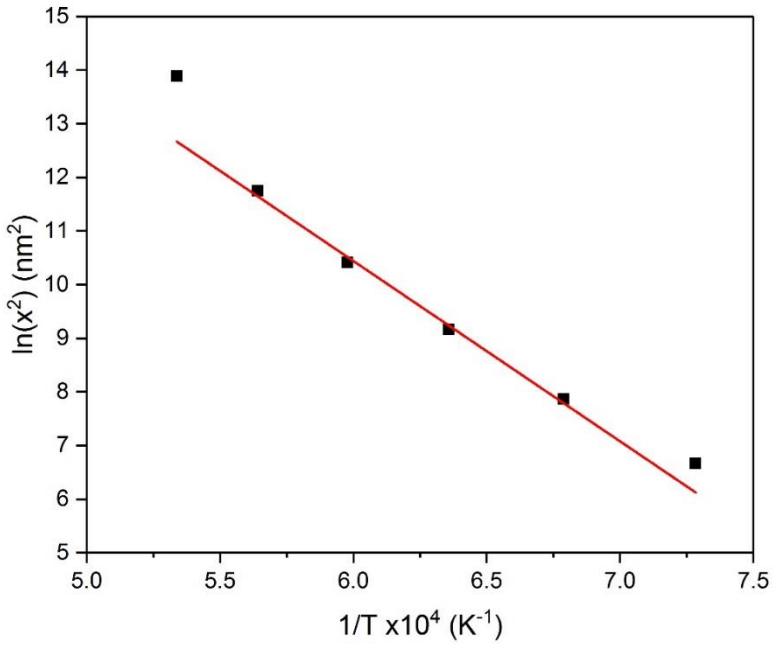

Fig. 17 The logarithm of x^2 vs the reciprocal of the annealing temperatures for all $Hf_7B_{23}Si_{22}C_6N_{40}$ films annealed in air. Linear fitting was done using data from films annealed to 1200, 1300, 1400 and 1500 °C.

Oxidation resistance of the $Hf_7B_{23}Si_{22}C_6N_{40}$ film was estimated by calculating the activation energy of oxygen diffusion using the same method mentioned in our previous work, and the results were presented in Table 1. It is worth mentioning that the calculated activation energy is just a rough portray of oxidation resistance because to obtain the correct parabolic relationship at certain temperature it is usually required to do isothermal annealing for several hours, which is not in our case. $Hf_7B_{23}Si_{22}C_6N_{40}$ film showed higher oxidation resistance compared to $Hf_7B_{23}Si_{17}C_4N_{45}$ film. The improved performance is largely due to the optimization of the deposition parameters that create a high quality defect-free surface [57]. The drop in activation energy for the sample annealed to 1600 °C matches with the significant increase in oxide layer thickness and could be explained by the reasons we mentioned before. Apart from

that, the activation energy sees an increasing trend vs the annealing temperature. It was previously concluded that the change in morphology of the oxide layer, especially the increase in thickness of *SL-I*, and the formation of quartz SiO_2 in *SL-I* at high temperatures could contribute to this [47].

Table 1. The oxide layer thickness and calculated oxygen diffusion activation energy of $Hf_7B_{23}Si_{22}C_6N_{40}$ films annealed to various temperatures in air.

Sample	Oxide layer thickness (nm)	Activation energy (eV)
1100 °C	28	3.47
1200 °C	51	3.58
1300 °C	98	3.65
1400 °C	183	3.71
1500 °C	356	3.74
1600 °C	1038	3.62

4.1.4.2 $Hf_7B_{23}Si_{22}C_6N_{40}$ Films Annealed to 1500 °C in Air: Oxide Layer

The details of microstructure of the $Hf_7B_{23}Si_{22}C_6N_{40}$ film annealed to 1500 °C and 1600 °C in air are presented through Fig. 18 to Fig. 29. Figs. 18a and 18b illustrate an overview of the oxide layer of the film annealed to 1500 °C from the perspective of cross-section and plan-view respectively, and the corresponding SAED pattern taken from plan-view TEM foil is presented in Fig. 18c. Due to the particle coarsening effect the diffraction from crystalline HfO_2 did not form complete ring patterns, instead, they split into scattered diffraction spots. Spots corresponding to the same lattice

parameter should be considered as the same “ring”. A total of 7 rings were identified. The first three correspond to d-spacing of 5.10, 3.67, 3.17 Å. These values match uniquely with lattice parameters in m-HfO_2. They were m-HfO_2 (100), (011) and ($\bar{1}11$), respectively. Ring 4 corresponds uniquely to o-HfO_2 (111), which was measured as 2.98 Å. Ring 5 is a superimposed diffraction ring which could correspond to at least 2 lattice parameters: 2.63 and 2.54 Å. The former matches with m-HfO_2/ o-HfO_2 (002), while

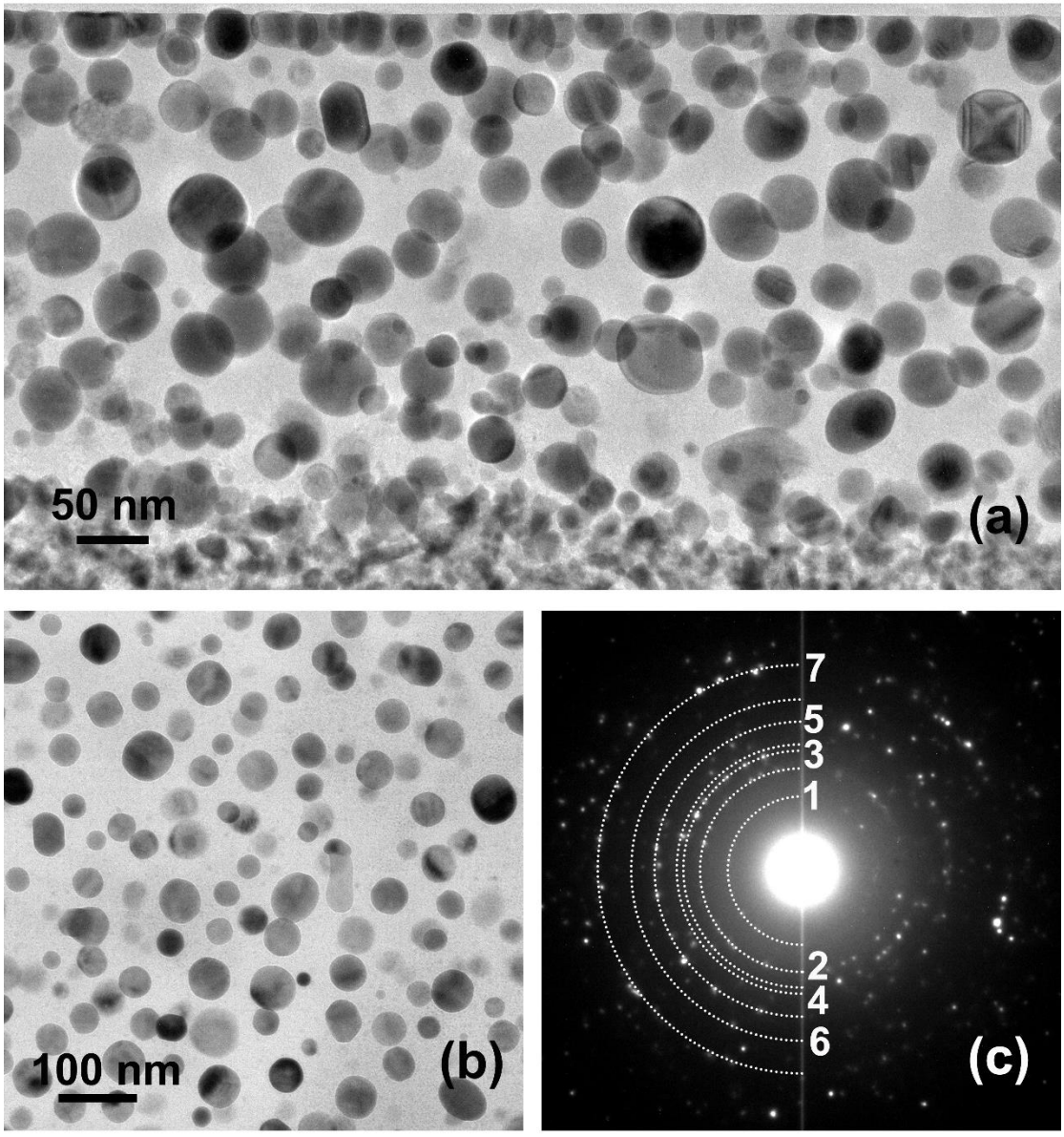

Fig. 18 The bright-field TEM image in view via (a) the cross-section and (b) the plan-view of the oxide layer in the $Hf_7B_{23}Si_{22}C_6N_{40}$ film annealed to 1500 °C in air and (c) the SAED pattern of the oxide layer taken from the PV-TEM sample.

the latter matches with m-HfO_2/ o-HfO_2 (200)/ (020). Ring 6 corresponds to a d-spacing of 2.21 Å, which could be identified as m-HfO_2 $(\bar{1}12)$ or $(\bar{2}11)$. Ring 7 is another superimposed diffraction ring and planes with lattice parameters of 1.82 to 1.85 Å corresponded to this ring. For m-HfO_2, it could be (220), (022) or $(\bar{2}12)$. For o-HfO_2, it could be (202) or (022). From the cross-section view of the oxide layer, the difference between two sublayers was not as evident as previous low-temperature samples. *SL-I* and *SL-II* mostly blended into each other, possibly due to strong particle coarsening. Particle size across the oxide layer could be as small as 16 nm, or as big as 60 nm. It generally became bigger in areas close to the film surface, but the trend was not obvious. Most particles on the film surface still exhibited abrupt cut-off from low-energy surfaces and incomplete spherical shape. Their size, compared to those within the matrix, was smaller and more uniform, mainly between 26 to 36 nm. It could be observed, however, that some particles extended out of the smooth matrix and their shape was also more complete, showing that the growth of these particle had overcome the surface energy restriction. More HRTEM images were taken from oxide layer and results were shown in Fig. 19. Fig. 19a is a HRTEM image taken from the cross-section TEM foil that illustrates both monoclinic and orthorhombic HfO_2 particles at the film surface. The particle on the left could be identified as m-HfO_2 with its $[1\bar{1}0]$ zone axis parallel to the beam. Monoclinic HfO_2 (111) plane, with measured d=2.85 Å and (002) plane, with measured d=2.63 Å were marked in the figure. The particle on the right could be identified as o-HfO_2 and its (111) plane with a d-spacing of 2.95 Å was identified. Fig. 19b is another HRTEM image taken from the oxide layer

just above the bottom layer. It was observed that extensive amount of quartz SiO_2 existed in this region. Both dimensions and density of these SiO_2 grew significantly compared to those within the film annealed to 1400 °C, suggesting that temperature increase promoted the formation of quartz SiO_2. However, this structure still only existed in the area close to interface. In the rest part of the oxide layer, the matrix is completely amorphous.

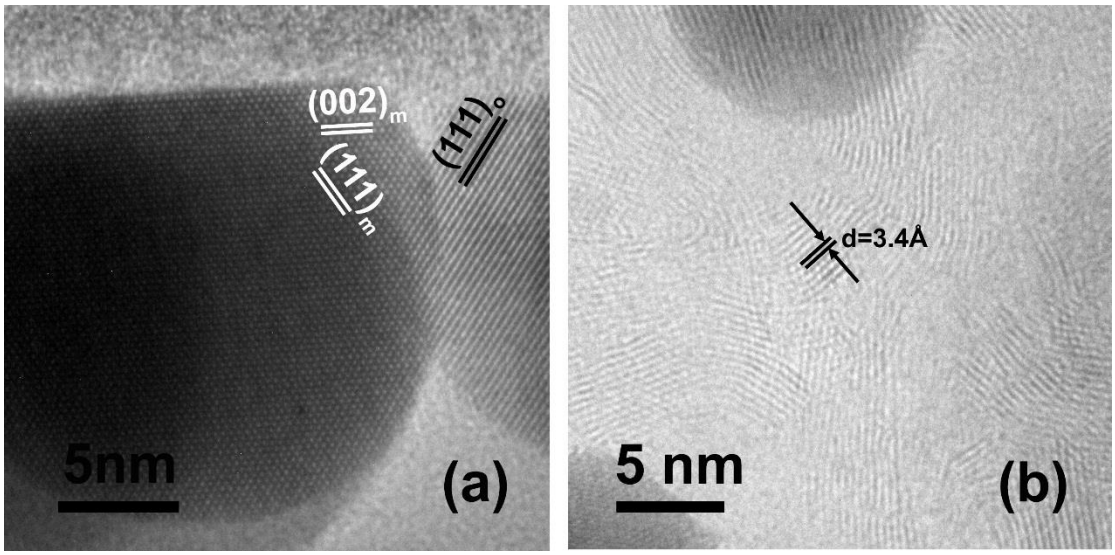

Fig. 19 HRTEM images of (a) HfO_2 particles near the film surface and (b) crystalline SiO_2 in the matrix near the interface between oxide layer and bottom layer in the $Hf_7B_{23}Si_{22}C_6N_{40}$ film annealed to 1500 °C in air.

4.1.4.3 $Hf_7B_{23}Si_{22}C_6N_{40}$ Films Annealed to 1500 °C in Air: Bottom Layer

The morphology of the bottom layer drastically changed compared to previous samples. Fig. 20a illustrates the overall structure of the recrystallized bottom layer, which shows fairly amount of complexity. Particles showing dark contrast with various shapes and sizes could be observed, while matrix with bright contrast filled in the space between these particles. The SAED pattern of this area is presented in Fig. 20b

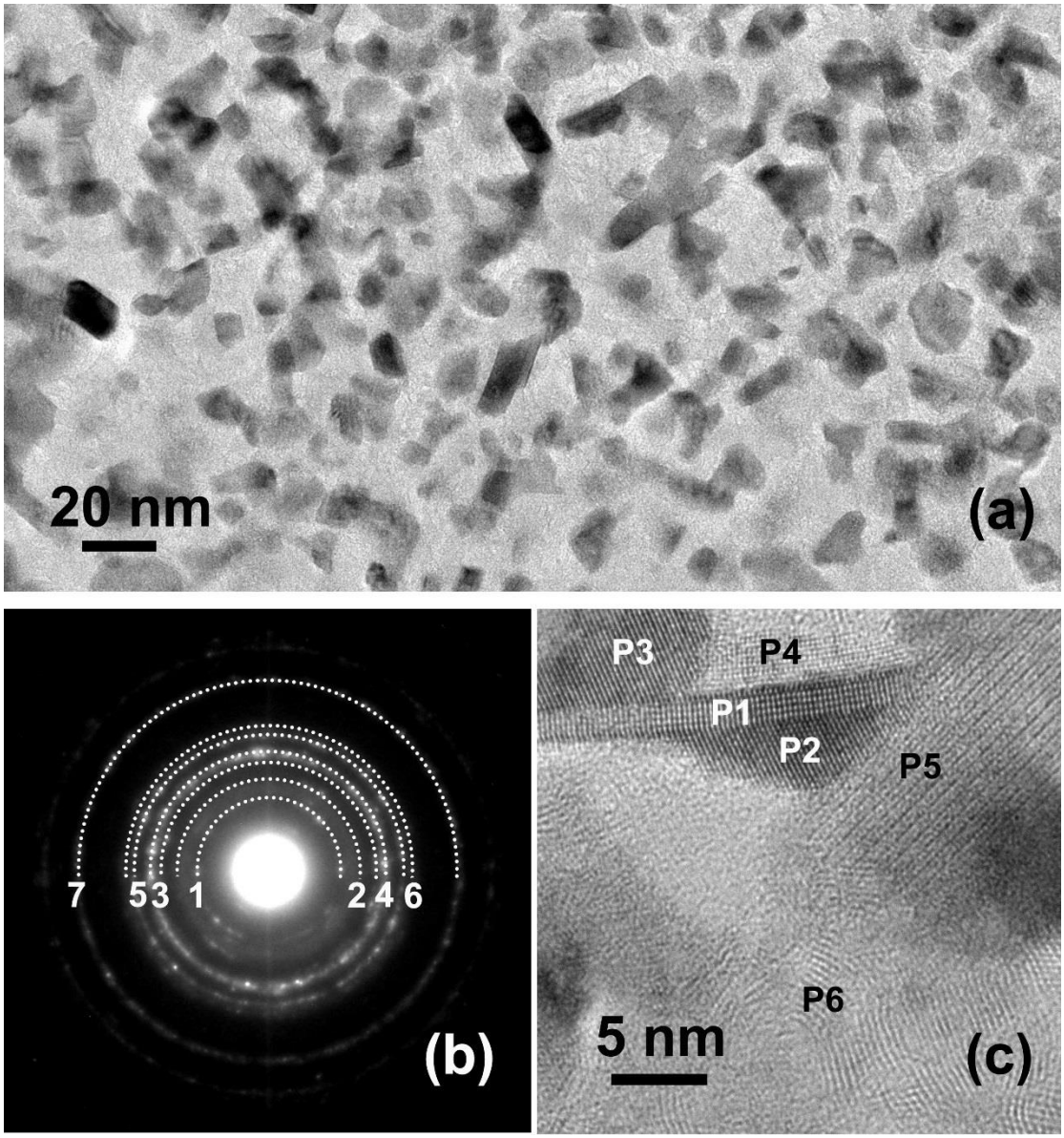

Fig. 20 (a) The bright-field TEM image, (b) the corresponding SAED pattern and (c) a zoom-in HRTEM image of the bottom layer in the $Hf_7B_{23}Si_{22}C_6N_{40}$ film annealed to 1500 °C in air.

showing clear polycrystalline diffraction rings. There are 7 rings in total, first three of which are diffraction from hexagonal Si_3N_4. They could be identified as Si_3N_4 (101), (200) and (201), corresponding to d-spacing of 4.33, 3.32 and 2.89 Å. The 4th and 5th ring correspond to the d-spacing of 2.63 and 2.30 Å and could be identified as HfN (111) and (200), respectively. What's more, Ring 6 could be identified as HfB_2 (101) and the corresponding lattice parameter is 2.17 Å. Finally, Ring 7 could be recognized

as HfN (220) which corresponds to the d-spacing of 1.61 Å. The presence of crystalline Si_3N_4 was verified by electron diffraction, while the development of crystalline HfN and HfB_2 also reasonably matched with the previous analysis. Fig. 20c is a zoom-in TEM image on the bottom layer illustrating some of the details. Immediately noticed was elongated particle P1 which could be identified as HfB_2 elongated along [100] direction. Jointed on the sides via (001) plane of HfB_2, which were denoted as P3, P4 and P5 are HfN. This combined HfB_2-HfN structure was observed and discussed in the sample annealed to 1400 °C. More HRTEM images showing this structure are presented in Fig. 21a through Fig. 21f. Through extensive HRTEM observation it was found that the structure existed throughout the whole bottom layer, and there's no evident trend regarding the size and shape distribution. However, there were some conclusions could be made: In all HRTEM images, HfB_2 had its [010] zone axis parallel to the beam, while HfN had its $[01\bar{1}]$ zone axis parallel to the beam, suggesting a certain crystallographic orientation relation between the two, which could be summarized as follows:

HfB_2-(001)//HfN-(111)

HfB_2-[100]//HfN-$[1\bar{1}0]$

HfB_2-[010]//HfN-$[01\bar{1}]$

Figs. 22a and 22b illustrate the crystal structure model of HfB_2 in view of [001] zone axis and HfN in view of [111] zone axis, respectively and the aforementioned parallel relationship is exhibited. In fact, HfB_2 and HfN joined together via a Hf monolayer, as marked in Fig. 21f. It was made possible based on the fact that both HfB_2-(001) and

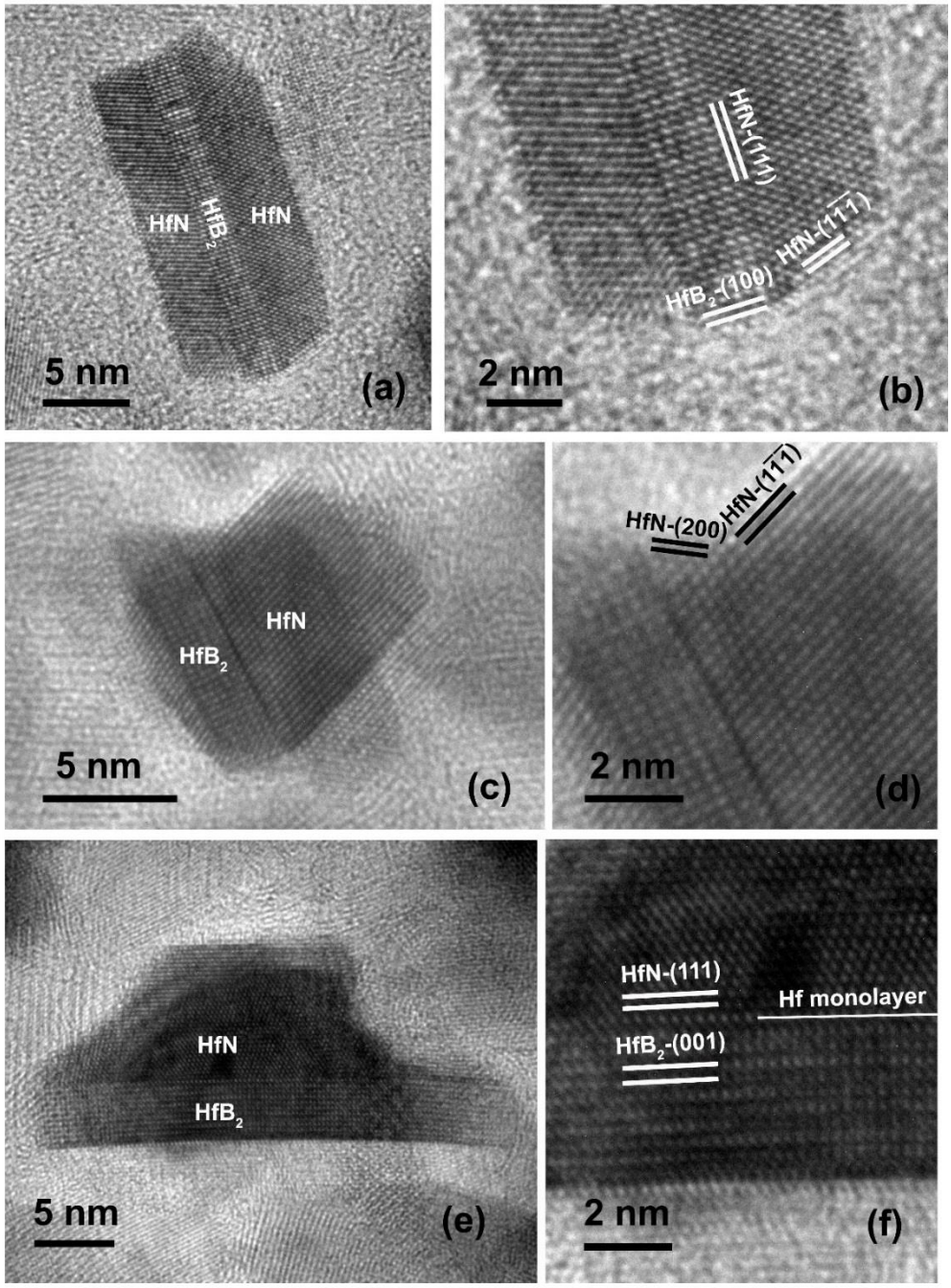

Fig. 21 HRTEM images of (a), (c) & (e) combined HfB_2-HfN structure in view of HfB_2 [010]/ HfN [$01\bar{1}$] and (b), (d) & (f) the zoom-in HRTEM image of the corresponding structure on the left.

HfN-(111) are the Hf close-packed planes in their corresponding structure and the Hf-Hf bond length within both planes are similar. For HfB_2 it is 3.14 Å while for HfN it is 3.21 Å, with a mismatch of about 2%. Fig. 22c illustrates the structure model of the interface between HfB_2 and HfN including the Hf monolayer and a HRTEM image

simulation on this particular area is presented in Fig. 22e using the defocus of 17 nm and thickness of 2.2 nm as the condition. In comparison, the actual HRTEM image is presented in Fig. 22d and the results are matched. The growth of HfB_2 always preferred [100] direction, resulting strong anisotropic structure. HfN, on the other side, did not have regular pattern regarding to the shape. In some cases, it demonstrated sharp edges, as in Figs. 21a and 21c. The reason behind the elongated shape of HfB_2 was possibly related to the interfacial energy. By reducing the dimension along the c-axis,

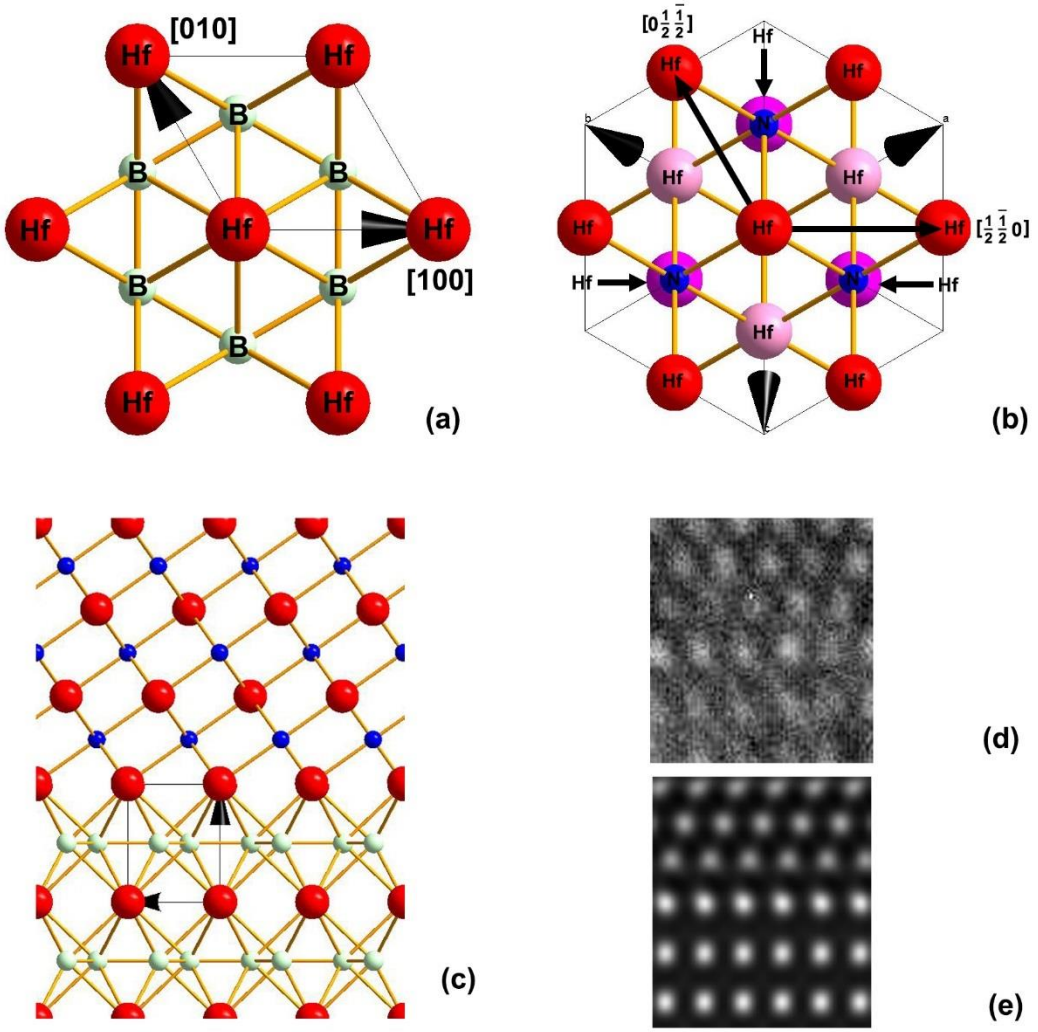

Fig. 22 Structural model of (a) hexagonal HfB_2 in view of [001] zone axis, (b) fcc HfN in view of [111] zone axis and (c) the interface between HfB_2 and HfN, (d) the actual HRTEM image and (e) the HRTEM image simulation on the interface.

much smaller high energy (100) plane would be exposed to the boundary areas compared to low energy (001) plane. The same explanation could be applied to the case of HfN. Apart from the (111) plane parallel to HfB_2-(001), HfN had tendency to expose more of its {111} planes instead of {100} according to our observation possibly due to lower surface energy. For example, the sharp edges in Figs. 21a and 21c are identified as Hf-$(1\bar{1}\bar{1})$. However, local atomic concentration and geometry restriction could've major impact too, especially when the size of the particle was relatively large, like the one shown in Fig. 21e. Individual HfN particles could also be found in the bottom layer. Fig. 23a presents the HRTEM image of two HfN particles with almost the same crystallographic orientation and both of them was in view of $[01\bar{1}]$ zone axis. (111) plane and (200) plane could be identified by analyzing the FFT pattern. Fig. 23b is another HRTEM image of HfN structure with very complicated shape. The d- spacing of the lattice fringes matches with HfN-(111). On the other hand, the Hf-free matrix was mostly occupied by crystalline Si_3N_4, shown as P5 in Fig. 20c. The d-spacing of the lattice fringes in P5 is 6.75 Å which could be identified as hexagonal Si_3N_4 (100). Fig. 24a illustrats another HRTEM image on the structure of Si_3N_4, along with the corresponding FFT pattern. The lattice parameters were measured as 4.33 and 3.92 Å. They could be identified as Si_3N_4 (101) and (110) respectively. The rest of the matrix was filled with heavily curved crystalline structure, shown as P6 in Fig. 20c. Another HRTEM image of this structure is presented as Fig. 24b. The measured d-spacing is 3.4 Å. It was determined to be hexagonal BN according to the image analysis, as well as the previous study on the high-temperature oxidation-resistant Si-B-C-N films. In the

annealed Si-B-C-N films, curved hexagonal BN was also observed [45].

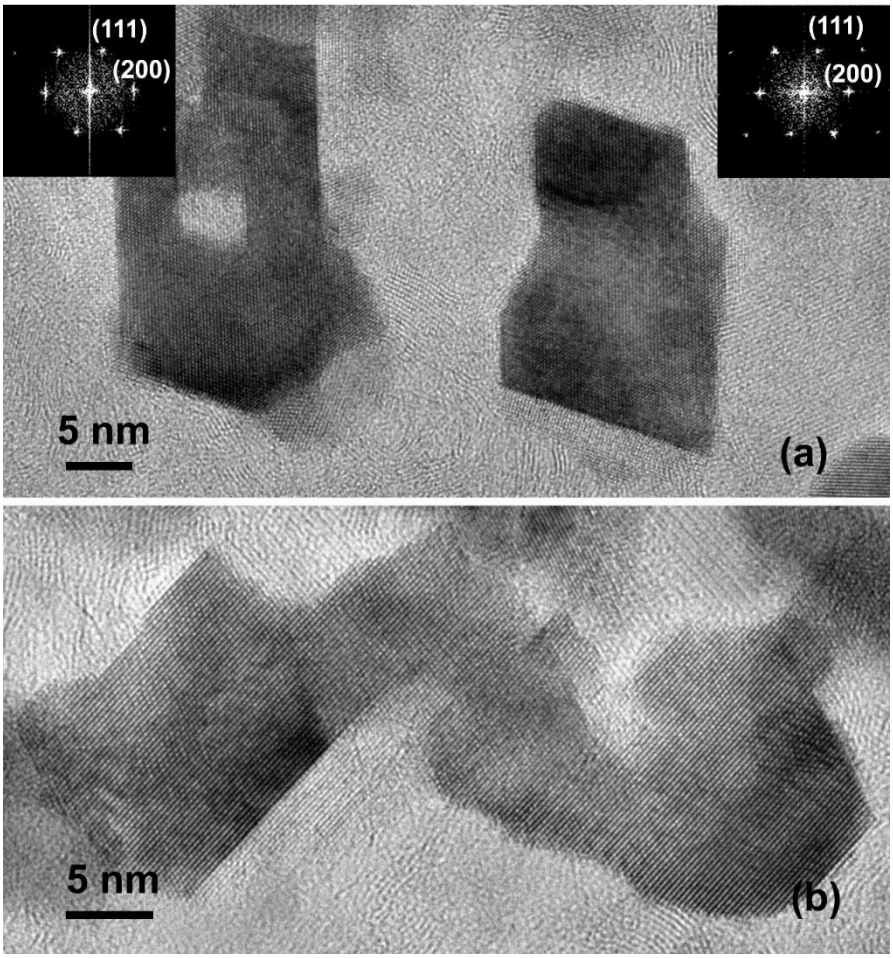

Fig. 23 (a) & (b) HRTEM images of HfN in the bottom layer of the $Hf_7B_{23}Si_{22}C_6N_{40}$ film annealed to 1500 °C in air.

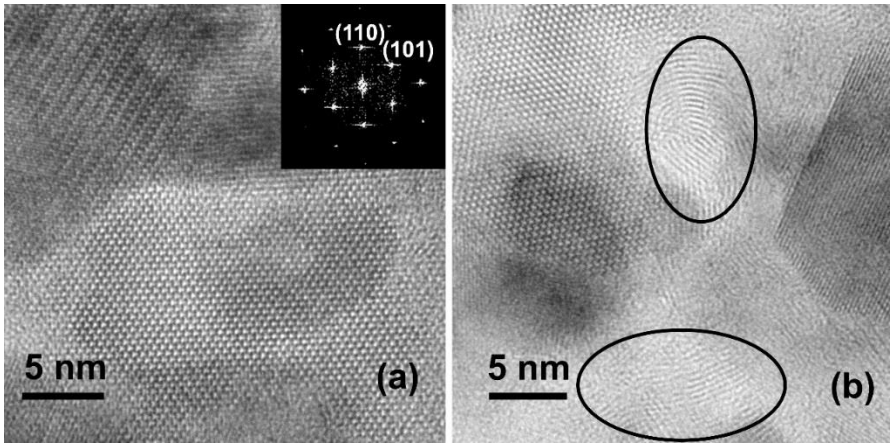

Fig. 24 HRTEM image of (a) Si_3N_4 and (b) BN (in black circle) in the bottom layer of the $Hf_7B_{23}Si_{22}C_6N_{40}$ film annealed to 1500 °C in air.

To summarize, at 1500 °C, the previously amorphous bottom layer of the film recrystallized into a polycrystalline structure. HfB_2 and HfN developed in the Hf-rich area, while Si_3N_4 and BN developed in the Hf-depleted area. The overall process of recrystallization could be described as follows: at the beginning, high temperature annealing gradually led to the agglomeration of Hf atoms, resulting more and more evident differentiation between Hf-rich areas and Hf- depleted areas. In Hf-rich areas, nucleation and initial growth of HfB_2 "strip" started at numerous nucleation sites, while the rest area remained amorphous. The microstructure thus gradually changed to a nanocrystalline composite structure. As temperature kept increasing, HfB_2 developed elongated shape along [100] direction, and kept consuming B atoms in the surrounding area. In the meantime, HfN started to form either as individual particles or by stacking Hf and N atoms at (001) plane of HfB_2 when there wasn't enough B supplement to support the growth of HfB_2. In the Hf-depleted area, Si and N developed Si_3N_4 structure, and the remaining B and N atoms formed h-BN structure trying to fill up the remaining space. The recrystallization did not follow epitaxial orientation, and the whole process should be considered independent from the oxidation since it initiated from the region close to substrate instead of the interface between oxide layer and bottom layer.

4.1.4.4 $Hf_7B_{23}Si_{22}C_6N_{40}$ Films Annealed to 1600 °C in Air: Oxide Layer

Annealing the $Hf_7B_{23}Si_{22}C_6N_{40}$ film to 1600 °C resulted in rapid oxidation of the film. The bright-field TEM image and SAED pattern of the oxide layer are presented in Fig. 25. The overall morphology revealed the development of oxide layer as expected

including the increase in thickness and particle size. The typical diameter of HfO_2 particles residing in the middle of the oxide layer was usually over 100 nm, which increased drastically compared to the sample annealed to 1500 °C. These particles did not have strictly spherical shape. A lot of them exhibited elongated or even cubic form and some of them showed barbell shape, which might be the sign of ongoing coalescence process by the migration and direct contact of two HfO_2 particles. This phenomenon was rarely observed in previous samples, which might result from the higher temperature and lower viscosity of the glass matrix that hindered the migration of HfO_2 to a less degree. The SAED pattern was analyzed and the result was close to that of the sample annealed to 1500 °C. A total of 7 rings were identified. They correspond independently to the d-spacing of 5.06, 3.63, 3.15, 2.83, 2.58/ 2.51, 2.30, 2.21 Å. The first one was identified as m-HfO_2 (100), while the second one as m-HfO_2 (011). The 3rd and 4th could be identified as m-HfO_2 ($\bar{1}11$) and m-HfO_2 (111), respectively. Ring 5 is a superimposed diffraction ring which could be identified as m-HfO_2 (200)/(020)/(002) or o-HfO_2 (200)/(020). Ring 6 could be identified as m-HfO_2 (120)/(021)/(012) or o-HfO_2 (102) and Ring 7 matches with m-HfO2 ($\bar{2}11$) or ($\bar{1}12$).

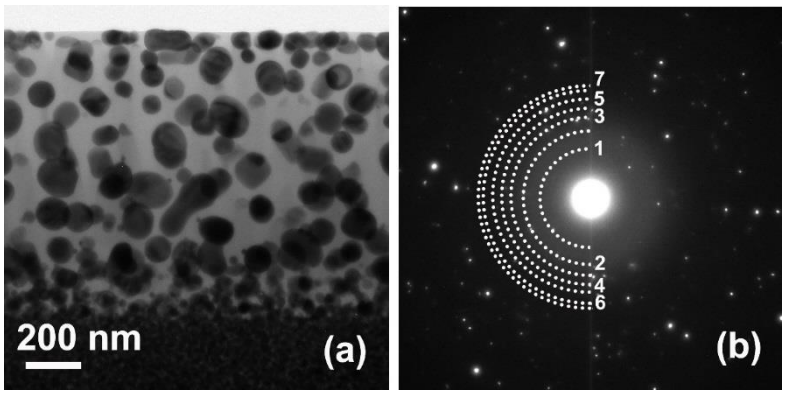

Fig. 25 (a) Bright-field TEM image and (b) SAED pattern in view via the cross-section of the oxide layer in the $Hf_7B_{23}Si_{22}C_6N_{40}$ film annealed to 1600 °C.

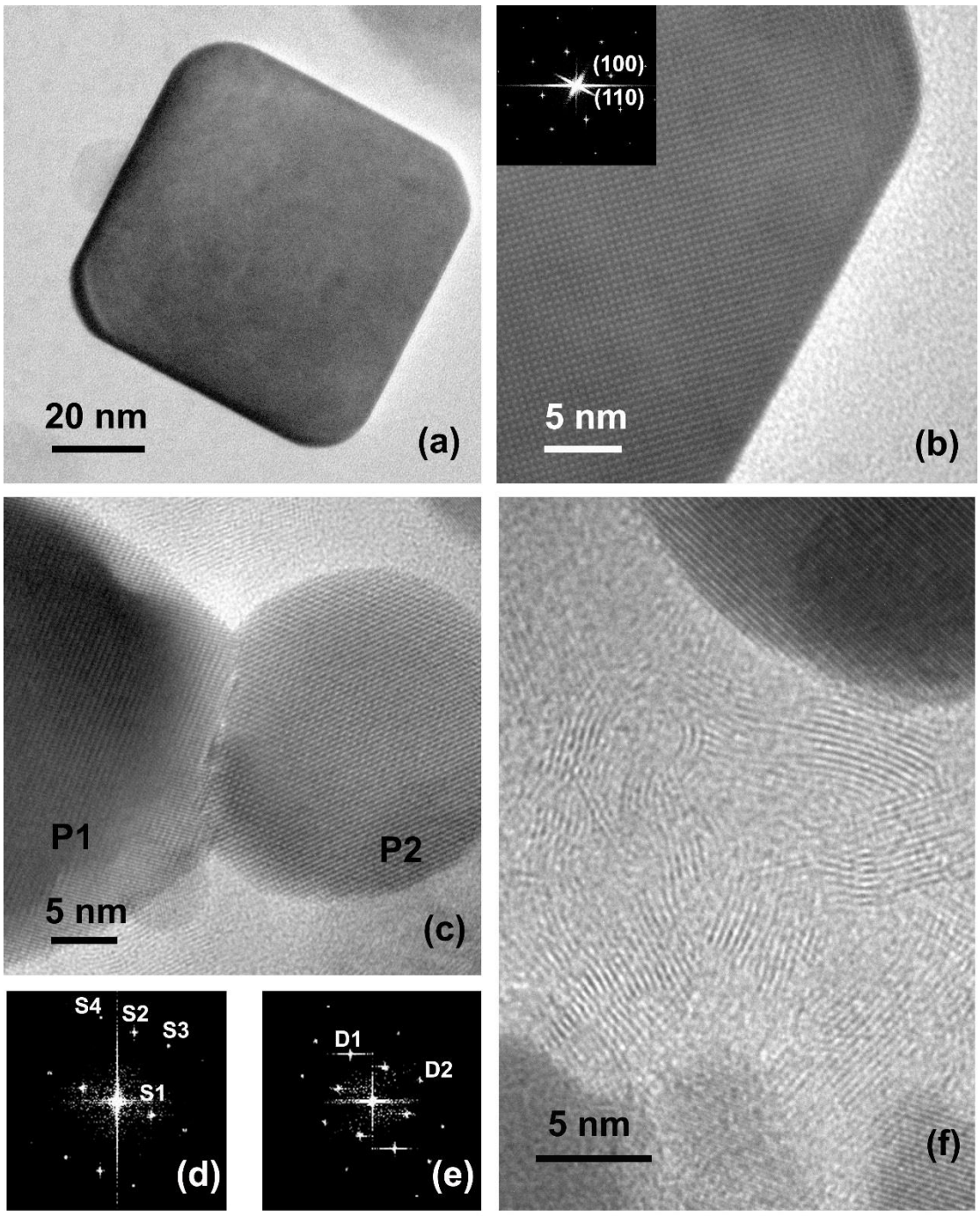

Fig. 26 HRTEM images on (a) & (b) a cubic-shape HfO_2 particle and (c) two HfO_2 particles possibly showing ongoing coalescence process, (d) & (e) FFT patterns illustrating the crystalline orientation of the particle P1 and P2 and (f) HRTEM image on the matrix close to the interface between oxide layer and bottom layer.

HRTEM image analysis was conducted on the HfO_2 particles, especially those which have shown different morphology. Figs. 26a and 26b illustrated a HfO_2 particle in cubic shape. HRTEM image analysis showed that all 4 visible edges of the cube were

parallel to {110} plane. First principle calculations of the structural properties of HfO_2 surfaces done by Mukhopadyay *et al.* reported that m-HfO_2 (110) has higher surface stability than both (100) and (010) planes [58], which could be the main reason that the exposure of {110} planes to the matrix is larger than {100} planes in this case. Fig. 26c illustrates two monoclinic HfO_2 particles joined together. Particle P1 had its [010] zone axis orientated parallel to the beam. In the FFT of the crystalline structure (Fig. 26d), diffraction spot S1 and S2 could be identified as m-HfO_2 ($\bar{1}00$) and (002), with a measured d-spacing of 5.08 Å and 2.62 Å, respectively. Meanwhile, S3 and S4 correspond to the d-spacing of 2.49 and 2.17 Å, which match with m-HfO_2 ($\bar{1}02$) and (102), respectively. On the other hand, particle P2 could be also identified as m-HfO_2 having [100] zone axis parallel to the beam. Diffraction spot D1 and D2 in Fig. 26e both correspond to the d-spacing of 3.69 Å and could be identified as m-HfO_2 {011}. P2 joined P1 via its (010) plane and P1 joined P2 via its (100) plane. The lattice mismatch led to the incoherence of the interface. Figs. 27a and 27b illustrate the structure model of O-rich (100) plane in view of [010] direction and Hf-rich (010) plane in view of [100] direction, respectively. In both planes, unsaturated surface atoms were marked and in terms of charge neutrality, they both have 6 unsaturated Hf-O bonds per unit cell, meaning that there won't be excessive Hf-O bonds when the two planes join together. On the other hand, the matrix generally showed similar morphology as the sample annealed to 1500 °C. While most part maintained amorphous, the area that is close to the interface was occupied by crystalline SiO_2, with higher density than any of the previous samples, as illustrated in Fig. 26f.

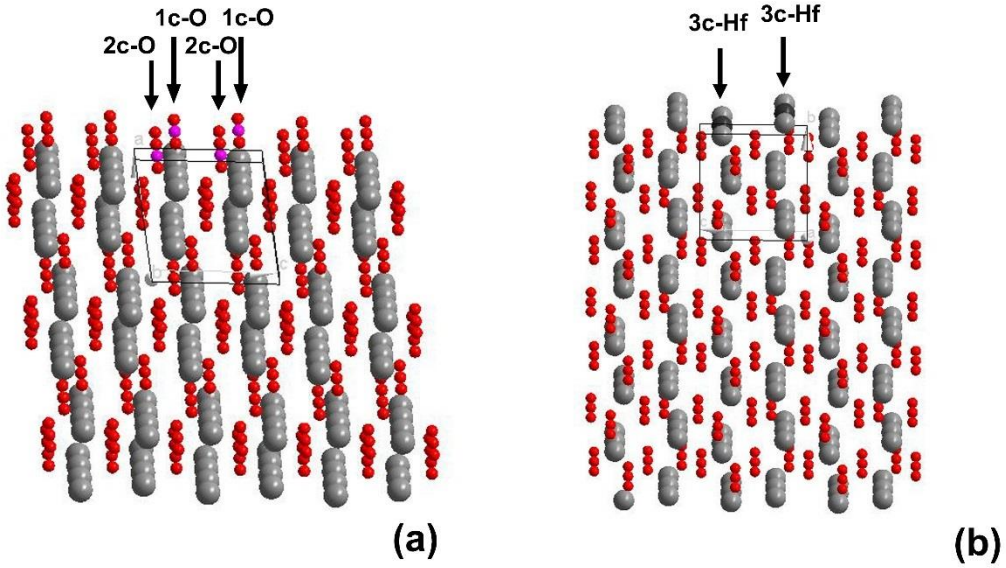

Fig. 27 The structural model showing o-rich m-HfO_2 (100) plane and Hf-rich m-HfO_2 (010) plane. Red solid balls are O atoms and grey solid balls are Hf atoms. The unsaturated atoms on the surface within the same unit cell are marked in slightly different color (pink and black).

4.1.4.5 $Hf_7B_{23}Si_{22}C_6N_{40}$ Films Annealed to 1600 °C in Air: Bottom Layer

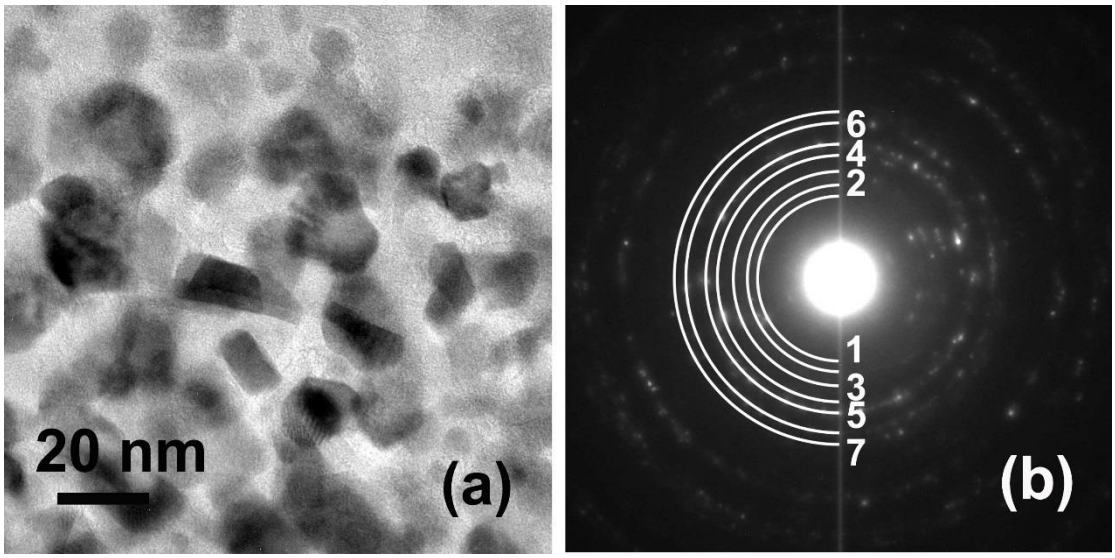

Fig. 28 (a) Bright-field TEM image and (b) SAED pattern of the bottom layer in the $Hf_7B_{23}Si_{22}C_6N_{40}$ film annealed to 1600 °C.

Analysis on the bottom layer demonstrated that no significant changes regarding to the microstructure can be concluded when compared with the film annealed to 1500 °C. Fig. 28 illustrates a bright-field TEM image and an SAED pattern on the bottom

layer of the $Hf_7B_{23}Si_{22}C_6N_{40}$ film annealed to 1600 °C. A total of 7 diffraction rings were identified in Fig. 28b and despite the pattern showed some difference compared to the one of 1500 °C, the analysis arrived at the same conclusion. Table 2 summarizes the results of the analysis. Detailed HRTEM images yielded no significant changes of the microstructure, as shown in Fig. 29. Combined HfB_2-HfN and independent HfN formed the skeleton, while the matrix consisted of Si_3N_4 and BN. It was most likely that the bottom layer remained stable in the temperature range between 1500 and 1600 °C until it was oxidized as the interface gradually progressed inward, eliminating the crystalline structure of the bottom layer and replacing it with the oxide layer.

Table 2 The comparison of SAED ring patterns taken from the bottom layer in the $Hf_7B_{23}Si_{22}C_6N_{40}$ film annealed to 1500 °C (left column) and 1600 °C (middle column).

d-spacing (Å) (1500°C)	d-spacing (Å) (1600°C)	Index
4.33	4.32	h-Si_3N_4 (101)
3.32	-	h-Si_3N_4 (200)
2.89	2.95	h-Si_3N_4 (201)
2.63	2.63	HfN (111)
2.30	2.30	HfN (200)
2.17	2.13	HfB_2 (101)
-	1.82	h-Si_3N_4 (103)
1.61	1.63	HfN (220)

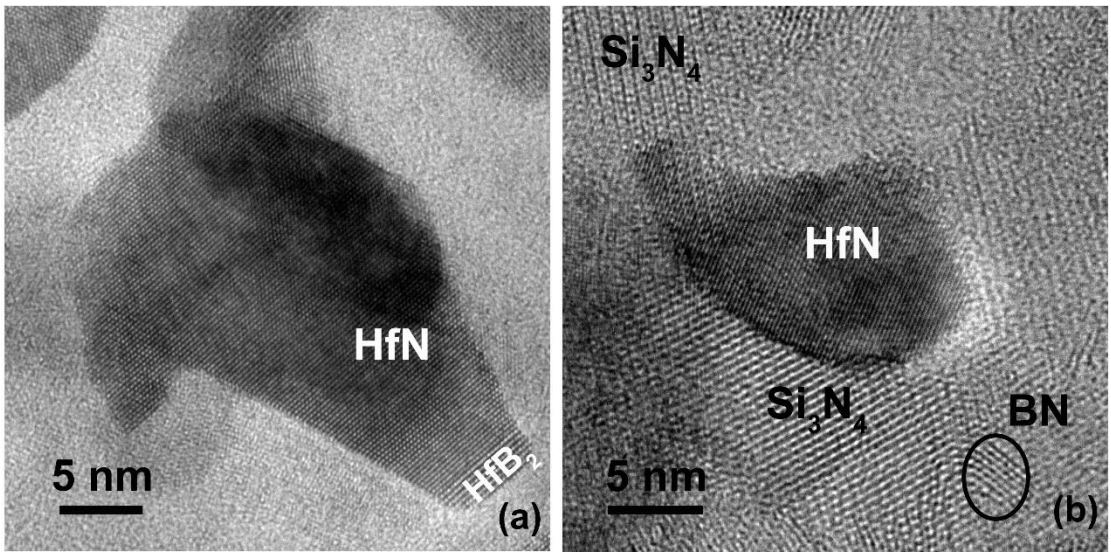

Fig. 29 HRTEM image of the bottom layer in the $Hf_7B_{23}Si_{22}C_6N_{40}$ film annealed to 1600 °C illustrating (a) combined HfB_2-HfN structure and (b) independent HfN particle surrounded by Si_3N_4 and BN matrix.

4.1.5 The Interface between Oxide Layer and Bottom Layer

The interface, where the oxidation and the transition of the microstructure occurred, was also part of the TEM microstructure analysis. Fig. 30a illustrates the interface between the oxide layer and bottom layer in the $Hf_7B_{23}Si_{22}C_6N_{40}$ film annealed to 1400 °C in air. This represents the typical microstructure of this particular area in this sample, as well as samples annealed to lower temperatures. In these samples, a clear interface between the bottom layer and top layer was observed. It is because the bottom layer of these samples was either homogeneous amorphous, or mostly amorphous with small nanocrystalline particles scattered uniformly and the oxidation happened at the same rate across the interface. Nucleation of HfO_2 could be observed at the interface. For example, in Fig. 30a, small HfO_2 nuclei were marked by black circles denoted as N1 and N2. These nuclei were usually in the range of 1 to 2

nm and contained only several lattice planes that barely formed visible crystalline structure. As oxidation continued, the interface progressed inwards, leaving these nuclei behind, while at the same time, initial growth of the nuclei happened as they kept consuming the oxygen species and unreacted Hf in the surrounding area, which can be seen as small particles P1, P2, P3 and P4. These particles were significantly larger than the initial nuclei, usually in the range of 5 to 8 nm. Lattice fringes could be clearly observed. For example, the lattice fringes in particle P2 and P4 had d-spacing of 2.94 and 2.96 Å, respectively, and were identified as o-HfO_2 (111). The shape of these particles was usually not spherical, showing that the interfacial energy was not dominant during this stage of growth. The surrounding matrix of these particles would gradually be depleted of Hf, which was indicated by the change of contrast in the amorphous matrix. In the meantime, the growth of HfO_2 particles continued. These particles, shown as G1 and G2 in Fig. 30a, were spherical in attempt to minimize the surface energy. The supplement of oxygen was most likely from the surrounding matrix, while the supplement of Hf needed to be from the surrounding matrix, if there was still unreacted Hf left, or from other HfO_2 particles. The latter one, which was mentioned before as Ostwald ripening process, is a diffusional mass transfer process from regions of higher interfacial curvature to regions of lower interfacial curvature in a two-phase mixture environment. And since it is an atomic-scale diffusional process, the shape of these particles will not be influenced, which matched with our observation results that up to 1400 °C the HfO_2 particles maintained ideal spherical shape in the oxide layer. We believe that at lower temperatures, i.e., 1100 °C and

1200 °C, HfO_2 growth via consuming Hf atoms from the matrix played a more important role since the size distribution of the HfO_2 particles was rather uniform in both the sample annealed to 1100 °C (Fig. 3b and 4a) and 1200 °C (Fig. 3d and 6a) which suggested a uniform growth rate of all HfO_2 particles without sacrificing smaller ones. However, at higher temperatures, i.e., 1300 °C and 1400 °C, Ostwald ripening process started to become more and more dominant, as we could observe a wider size distribution of HfO_2 particles in both samples (Fig. 3f and Fig. 10a) which was an indication of ongoing coarsening process. The oxide layers in both samples were divided into two sublayers, and it was possible that while two growth mechanism might co-exist in *SL-I*, the supplement of unreacted Hf in the matrix completely exhausted at the interface between *SL-I* and *SL-II* and in *SL-II*, Ostwald ripening process became the only growth mechanism of HfO_2.

The morphology of the interface changed drastically when the annealing temperature increased to 1500 °C and Fig. 30b is a HRTEM image representing the microstructure of the interface. Since the bottom layer had recrystallized, the oxidation process had to eliminate of the pre-existing crystalline structure at first. As a result, the interface was not as clear as that in the sample annealed to 1400 °C or to lower temperatures and no visible nucleation site could be seen at the interface. The analysis on the unreacted bottom layer microstructure revealed that the crystalline structure was not altered notably even when the interface was approached. For example, the analysis of the HfB_2 strip in Fig. 30b showed that the lattice parameter of its (100) plane was almost identical to those similar structures within the volume of

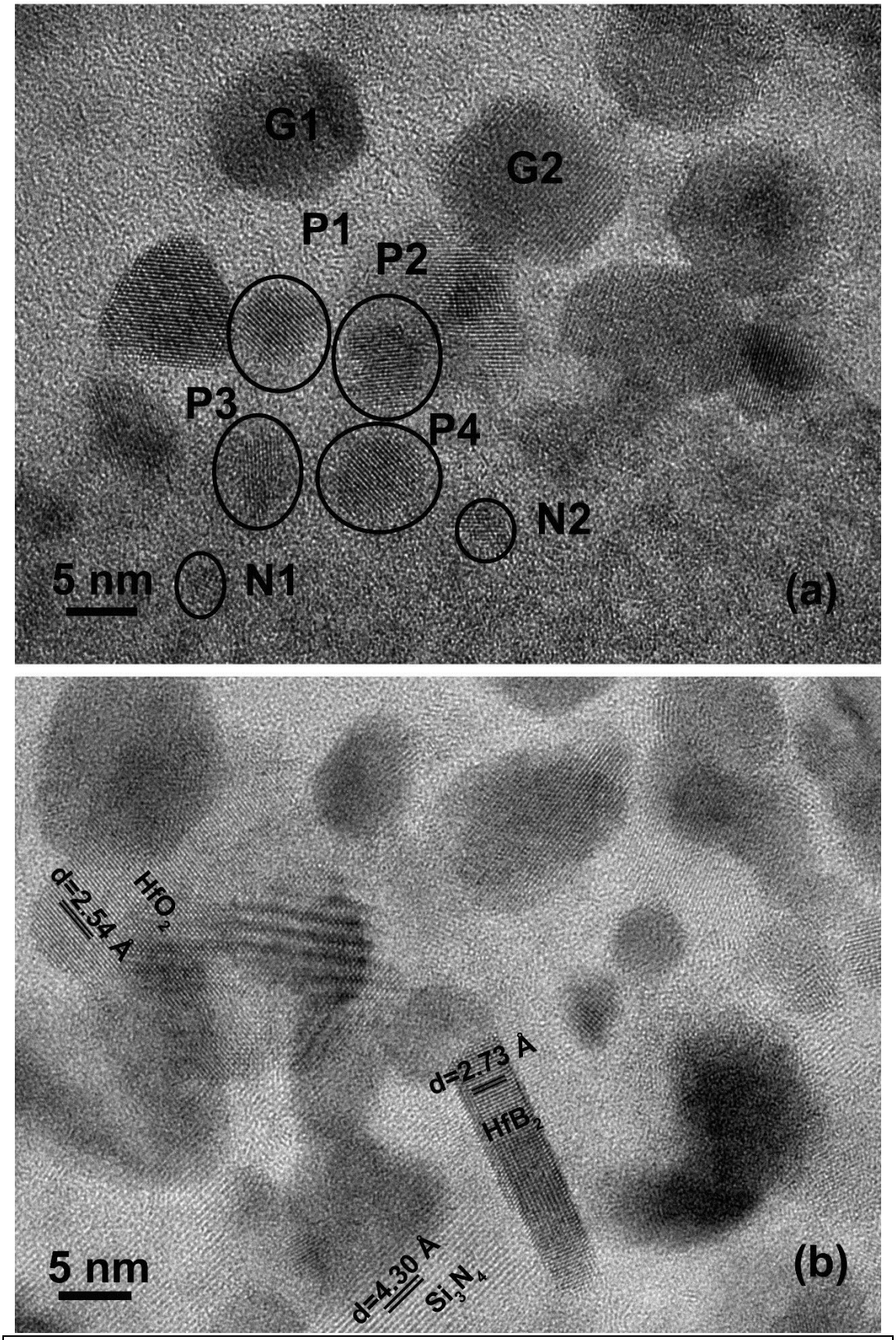

Fig. 30 HRTEM images on the interface between the oxide layer and bottom layer in the $Hf_7B_{23}Si_{22}C_6N_{40}$ film annealed to (a) 1400 °C and (b) 1500 °C in air.

the bottom layer. The same conclusion could be applied to the Si_3N_4, too. The lattice fringes of the matrix area in the lower part of Fig. 30b had a d-spacing of 4.30 Å, which matched closely with previously analyzed Si_3N_4 (101) within the volume of the bottom layer (Fig. 20b and 24a). Moreover, the crystalline oxidation product at the interface could be identified as HfO_2 with ease and while some of them were small, others were over 20 nm in size which indicated the formation of these particles did not involve progressive nucleation and initial growth. Extensive TEM analysis throughout different locations of the interface suggested that no Hf-containing intermediate oxidation product, for example hafnium oxynitride, formed during the reaction. The microstructure transition occurred by dissolving the original elements of the film from their respective crystalline structures and reassembling them into their final products. The huge size variation of HfO_2 even at the interface was possibly determined by varied local Hf atomic concentration after they dissolved from HfB_2 and HfN which matched with the wide size distribution of HfN and HfB_2 in the bottom layer. The oxidation of Si_3N_4 and BN resulted in a Hf-deficient matrix at the interface. This suggests that HfO_2 could hardly absorb any unreacted Hf from the matrix to support its growth and Ostwald ripening process became dominant across the whole oxide layer. As a result, the two sublayers that existed in the oxide layer of lower-temperature samples blended into each other.

4.1.6 Oxidation Mechanism

Overall, the oxidation process of the film could be described as follows: upon

reaching the annealed film surface, oxygen was absorbed and reacted with the homogeneous amorphous film. Oxygen that reacted with Hf formed HfO_2, and that reacted with B formed the initial B_2O_3 glass layer that covered the whole film continuously. As annealing temperature increased, more oxygen would be absorbed and then diffused through the glass layer, reacting with the film and pushing the interface between oxide layer and bottom layer inwards. During the process, the reaction between Hf and O resulted HfO_2 nucleation at the interface while the reaction of between B and O, as well as Si and O would form the matrix surrounding the HfO_2 nuclei. Nitrogen was likely to form and bubble through the oxide layer before being released to the ambient. Due to the glassy nature of the matrix, this step did not cause catastrophic failure of the oxide layer. HfO_2 nuclei would then absorb unreacted Hf and O within the matrix to grow, the matrix was likely to absorb oxygen too and the diffused oxygen would be continuously consumed. As a result, the amount of oxygen that reached the interface was less than that absorbed by the film surface. Once the thickness of the oxide layer passed 50 nm, the oxidation would reach a steady state when the oxide thickness was in parabolic relationship with annealing temperature and oxygen diffusion became the rate-limiting factor. As temperature kept increasing to about 1300 °C, the growth of HfO_2 eventually depleted all unreacted Hf in the matrix and further growth would rely solely on the diffusional mass transfer between these HfO_2 particles (i.e., Ostwald ripening process). The oxide layer was then split into two sublayers: in *SL-I*, the matrix was close enough to the interface and some unreacted Hf was left. The growth of HfO_2 would consume the Hf in the nearby matrix, as well as

from smaller HfO_2 particles as discussed earlier. However, in *SL-II*, the matrix no longer contained Hf and oxygen diffused through this sublayer was not likely to be consumed by HfO_2. Apart from the gradual depletion of Hf, the composition of the matrix changed constantly during oxidation as the oxidation rate of different elements was not the same. At this temperature, boron was likely to be fully oxidized into boron oxide and some of that could be released from the film together with N_2 while silicon was much more stable. Details of the composition change in the matrix was hard to determine given the current experiment conditions. As temperature kept increasing, the diffusivity of Hf within matrix increased, and the particle coarsening effect was more and more evident. Smaller HfO_2 particles would shrink and finally disappear and larger ones would continue to grow. In the meantime, quartz SiO_2 formed within the matrix and the recrystallization of the bottom layer happened independently as discussed in the previous paragraphs until the fully recrystallized bottom layer reached the interface. The oxidation kinetics then changed from oxidation of the bottom layer as a whole, to oxidation of different crystalline structures from the bottom layer separately. The oxidation of HfB_2 and HfN happened via dissolving Hf from original structures to produce HfO_2, while the oxidation of Si_3N_4 and BN resulted in dissolving Si and B to form borosilicate glass. The matrix was likely Hf-deficient and no growth of HfO_2 via consuming Hf from matrix was possible. The difference between two sublayers of the oxide layer was then insignificant. Large amount of quartz SiO_2 would form at the interface between the oxide layer and bottom layer. At temperatures above 1500 °C, the fact that no more oxygen consumption via particle growth resulted in

higher concentration of oxygen at the interface between the oxide layer and bottom layer. To add on to that, oxidation of the bottom layer happened by oxidation of individual crystalline grains, which created local oxidation rate variation. This is most likely the reason behind a rough interface between the oxide layer and bottom layer. This rough interface would likely extend the effective oxidation interface compared to the smooth interface in samples annealed to lower temperatures. These factors, together with higher liquidus temperature and lower viscosity of the borosilicate glass likely contributed to the lower activation energy and faster oxidation kinetics of the film annealed to 1600 °C.

The thermogravimetric results of the $Hf_7B_{23}Si_{22}C_6N_{40}$ film measured in air demonstrated extremely low mass changes (± 5 μg/cm^3) after annealing up to 1300 °C [57] which is a clear indication of superior oxidation resistance. The TGA result should be considered as a competition between oxidation (O_2 absorption) and volatilization (N and B losses). Microstructure-wise, the superior oxidation resistance of the $Hf_7B_{23}Si_{22}C_6N_{40}$ film is mainly attributed to the formation of a continuous top oxide layer. In all annealed samples, this layer was observed maintaining its structural integrity which was not damaged by volatilization process. The oxidation rate was successfully limited as oxygen needed to diffuse through the oxide layer to react with the film. In samples annealed to 1400 °C and below, the process was further limited by the presence of *SL-I* that consumed oxidizing species and the dense atomic network of the amorphous structure in the bottom layer. At higher temperatures, the dense array of HfO_2, as well as quartz SiO_2 precipitated at the bottom of the oxide layer,

helped forming a thermal and diffusion barrier thanks to the low thermal conductivity of HfO_2 and high density of quartz SiO_2.

4.2 Microstructure Evolution of $Hf_7B_{23}Si_{22}C_6N_{40}$ Films Annealed to Various Temperatures in Helium

4.2.1 TEM Study

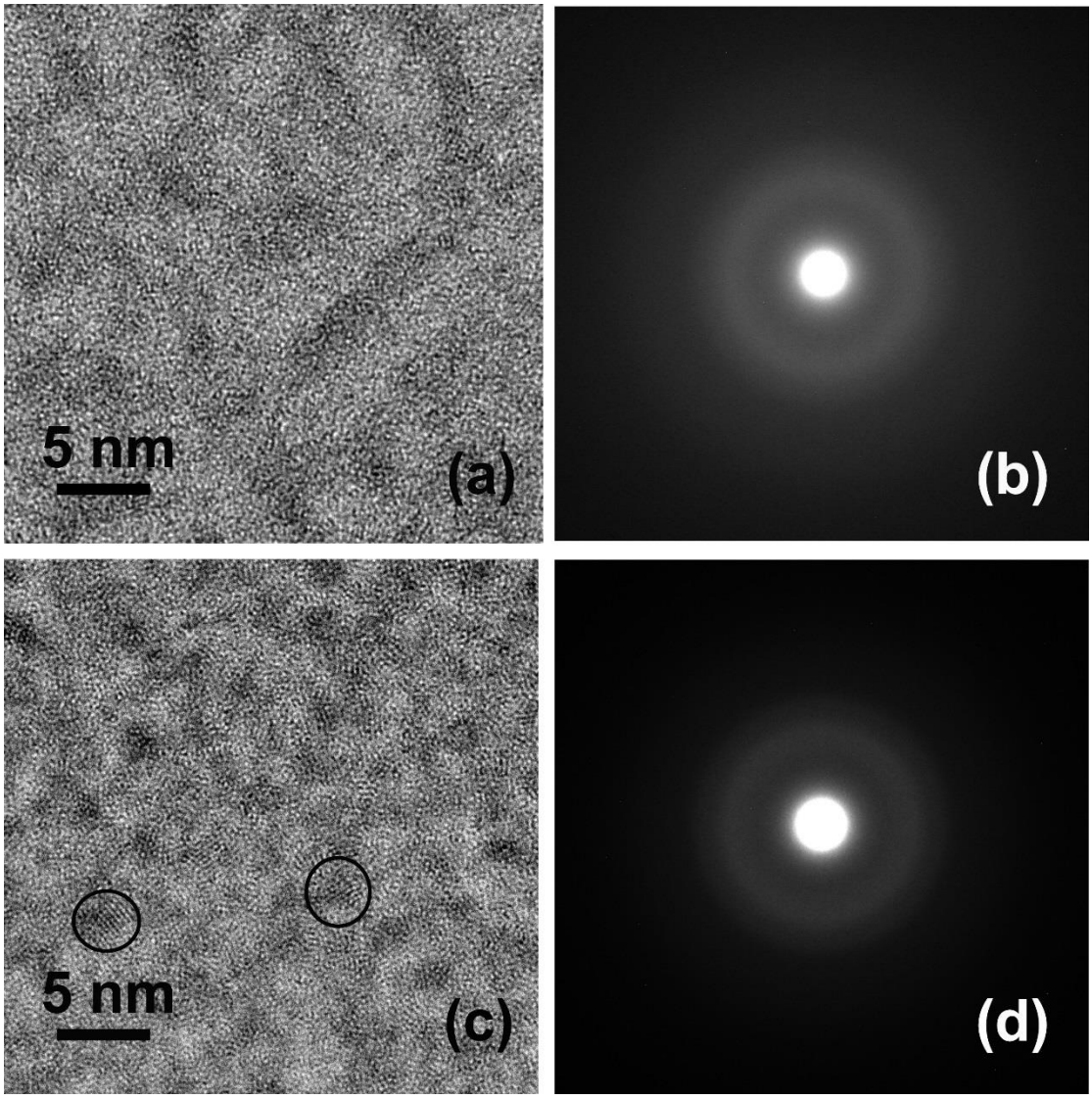

Fig. 31 A HRTEM image of (a) the $Hf_7B_{23}Si_{22}C_6N_{40}$ film annealed to 1100 °C in helium and (c) the $Hf_7B_{23}Si_{22}C_6N_{40}$ film annealed to 1200 °C in helium. The corresponding SAED pattern of each sample is presented on the right side of the image.

Annealing the $Hf_7B_{23}Si_{22}C_6N_{40}$ films in helium did not result in tremendous changes in the microstructure as observed with annealing in air. Fig. 31a shows the HRTEM image of the film annealed to 1100 °C in helium. The microstructure was

homogeneous amorphous and almost identical to the as-deposited film as confirmed by the SAED pattern (Fig. 31b). Fig. 31c is a HRTEM image illustrating the microstructure of the film annealed to 1200 °C in helium. Small nanocrystalline clusters could be observed as dark circles marked in the figure. The average size of these nanocrystalline clusters was only about 2 nm and they hardly show visible lattice fringes. The SAED pattern (Fig. 31d) of this film does not show clear diffraction rings

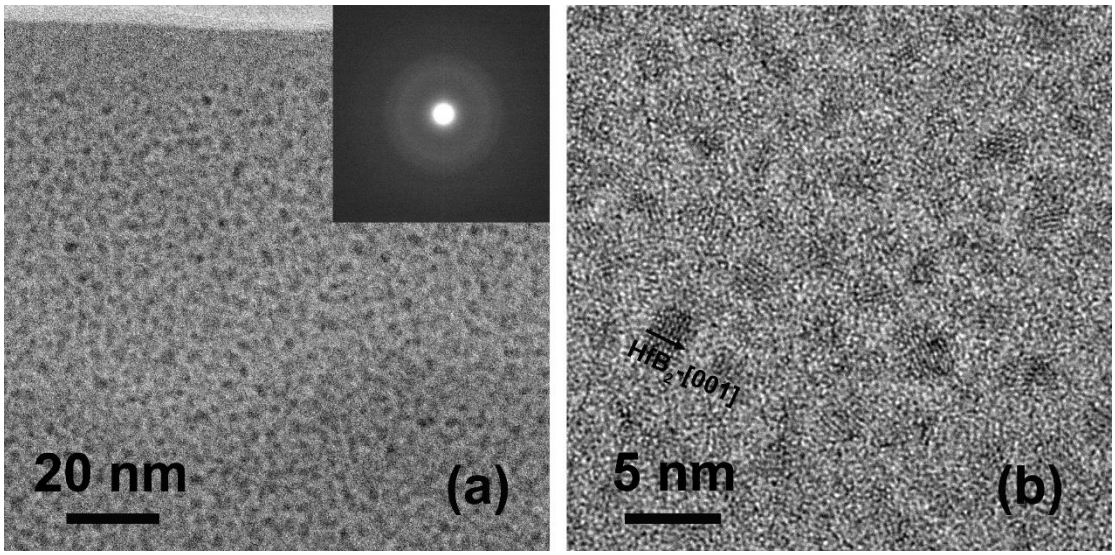

Fig. 32 (a) Bright-field cross-section TEM image and (insertion) the corresponding SAED pattern of the $Hf_7B_{23}Si_{22}C_6N_{40}$ film annealed to 1300 °C in helium taken from the region close to surface and (b) the HRTEM image illustrating the nanocrystalline composite structure of the film.

from any crystalline structure either. This result suggested that annealing to 1200 °C in helium did not change the microstructure of the film significantly, but the transition from a homogeneous amorphous structure to a nanocrystalline composite structure was underway, similar to annealing the same film in air. Fig. 32a is a bright-field cross-section TEM image taken from the $Hf_7B_{23}Si_{22}C_6N_{40}$ film annealed to 1300 °C. The area of interest in this image is near the film surface. Numerous Hf-rich clusters could be observed scattered within the film and HRTEM images illustrate that these clusters

were HfB_2 nanocrystalline particles with visible lattice fringes. Fig. 32b is a representative HRTEM image illustrating the details of the microstructure. The average size of the nanocrystalline particles was less than 5 nm. The particle with an arrow in the center was identified as a HfB_2 strip-like structure with the arrow pointing out its [001] zone axis. However, SAED pattern, shown as an insert in Fig. 32a, fails to provide the crystallographic information of the HfB_2 nanocrystalline particles due to their extremely small size and poor crystallinity.

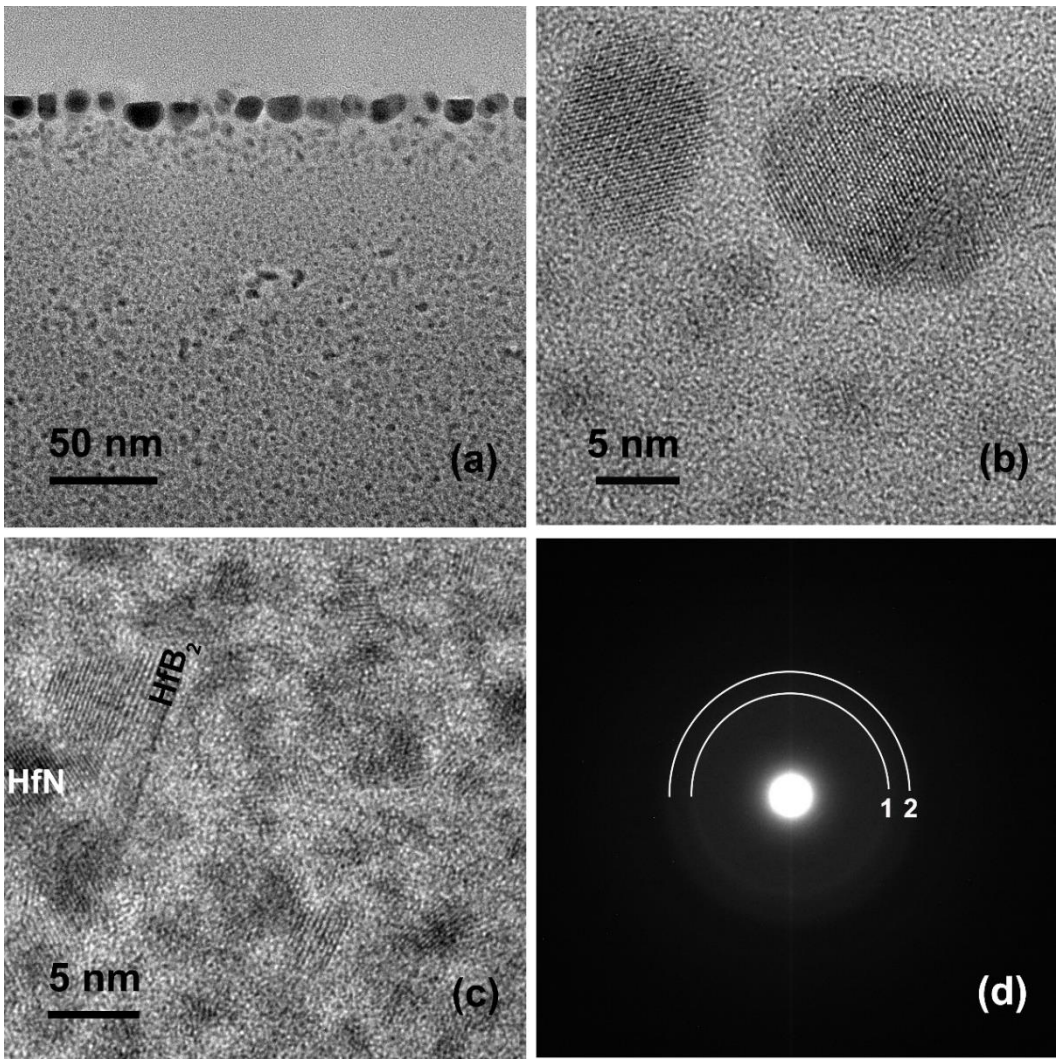

Fig. 33 (a) Bright-field cross-section TEM image of the $Hf_7B_{23}Si_{22}C_6N_{40}$ film annealed to 1400 °C in helium, (b) HRTEM image of the surface oxides, (c) HRTEM image of the nanocrystalline composite structure of the film and (d) the corresponding SAED pattern.

The nanocrystalline composite structure continued to develop when annealing temperature increased to 1400 °C, along with some other changes. Fig. 33a is a bright-field cross-section TEM image of the film annealed to 1400 °C in helium. It is noticeable that a very thin oxide layer could be seen formed on the surface that did not appear in any previous sample. The thickness of the layer was roughly 30 nm, consisting of a dense single-layer HfO_2 array with small HfO_2 nuclei underneath. A HRTEM image of the oxide layer is presented as Fig. 33b. The particle on the right could be identified as o-HfO_2 in view of $[1\bar{1}0]$ zone axis. (111) plane and (002) plane could be identified, each with a d-spacing of 2.92 and 2.65 Å, respectively. The particle on the left could also be identified as o-HfO_2 as the d-spacing of the lattice fringes matches with o-HfO_2 (111). This partial oxidation was most likely caused by the impurities from the purging helium when the sample was annealed, reflecting how reactive oxygen was at this temperature. The rest part of the film continued to evolve into a nanocrystalline composite structure. Fig. 33c is a HRTEM image illustrating this microstructure. HfB_2 strips were clearly visible, while crystalline structures that match with HfN could also be observed. The SAED pattern (Fig. 33d) could be interpreted as an amorphous disk that is about to split into two diffraction rings. They correspond to HfB_2 (100) and (101), with a d-spacing of 2.69 and 2.14 Å, respectively. The crystallinity of HfN is relatively poor, as it may formed late during the microstructure evolution compared to HfB_2 which is similar to the case of the sample annealed in air. Therefore, the diffraction of HfN is missing from the SAED pattern. In summary, annealing the $Hf_7B_{23}Si_{22}C_6N_{40}$ film in an inert gas environment resulted in limited microstructure evolution, suggesting

good thermal stability of the film in such environment. In the whole annealing temperature range, the film maintained a uniform microstructure except for a thin oxide layer in the sample annealed to 1400 °C caused by impurities of the purging gas. The microstructure changed from homogeneous amorphous to a nanocrystalline composite structure as annealing temperature increased.

4.2.2 Effect of Annealing in Helium

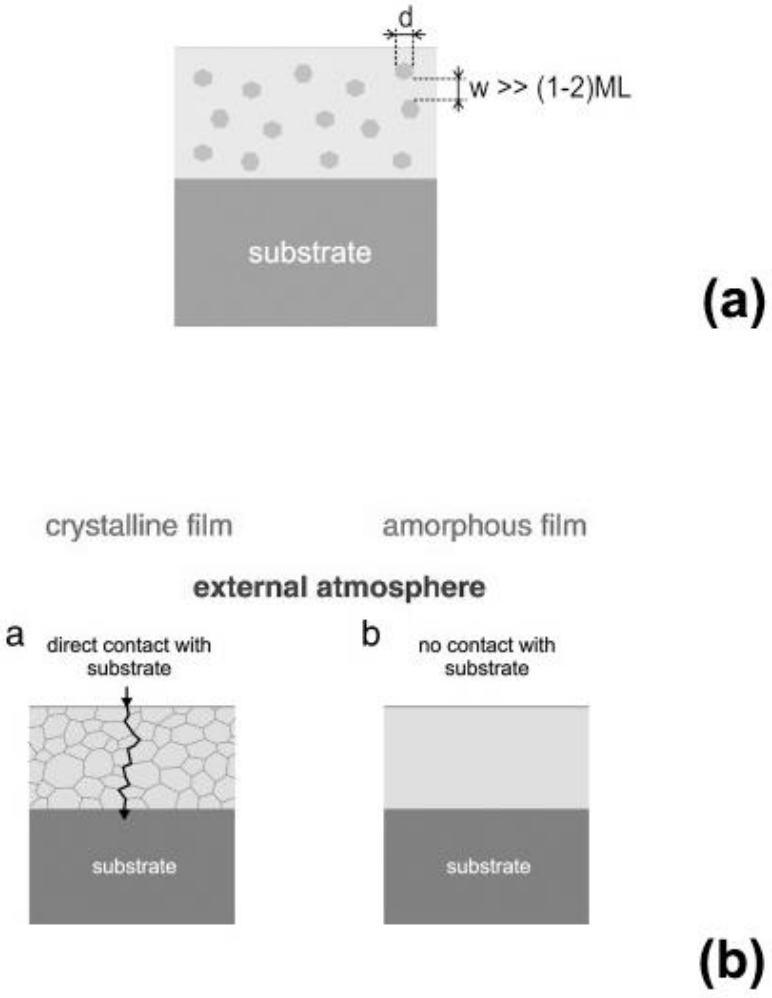

Fig. 34 (a) Schematic illustration of the microstructure of DNB/AM nanocomposites and (b) comparison of the oxidation principles in films with different microstructure [59].

The nanocrystalline composite structure formed during the annealing process could be described by a schematic illustration shown in Fig. 34a. The structure can be defined as well dispersed nanograins (DNG) separated by amorphous matrix (AM). The distance between DNGs is way larger than several monolayers (ML) to distinguish with grain boundaries in crystalline structure. DNG/AM nanocomposite structure can be formed in two ways: (1) by the dispersion of nanograins in the amorphous matrix during the deposition or (2) by the post deposition nano-crystallization of the amorphous materials that often offers unique properties such as sufficiently high hardness with enhanced toughness, low friction and high wear resistance [59, 60]. Meanwhile, DNG/AM nanocomposites maintain the superior oxidation resistance of the amorphous structures. Thin grain boundaries in conventional crystalline structures provide easy channel for oxygen diffusion and harm the protective function of the coating against oxidation, as illustrated in Fig. 34b [59]. The excellent oxidation resistance of the amorphous $Hf_7B_{23}Si_{22}C_6N_{40}$ film was already demonstrated by the analysis of microstructure evolution of the film annealed in air, and by annealing the film in helium and altering the microstructure as a post-deposition treatment, a film with both enhanced hardness and good oxidation resistance could be manufactured.

4.3 Effect of Nitrogen Content on the Microstructure and Oxidation Resistance

4.3.1 Microstructure Analysis

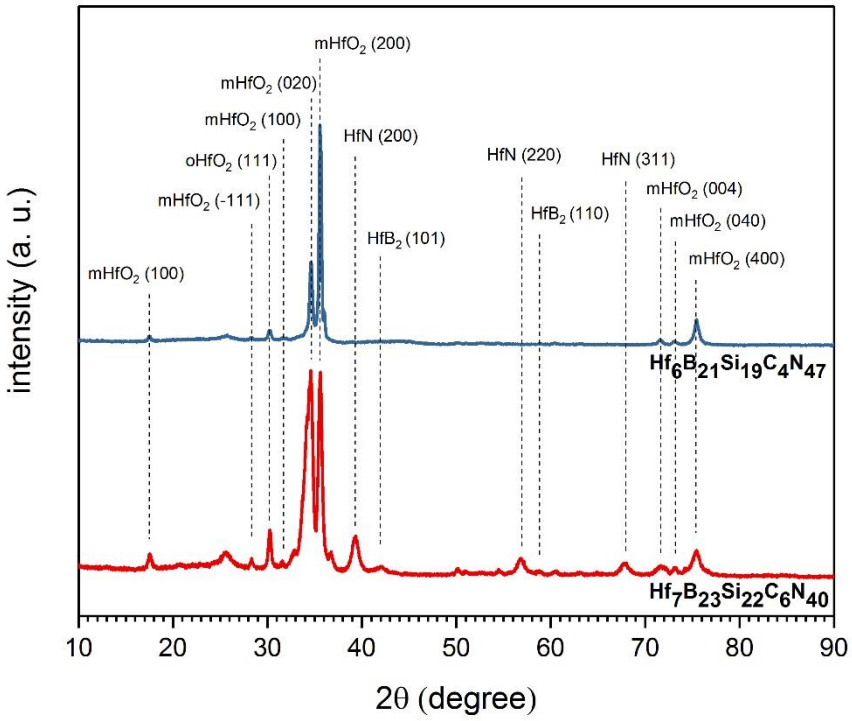

Fig. 35 XRD spectra of $Hf_7B_{23}Si_{22}C_6N_{40}$ and $Hf_6B_{21}Si_{19}C_4N_{47}$ film annealed to 1500 °C.

In this study, two samples, the $Hf_7B_{23}Si_{22}C_6N_{40}$ and $Hf_6B_{21}Si_{19}C_4N_{47}$ film annealed to 1500 °C in air, were subjected to detailed microstructure analysis. The microstructure of the former one was discussed in previous paragraphs. The latter film will be presented in this part and will be compared with the former. Composition-wise, the as-deposited $Hf_6B_{21}Si_{19}C_4N_{47}$ film contains more nitrogen than the $Hf_7B_{23}Si_{22}C_6N_{40}$ film, while all other elements are present at slightly lower level. Both annealed samples were first studied by X-ray diffraction. The XRD results of the annealed

$Hf_7B_{23}Si_{22}C_6N_{40}$ film were consistent with the TEM analysis. Diffraction peaks from monoclinic and orthorhombic HfO_2, as well as HfN and HfB_2 were identified. On the other hand, the diffraction pattern of annealed $Hf_6B_{21}Si_{19}C_4N_{47}$ film contained only peaks from HfO_2, suggesting that no HfN and HfB_2 recrystallization happened in the bottom layer.

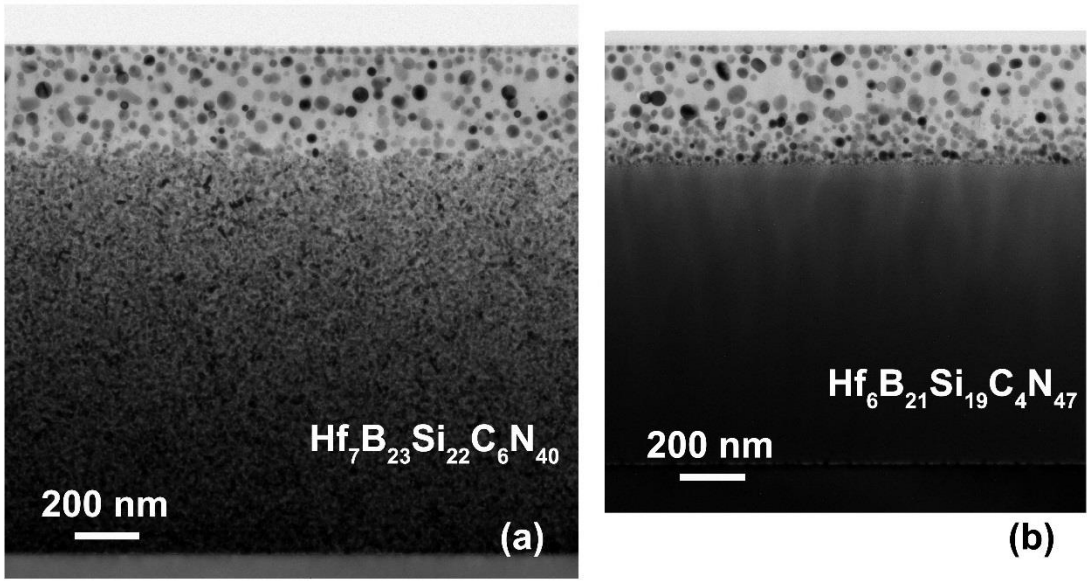

Fig. 36 Bright-field cross-section TEM image of (a) $Hf_7B_{23}Si_{22}C_6N_{40}$ and (b) $Hf_6B_{21}Si_{19}C_4N_{47}$ film annealed to 1500 °C in air.

Fig. 36 is a general microstructure comparison of two annealed samples taken from their respective cross-section TEM samples. Both films consisted of a two-layer structure with a similar top oxide layer and a completely different bottom layer. The overall thickness of annealed $Hf_6B_{21}Si_{19}C_4N_{47}$ film was about 1290 nm, which was 320 nm less than the annealed $Hf_7B_{23}Si_{22}C_6N_{40}$ film. It is due to the fact that N_2 content in the gas mixture was tuned higher during the deposition of $Hf_6B_{21}Si_{19}C_4N_{47}$ film in order to incorporate more N into the film (25% vs 15%), which reduced the deposition rate. The thickness of the oxide layer in the annealed $Hf_6B_{21}Si_{19}C_4N_{47}$ film was measured as

357 nm, which is almost identical to the annealed $Hf_7B_{23}Si_{22}C_6N_{40}$ film.

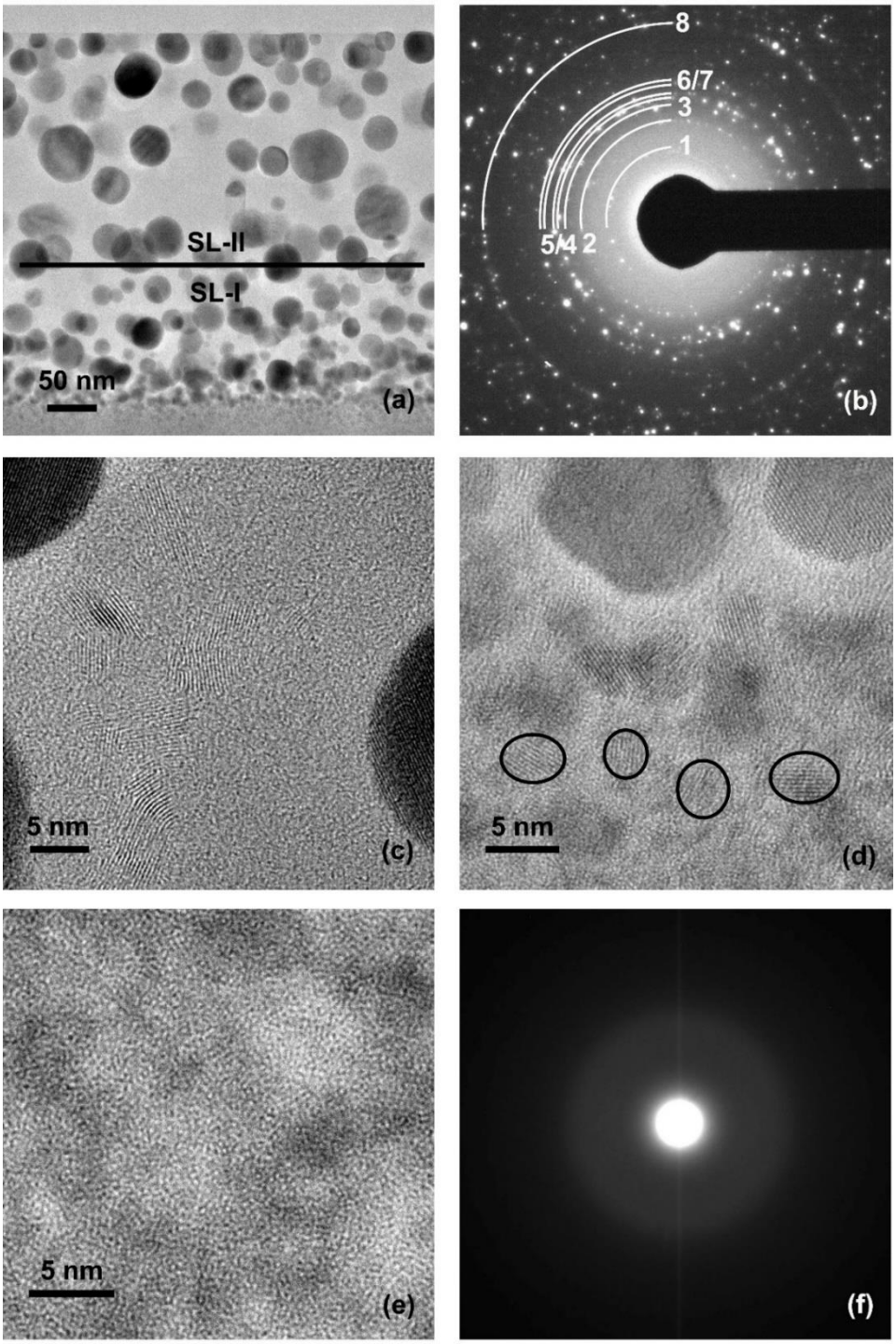

Fig. 37 (a) Bright-field TEM image of the oxide layer and (b) the corresponding SAED pattern, HRTEM image of (a) the quartz SiO_2 in the oxide layer near the interface, (d) the interface and (e) the bottom layer, and (f) the SAED pattern of the bottom layer in the $Hf_6B_{21}Si_{19}C_4N_{47}$ film annealed to 1500 °C in air.

From the previous discussion, it was concluded that the formation of a dense and continuous oxide layer is crucial to the oxidation resistance of the Hf-B-Si-C-N films. The oxide layer of the annealed $Hf_6B_{21}Si_{19}C_4N_{47}$ film was subjected to TEM investigation and a bright-field TEM image is presented in Fig. 37a. Unlike the one in annealed $Hf_7B_{23}Si_{22}C_6N_{40}$ film, the oxide layer of annealed $Hf_6B_{21}Si_{19}C_4N_{47}$ film could again be divided into two sublayers. *SL-I* and *SL-II*, which were divided by the black line in Fig. 37a, possessed similar features to their equivalent in the previous samples: In *SL-I*, dense HfO_2 particles could be found, the size of which ranged from 10 to 30 nm. In *SL-II*, dispersed particles had wide size distribution of 15 to 60 nm that indicated the ongoing coarsening process. SAED pattern of the oxide layer is presented as Fig. 37b. The analysis of the diffraction pattern was done and compared with the oxide layer in the annealed $Hf_7B_{23}Si_{22}C_6N_{40}$ film and the result is listed in Table 3, which shows that two diffraction patterns contain the same crystallographic information. Fig. 37c is a HRTEM image taken near the interface between the oxide layer and bottom layer. Quartz SiO_2 could be observed in the matrix. They had shorter length and contained a smaller number of monolayers compared to those in the annealed $Hf_7B_{23}Si_{22}C_6N_{40}$ film (Fig. 19b). The morphology of quartz SiO_2 was possibly affected not only by the annealing temperature, but also by the size of HfO_2 particles as SiO_2 formed after the formation of HfO_2, which could explain the curved nature of the crystalline structure instead of flat lattice planes. In the annealed $Hf_7B_{23}Si_{22}C_6N_{40}$ film, it was previously concluded that the microstructure changes in the bottom layer affected the oxidation kinetics, which led to HfO_2 particles with very large dimensions even at the interface.

Table 3 Index of the SAED pattern of the oxide layer in the $Hf_7B_{23}Si_{22}C_6N_{40}$ film (left column) and $Hf_6B_{21}Si_{19}C_4N_{47}$ film (middle column) annealed to 1500 °C in air.

d-spacing (Å) $Hf_7B_{23}Si_{22}C_6N_{40}$ (Fig. 18c)	d-spacing (Å) $Hf_6B_{21}Si_{19}C_4N_{47}$ (Fig. 37b)	Index
5.10	5.07	m-HfO_2 (100)
3.67	3.66	m-HfO_2 (011)
3.17	3.16	m-HfO_2 ($\bar{1}11$)
2.98	2.96	o-HfO_2 (111)
-	2.85	m-HfO_2 (111)
2.63	2.65	m-HfO_2 (002) o-HfO_2 (002)
2.54	2.55	m-HfO_2 (200)/ (020) o-HfO_2 (200)/ (020)
2.21	-	m-HfO_2 ($\bar{2}11$)/ ($\bar{1}12$)
1.83	1.82-1.85	m-HfO_2 (220)/ (022) o-HfO_2 (202)/ (022)

Thus, the length and width of quartz SiO_2 surrounding these HfO_2 particles were extended. In the annealed $Hf_6B_{21}Si_{19}C_4N_{47}$ film the situation was different. A HRTEM image of the interface is presented in Fig. 37d. Nucleation sites could be observed (marked by black circles), unlike the $Hf_7B_{23}Si_{22}C_6N_{40}$ film annealed to 1500 °C (Fig. 30b), but rather similar to the one annealed to 1400 °C (Fig. 30a). The HfO_2 underwent progressive nucleation and initial growth. Their size was considerably smaller and

more uniform, which in return led to sparse distribution of thinner and shorter crystalline SiO_2. Fig. 37e illustrates the microstructure of the bottom layer. It remained highly homogeneous amorphous without formation of nanocrystalline clusters, as verified by the SAED pattern from the bottom layer (Fig. 37f). To summarize, the slight increase of N in film composition resulted in total difference in film microstructure. The bottom layer did not transform into either nanocrystalline composite structure or crystalline structure, while two sub-layers in the oxide layer did not blend. The oxidation kinetics at the interface was different, which was primarily caused by the difference in microstructure of the bottom layer. This change in oxidation kinetics is considerably similar to the one between $Hf_7B_{23}Si_{22}C_6N_{40}$ film annealed to 1400 °C and 1500 °C in air, which was discussed in Part 4.1.

4.3.2 Effect of Nitrogen

An experimental and *ab-initio* study by Houska *et al.* on the characteristics of MSiBCN system (M=Ti, Zr, Hf) might offered some clues to explain the significant microstructure difference between the two films [61]. In that study, the composition of six films deposited using different N_2 content in the Ar+N_2 mixture was examined and the results are listed in Table 4. It shows that between 5% and 20% the nitrogen content in the film was “sub-saturated” which would significantly increase if the N_2 content in the gas mixture increased. On the other hand, between 20% and 50% the nitrogen content in the film was “saturated” which remained constant despite the N_2

content in the gas mixture increased. The two samples in comparison in our study, despite only 7% difference in N content, actually fall into different categories. Nitrogen in $Hf_7B_{23}Si_{22}C_6N_{40}$ film deposited using 15% N_2 is sub-saturated, while nitrogen in $Hf_6B_{21}Si_{19}C_4N_{47}$ film deposited using 25% N_2 is saturated. In N sub-saturated films, all bonds between different elements were possible, although the bonding statics was not random, and the formation of M-N and M-B bonds was more preferable. As more nitrogen was incorporated into the film, more N-containing bonds would form until N reached saturation when almost all other bonds were replaced by N-containing bonds.

Table 4 A list of film composition deposited using different N_2 content in the gas mixture [61].

	N_2 content in gas mixture (%)	Film composition
N sub-saturated	5	$M_{16}Si_{27}B_{36}C_9N_{12}$
	10	$M_{10}Si_{24}B_{28}C_7N_{31}$
	15	$M_8Si_{20}B_{23}C_6N_{43}$
N-saturated	20	$M_7Si_{17}B_{22}C_6N_{48}$
	30	$M_6Si_{15}B_{23}C_6N_{50}$
	50	$M_5Si_{13}B_{26}C_6N_{50}$

We believe that from the perspective of film microstructure, the role of nitrogen is amorphization of the Hf-B-Si-C-N film, which explains the amorphous nature of both as-deposited film. However, if nitrogen is sub-saturated, the amorphous structure will become metastable upon annealing possibly due to the loss of nitrogen, resulting

partial recrystallization into a nanocomposite structure and eventually into a crystalline structure due to considerable amount of pre-existed B-B, M-B and M-N bonds. However, once nitrogen is saturated, the film will remain amorphous even at high temperatures. No partial recrystallization will happen due to the excessive amount of N and the dominance of Si-N and B-N bonds. It is worth mentioning that the number of M-N bonds actually dropped in Houska *et al.*'s simulation results when nitrogen saturated which would explain that 7% more nitrogen in $Hf_6B_{21}Si_{19}C_4N_{47}$ film did not lead to the recrystallization of HfN upon annealing.

The oxidation resistance of the two films, on the other hand, is hard to conclude with the given results. In terms of oxide layer thickness and structural integrity, both films were almost identical to each other. The thermogravimetric test exhibited that both samples underwent small mass change of less than 10 μg/cm^2 at 1500 °C. $Hf_7B_{23}Si_{22}C_6N_{40}$ film experienced mass gain while $Hf_6B_{21}Si_{19}C_4N_{47}$ film experienced mass loss. More nitrogen content in $Hf_6B_{21}Si_{19}C_4N_{47}$ film led to more N_2 released from the film, which exceeded the mass gain from the oxidation of Hf and Si. From previous discussion, it is clear that compared to amorphous structure, crystalline structure in thin films are more susceptible to oxygen attacks since grain boundaries offer fast diffusion channels for oxygen. Since the bottom layer of $Hf_7B_{23}Si_{22}C_6N_{40}$ film has fully recrystallized at 1500 °C, it is possible that the oxidation resistance of this film is worse than the $Hf_6B_{21}Si_{19}C_4N_{47}$ film at higher temperatures. However, such a conclusion will not be a solid one unless a comprehensive microstructure analysis of $Hf_6B_{21}Si_{19}C_4N_{47}$ film annealed in air to 1600 °C is conducted.

Even though nitrogen saturation helps stabilize the film structure and could possibly increase oxidation resistance, blindly increasing nitrogen content in the film will not necessarily improve high temperature oxidation resistance. From Table 4 it is easy to find that the B content in N sub-saturated film decreased when N_2 content in the gas mixture increased. However, in N-saturated film, B content increased when N_2 content in the gas mixture increased. Different sputtering yield by N_2 and by Ar could contribute to this trend. Replacing metal or Si with B does not help with oxidation resistance at high temperatures because B, compared to other elements within the system, is the most susceptible to oxidation and could easily volatize at high temperatures. Therefore, it is essential to reach a balance between N and B in the film composition. In summary, the proposed film that will offer the best oxidation resistance should meet the following requirement at the same time:

1. Nitrogen just reaches the saturation state, meaning annealing will not cause recrystallization of the film.
2. Boron content within the film is kept at minimum to reduce the mass loss at high temperatures.

Given the current condition, the N_2 content in the gas mixture should be around 20% if such film is to be deposited.

4.4 Effect of Silicon vs Boron Ratio on the Microstructure and Oxidation Resistance

4.4.1 TEM Study

$Hf_7B_{10}Si_{32}C_2N_{44}$ and $Hf_6B_{10}Si_{31}C_2N_{50}$ films were deposited by a target composition of 30% B_4C + 50% Si + 20%Hf, which resulted in a higher silicon vs boron ratio of 3:1, increasing drastically from roughly 1:1 compared to previously studied $Hf_7B_{23}Si_{22}C_6N_{40}$ and $Hf_6B_{21}Si_{19}C_4N_{47}$ film. The difference between $Hf_7B_{10}Si_{32}C_2N_{44}$ and $Hf_6B_{10}Si_{31}C_2N_{50}$ film is similar to the one between $Hf_7B_{23}Si_{22}C_6N_{40}$ and $Hf_6B_{21}Si_{19}C_4N_{47}$ film, which resulted from a change in N_2 content in the gas flow during deposition. Table 5 summarizes the deposition condition and the resulted composition difference between these four films. In this part, both $Hf_7B_{10}Si_{32}C_2N_{44}$ and $Hf_6B_{10}Si_{31}C_2N_{50}$ films were subjected to comprehensive and detailed TEM microstructure analysis.

Table 5 A summary of deposition condition and composition difference between four Hf-B-Si-C-N films.

Film composition	Target			N_2
	B_4C	Si	Hf	
$Hf_7B_{10}Si_{32}C_2N_{44}$	65%	20%	15%	25%
$Hf_6B_{10}Si_{31}C_2N_{50}$	65%	20%	15%	50%
$Hf_7B_{23}Si_{22}C_6N_{40}$	30%	50%	20%	15%
$Hf_6B_{21}Si_{19}C_6N_{47}$	30%	50%	20%	25%

4.4.1.1 Overall microstructure

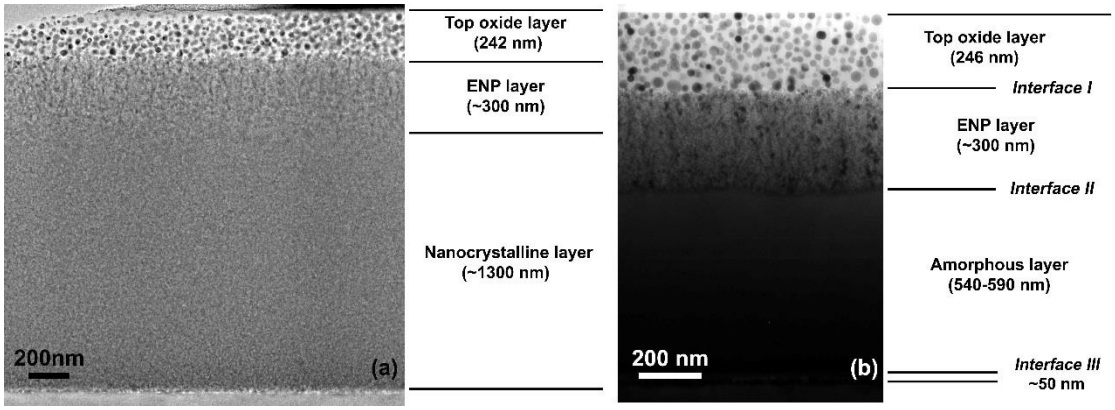

Fig. 38 Cross-section BF images of (a) $Hf_7B_{10}Si_{32}C_2N_{44}$ and (b) $Hf_6B_{10}Si_{31}C_2N_{50}$ film.

The cross-section bright-field images of $Hf_7B_{10}Si_{32}C_2N_{44}$ and $Hf_6B_{10}Si_{31}C_2N_{50}$ films are presented in Fig. 38. The images showed that both films could be roughly divided into 3 layers, which was different from previous $Hf_7B_{23}Si_{22}C_6N_{40}$ and $Hf_6B_{21}Si_{19}C_4N_{47}$ films. A top oxide layer consisting of spherical nanoparticles embedded in a bright amorphous matrix existed in both films, followed by an unprecedented elongated nanoparticle (ENP) layer underneath. The overall morphology, including thickness, of these two layers was similar in both films. The difference in the third layer can be compared to the difference between $Hf_7B_{23}Si_{22}C_6N_{40}$ and $Hf_6B_{21}Si_{19}C_4N_{47}$ film, where "nitrogen-subsaturation" led to recrystallization of the bottom layer into polycrystalline structure, and "nitrogen-saturation" helped maintain the homogeneous amorphous structure and demonstrated high thermal stability. Similarly, the third layer, i.e., bottom layer in $Hf_7B_{10}Si_{32}C_2N_{44}$ film has fully recrystallized while the one in $Hf_6B_{10}Si_{31}C_2N_{50}$ film was still amorphous. Apart from that, the thickeness of the bottom layer in these two films was significantly different. The nanocrystalline layer in $Hf_7B_{10}Si_{32}C_2N_{44}$ film was over 1300 nm, while the amorphous layer in

$Hf_6B_{10}Si_{31}C_2N_{50}$ film was less than 600 nm. In addition, the interface between the nano-column layer and the bottom layer, which was marked as *Interface II* in Fig. 38b, is clearly observable in $Hf_6B_{10}Si_{31}C_2N_{50}$ film, while in $Hf_7B_{10}Si_{32}C_2N_{44}$ film it is much harder to identify such interface. A detailed TEM analysis focusing on that particular part of the film will be given in the following paragraphs. What's more, *Interface III* in Fig. 38b, which is between the bottom layer and substrate, could be considered as a thin "sublayer". The thickness of this sublayer was about 50 nm. Such a sublayer was not identified in $Hf_7B_{10}Si_{32}C_2N_{44}$ film at the beginning by low-mag images. However, HRTEM images taken from that area proved that *Interface III* existed in $Hf_7B_{10}Si_{32}C_2N_{44}$ film having similar thickness, with unique microstructure features, which blended into the nanocrystalline bottom layer eventually.

4.4.1.2 Top Oxide Layer

The top oxide layers in both $Hf_7B_{10}Si_{32}C_2N_{44}$ and $Hf_6B_{10}Si_{31}C_2N_{50}$ films had very similar thickness, as shown in Fig. 38. TEM images taken under higher magnification, along with the corresponding electron diffraction patterns, are illustrated in Fig. 39. The thickness of this layer was less than 250 nm in both films, which was less than the oxide layer in $Hf_7B_{23}Si_{22}C_6N_{40}$ and $Hf_6B_{21}Si_{19}C_4N_{47}$ films with lower silicon vs boron ratio. The spherical particle size had very homogeneous distribution across the whole oxide layer, as shown in Fig. 39a and 39c. No sublayers within the top oxide layer could be identified. The average size of these particles ranged from 10 to 30 nm. The electron diffraction patterns from the oxide layers in both films contain diffraction from monoclinic and orthorhombic/tetragonal HfO_2. Like the previous cases, it is difficult to

tell the difference between orthorhombic and tetragonal HfO_2 solely from diffraction patterns as these two structures are very similar. However, the annealing temperature of these two sample was 1500 °C which is similar to the samples studied before, making formation of orthorhombic HfO_2 more probable than tetragonal HfO_2. Table 6 is a summary of analysis results from the two diffraction patterns in Fig. 39b and 39d.

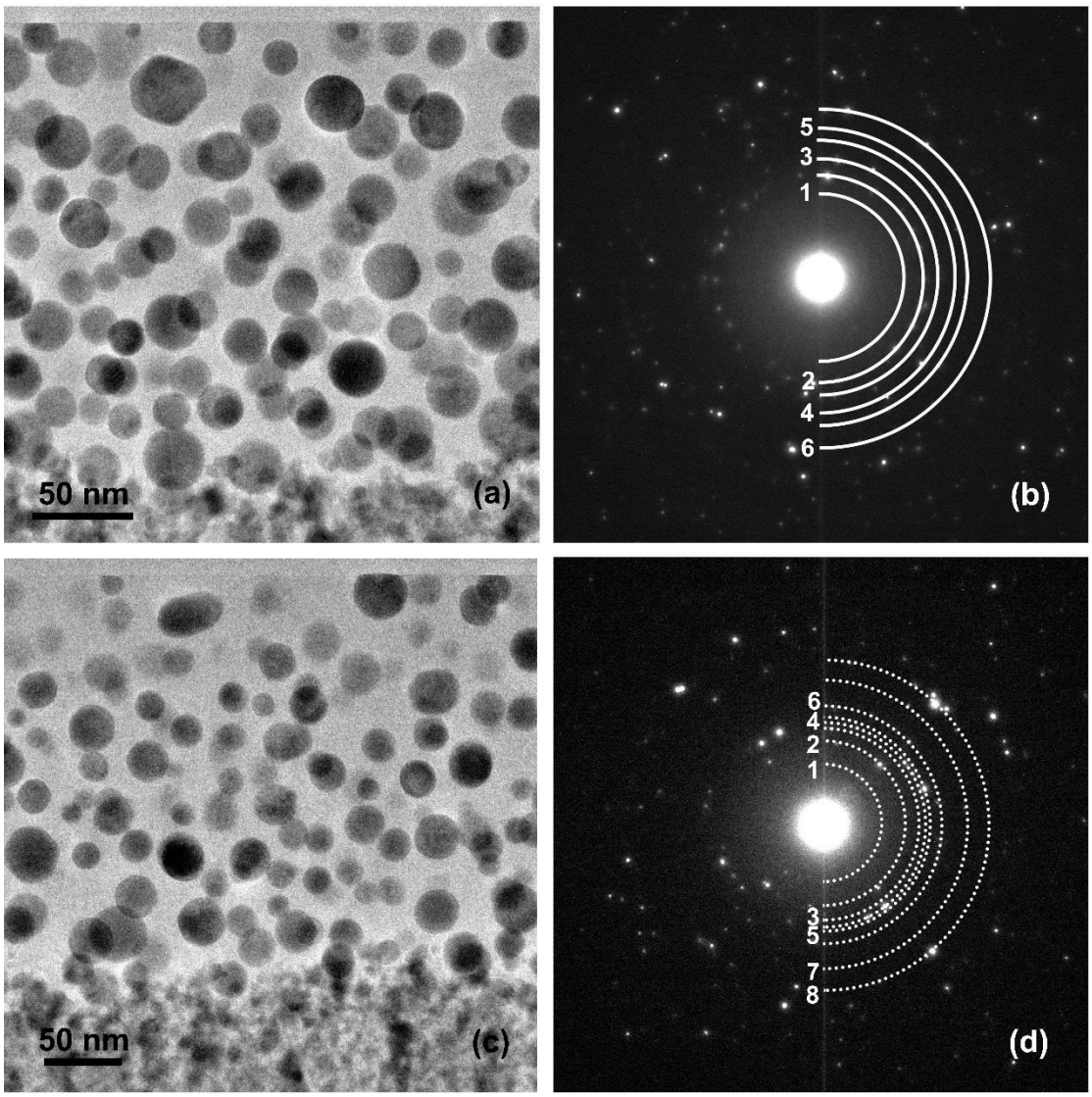

Fig. 39 TEM images and corresponding SAED patterns of (a) & (b) $Hf_7B_{10}Si_{32}C_2N_{44}$ and (c) & (d) $Hf_6B_{10}Si_{31}C_2N_{50}$ film.

Table 6 A summary of analysis results from the SAED patterns of the oxide layer in $Hf_7B_{10}Si_{32}C_2N_{44}$ and $Hf_6B_{10}Si_{31}C_2N_{50}$ film.

$Hf_7B_{10}Si_{32}C_2N_{44}$			$Hf_6B_{10}Si_{31}C_2N_{50}$		
Ring No.	Measured d-spacing (Å)	Index	Ring No.	Measured d-spacing (Å)	Index
1	3.70	m-(011)	1	5.05	m-(100)
2	2.99	o-(111)	2	3.67	m-(011)
3	2.57-2.65	m-(200)/(020)/(002) o-(200)/(020)/(002)	3	3.13	m-($\bar{1}$11)
4	2.37	m-(120)/(021)/(012) o-(102)	4	2.97	o-(111)
5	2.09	m-(121) o-(121)	5	2.82	m-(111)
6	1.81-1.83	m-(220)/(022) o-(220)/(202)/(022)	6	2.58	m-(020)/(002) o-(020)
			7	2.13	m-($\bar{1}$21)
			8	1.78-1.83	m-($\bar{2}$21)/($\bar{1}$22)/ (220)/(022) o-(220)/(202)/(022)

HRTEM images were taken to study the HfO_2 particles, examples of which are illustrated as Fig. 40. Like in previous samples, monoclinic HfO_2 particles could be captured by HRTEM which are shown in Fig. 40a. In the corresponding FFT pattern (Fig. 40b), B1 and B2 are diffraction spots of m-HfO_2 (110) and (002), with the d-spacing of 3.63 and 2.64 Å, respectively, while B3 corresponds to the diffraction of m-HfO_2 (111), with a lattice spacing of 2.83 Å. B4 is likely to be the diffraction spot of m-HfO_2 (11$\bar{1}$) and has a d-spacing of 3.16 Å that is unique in monoclinic HfO_2 since this lattice parameter does not appear in other HfO_2 crystalline structures. Figs. 40c and 40e are two HRTEM images taken on orthorhombic HfO_2 particles, and Figs. 40d and 40f are

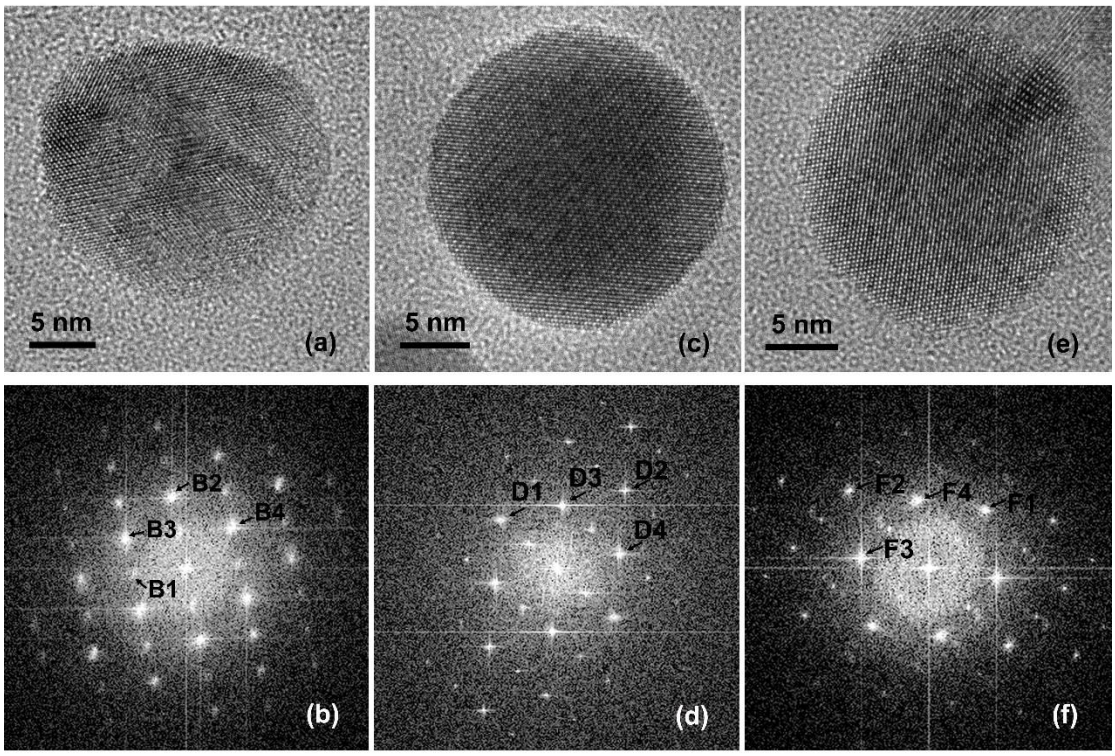

Fig. 40 HRTEM images of m-HfO_2 and o-HfO_2 in the top oxide layer in $Hf_7B_{10}Si_{32}C_2N_{44}$ and $Hf_6B_{10}Si_{31}C_2N_{50}$ film.

the corresponding FFT patterns. Fig. 40c was captured with $[01\bar{1}]$ or $[10\bar{1}]$ zone axis parallel to the beam. D1 in Fig. 40d could be identified as o-HfO_2 (200) or (020) and D2 could be identified as o-HfO_2 (022) or (202), depending on the index of D1. Tiny difference between *a* and *b* axis of the o-HfO_2 unit cell made it difficult to index accurately these two diffraction spots. However, D3 and D4 could be identified as o-HfO_2 {111} with ease as they possess a unique d-spacing of about 2.96 Å. Similarly, another o-HfO_2 particle was identified and presented in Fig. 40e with its corresponding FFT pattern shown in Fig. 40f. F1 in Fig. 40f could be identified as o-HfO_2 (200) with a d-spacing of 2.49 Å. This parameter is close to the shorter *a* axis of the o-HfO_2 unit cell instead of *b* axis. Accordingly, F2 corresponds to (022) plane of o-HfO_2. Both F3 and F4

match well with o-HfO_2 (111). The formation of both m-HfO_2 and o-HfO_2 was consistent with previously analyzed $Hf_7B_{23}Si_{22}C_6N_{40}$ films. No direct and solid proof of tetragonal HfO_2 in the oxide layer could be drawn from the TEM results. The matrix surrounding HfO_2 particles is amorphous in all HRTEM images and is likely SiO_x based similarly to our previous findings.

4.4.1.3 ENP layer

The formation of ENP layer was observed directly underneath the top oxide layer in both $Hf_7B_{10}Si_{32}C_2N_{44}$ and $Hf_6B_{10}Si_{31}C_2N_{50}$ films. The characteristic feature of this layer is, as the name indicated, scattering elongated nanoparticles (darker contrast) separated by the matrix (brighter contrast). Elongation of these particles was not randomly oriented, instead, they are mostly oriented perpendicularly to the film substrate, as shown in Figs. 41a and 41c, which likely indicated anisotropic growth of these particles. Initial investigation of this layer using electron analysis revealed that lattice parameters closely matching orthorhombic/tetragonal HfO_2 and Si_3N_4 crystalline structure could be found in this layer, which are shown as Figs. 41b and 41d, respectively. For example, Ring 1 in Fig. 41b corresponds to a lattice parameter of 6.73 Å, which uniquely matches with Si_3N_4 (100). In addition, ring 2, 3 and 4 correspond to the d-spacing of 4.39, 3.91 and 3.39 Å, respectively, which could be identified as Si_3N_4 (101), (110) and (200), respectively. Similarly, ring 1, 2 and 3 in Fig. 41d correspond to the d-spacing of 6.69, 3.88 and 3.35 Å and could be identified as Si_3N_4 (100), (110) and (200). Thus, formation of Si_3N_4 was confirmed in both films. Diffraction from ot-HfO_2 (111) which possesses a unique d-spacing of 2.95 Å was captured in SAED patterns

from both films and all the other diffraction spots also matched closely with the lattice parameters of either Si_3N_4 or ot-HfO_2. No sign of m-HfO_2 was observed. Tables 7 and 8 summarize the analysis results of two SAED patterns in Figs. 41b and 41d.

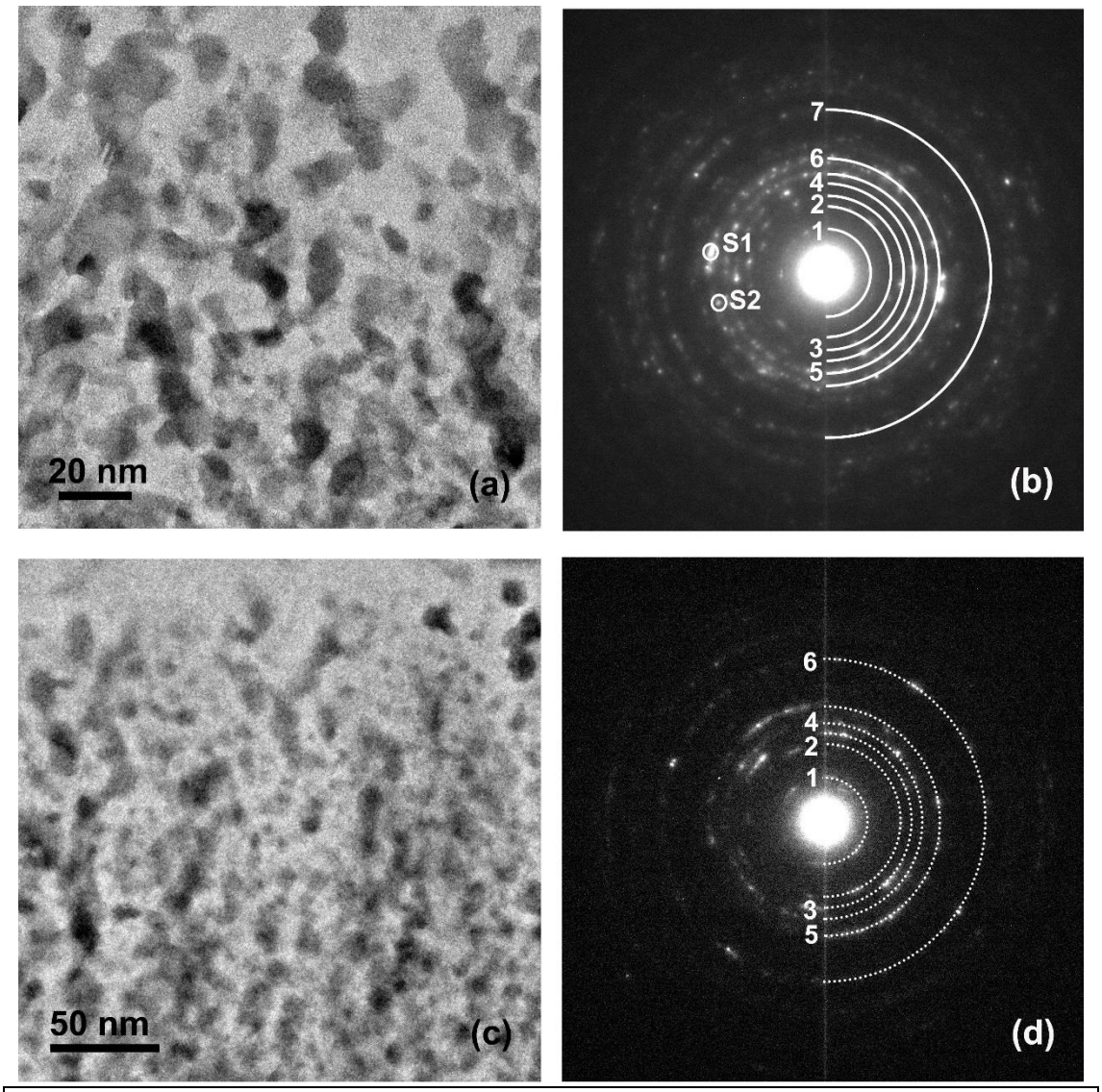

Fig. 41 TEM image and the corresponding SAED pattern of the ENP layer of (a) & (b) $Hf_7B_{10}Si_{32}C_2N_{44}$ film and (c) & (d) $Hf_6B_{10}Si_{31}C_2N_{50}$ film.

The formation of HfO_2 in ENP layer was proved by electron diffraction pattern analysis, which indicated that oxygen diffused beyond the interface between the top oxide layer and the rest of the film. In previously studied $Hf_7B_{23}Si_{22}C_6N_{40}$ and $Hf_6B_{21}Si_{19}C_4N_{47}$ films, the bottom part, whether being amorphous or crystalline, did

Table 7 A summary of analysis results from the SAED patterns of the ENP layer in $Hf_7B_{10}Si_{32}C_2N_{44}$ film.

Ring No.	Measured d-spacing (Å)	Index
1	6.69	Si_3N_4 (100)
2	3.88	Si_3N_4 (110)
3	3.35	Si_3N_4 (200)
4	2.93	ot-HfO_2 (111)
5	2.54	ot-HfO_2 (020) Si_3N_4 (210)
6	1.82	ot-HfO_2 (202)/(022) Si_3N_4 (103)

Table 8 A summary of analysis results from the SAED patterns of the ENP layer in $Hf_6B_{10}Si_{31}C_2N_{50}$ film.

Ring No.	Measured d-spacing (Å)	Index
1	6.73	Si_3N_4 (100)
2	4.39	Si_3N_4 (101)
3	3.91	Si_3N_4 (110)
4	3.39	Si_3N_4 (200)
5	2.99	o-HfO_2 (111)
6	2.54-2.7 *S1*: 2.57, *S2*: 2.65	ot-HfO_2 (200)/(020)/(002) Si_3N_4 (210)/(102)
7	1.84	ot-HfO_2 (022)/(202) Si_3N_4 (103)/(310)

not show existence of oxides which means all oxidation process happened at the interface between the top oxide layer and the bottom layer. However, in both $Hf_7B_{10}Si_{32}C_2N_{44}$ and $Hf_6B_{10}Si_{31}C_2N_{50}$ films, permeated oxygen had reached beyond this interface and oxidized Hf in the deeper part of the film. The ENP layer should be considered as a partially oxidized layer, as no sign of silicon, which was one of the major elements of the original film, being oxidized could be found. Instead, formation of crystalline Si_3N_4 was observed. HRTEM images further illustrating the two crystalline structures were taken and an example of which is shown as Fig. 42a. The grain on the

left with brighter contrast could be identified as Si_3N_4, with the clear fringes of its (101) plane being marked. The grain on the right with darker contrast could be identified as ot-HfO_2 in view of $[1\bar{1}0]$ zone axis. The FFT patterns of both crystalline structures are shown as Figs. 42b and 42c. Careful observation through the ENP layer did not verify formation of other crystalline structure, such as HfN or BN. It was also safe to say that no m-HfO_2 formed in this layer. However, despite our best effort, HRTEM imaging was unable to illustrate the lattice parameters that match exclusively with orthorhombic HfO_2 or tetragonal HfO_2, unlike in previous samples. In addition to that, phase transformation of HfO_2 between orthorhombic, tetragonal and monoclinic HfO_2 is complicated, and much about it is still unknown. Despite the fact at ambient pressure, the transition between monoclinic and tetragonal HfO_2 happened at temperatures higher than the annealing temperature of the current two samples, while the transition between orthorhombic and tetragonal HfO_2 could happen at much lower temperatures given the proper pressure. For example, Ohtaka *et al.* reported that this transition could happen at around 1400 °C [62]. Considering it was difficult to measure the exact pressure when oxidation happened in our sample, it was unclear that if the formation of t-HfO_2 is possible in ENP layer. Formation of tetragonal HfO_2 typically requires higher energy compared to orthorhombic one, which could be provided by extra pressure coming from the rigid Si_3N_4 matrix. A detailed explanation regarding the formation of Si_3N_4 in the ENP layer and its eventual oxidation, the formation and phase transformation of HfO_2, and how they are related to the higher silicon vs boron ratio of the film, would be given at the end of the discussion.

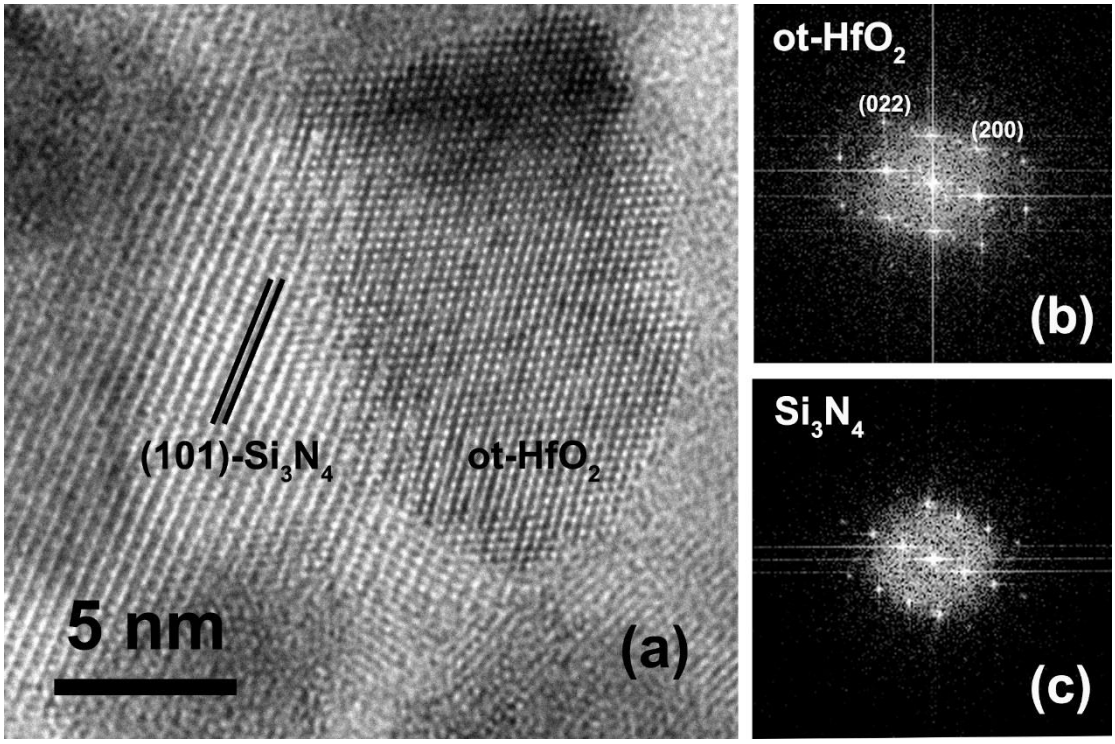

Fig. 42 (a) A HRTEM image of the crystalline structure of an ot-HfO_2 grain and the surrounding Si_3N_4 matrix, (b) & (c) and the corresponding FFT pattern.

4.4.1.4 Nanocrystalline layer in $Hf_7B_{10}Si_{32}C_2N_{44}$ film and amorphous layer in $Hf_6B_{10}Si_{31}C_2N_{50}$ film

The microstructure of the "bottom layer" in $Hf_7B_{10}Si_{32}C_2N_{44}$ and $Hf_6B_{10}Si_{31}C_2N_{50}$ films had major difference that closely resembled the difference between $Hf_7B_{23}Si_{22}C_6N_{40}$ and $Hf_6B_{21}Si_{19}C_4N_{47}$ films as illustrated clearly in Fig. 38. The film with higher nitrogen content had better thermal stability and as a result, the "bottom layer" in $Hf_6B_{10}Si_{31}C_2N_{50}$ film remained amorphous, while in $Hf_7B_{10}Si_{32}C_2N_{44}$ film it recrystallized into a nanocrystalline layer. However, TEM survey of this nanocrystalline layer revealed that formation of HfO_2 in this layer was extensive at its upper part. The finding of HfO_2 was unpreceded as in previously studied $Hf_7B_{23}Si_{22}C_6N_{40}$ film, the nanocrystalline bottom layer contained only nitrides and borides, i.e., HfN, HfB_2, Si_3N_4

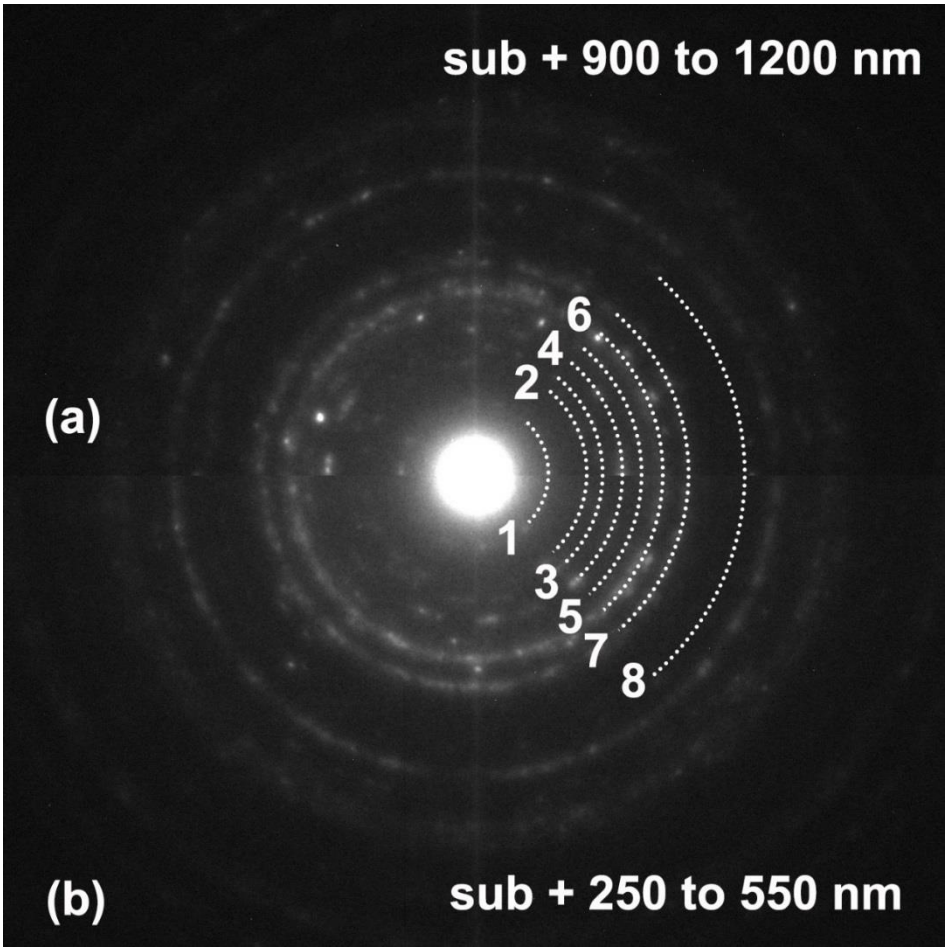

Fig. 43 The comparison of electron diffraction patterns taken from (a) the area 900 to 1200 nm above the substrate and (b) the area 250 to 550 nm above the substrate in $Hf_7B_{10}Si_{32}C_2N_{44}$ film, each occupying half of the image.

and BN instead of oxides, which means it was free of oxygen. In $Hf_7B_{10}Si_{32}C_2N_{44}$ film, only the bottom part of this layer which had a thickness of about 600 nm could be considered as oxide-free. HfN, together with Si_3N_4, was observed in this area. Above that, intensity of HfO_2 gradually increased until it reached the interface between the nanocrystalline layer and ENP layer. Fig. 43 is the SAED patterns taken from different "depth" of the nanocrystalline layer illustrating this oxidation process of Hf. The seemingly one complete diffraction pattern actually consists of two diffraction patterns, each occupying half of the image, taken from different area of the film. The upper part of the image was taken from an area about 900 to 1200 nm above the

substrate, close to the interface between the nanocrystalline layer and ENP layer. The lower part was taken from an area about 250 to 550 nm above the substrate, where it was believed to be oxide-free. Ring 1 to ring 4 appear in both diffraction patterns, they all correspond to different lattice parameters of Si_3N_4. For example, ring 1 corresponds to a d-spacing of 6.69 Å, a value close to Si_3N_4 (100). Ring 2 corresponds to a d-spacing of 4.33 Å, which could be identified as Si_3N_4 (101). Ring 3 and ring 4 could be identified as Si_3N_4 (110) and (200), respectively, corresponding to lattice spacing of 3.86 and 3.33 Å. Ring 5 shows a small visible mismatch in two diffraction patterns, suggesting that they represent different lattice parameters in different depth of the layer. Ring 5 in Fig. 43a is a bit smaller, corresponding to a d-spacing of 2.92 Å, a critical value that was previously determined closely corresponding to ot-HfO_2 (111). Ring 5 in Fig. 43b is a bit larger and much weaker, which corresponds to a smaller lattice parameter of about 2.89 Å. Despite such a small difference could be the result of measurement error, it's still possible that ring 5 represents a set of different lattice planes, presumably Si_3N_4 (201), in Fig. 43b. Ring 6 appears clearly in both patterns and they look much similar. This ring likely corresponds to superimposed diffraction of Si_3N_4 (102)/(210) and HfN (111), with lattice parameters ranging from 2.53 to 2.64 Å. Ring 7 could be identified uniquely as HfN (200) which has a d-spacing of 2.29 Å and it appears in both patterns as well. Ring 8 appears vaguely in both Figs.43a and 43b. It was identified as ot-HfO_2 (022)/(202) or Si_3N_4 (103). Despite diffraction rings overlapping, oxygen diffusion into the nanocrystalline layer, leading to formation of ot-HfO_2 in the upper part could be partially proved. Extensive HRTEM investigation of the nanocrystalline layer further

verified the existence of ot-HfO_2. As stated before, this thorough investigation found out that the lower part of the layer, starting from substrate to sub + 600 nm, had no oxide formation. Starting from sub + 600 nm, sparse HfO_2 could be observed along with HfN, which was still the majority of Hf-containing phase. It should be considered as the initial point of oxidation. However, there was no clear interface between the oxide-free part and the partially oxidized part of the layer. As TEM investigation gradually progressed away from the initial point of oxidation towards the interface

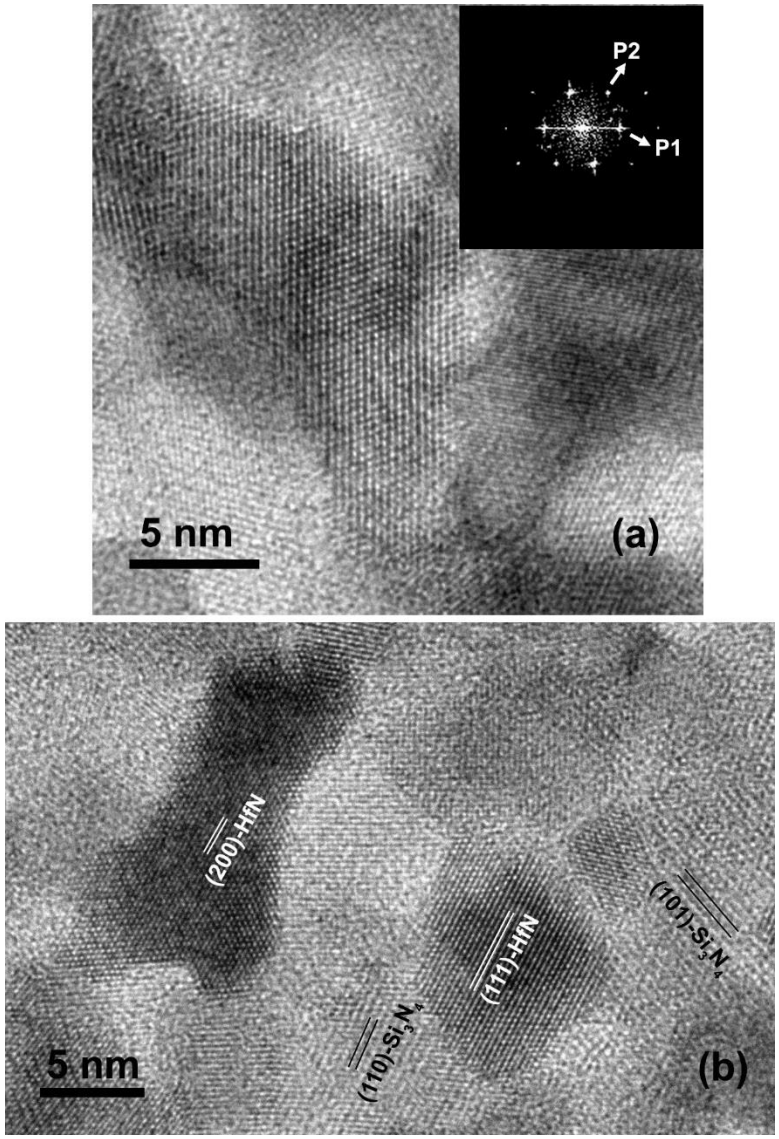

Fig. 44 HRTEM images taken from different area of the nanocrystalline layer in $Hf_7B_{10}Si_{32}C_2N_{44}$ film illustrating (a) ot-HfO_2, (b) HfN and Si_3N_4.

between the nanocrystalline layer and ENP layer, the intensity of ot-HfO_2 gradually increased while the intensity of HfN gradually reduced. However, it did not inflict changes to overall morphology and the nanocrystalline layer remained homogeneous across the thickness, as shown in Fig. 38. Differentiating between HfO_2 and HfN grains can only be reliably achieved by detailed HRTEM analysis of the crystalline structure.

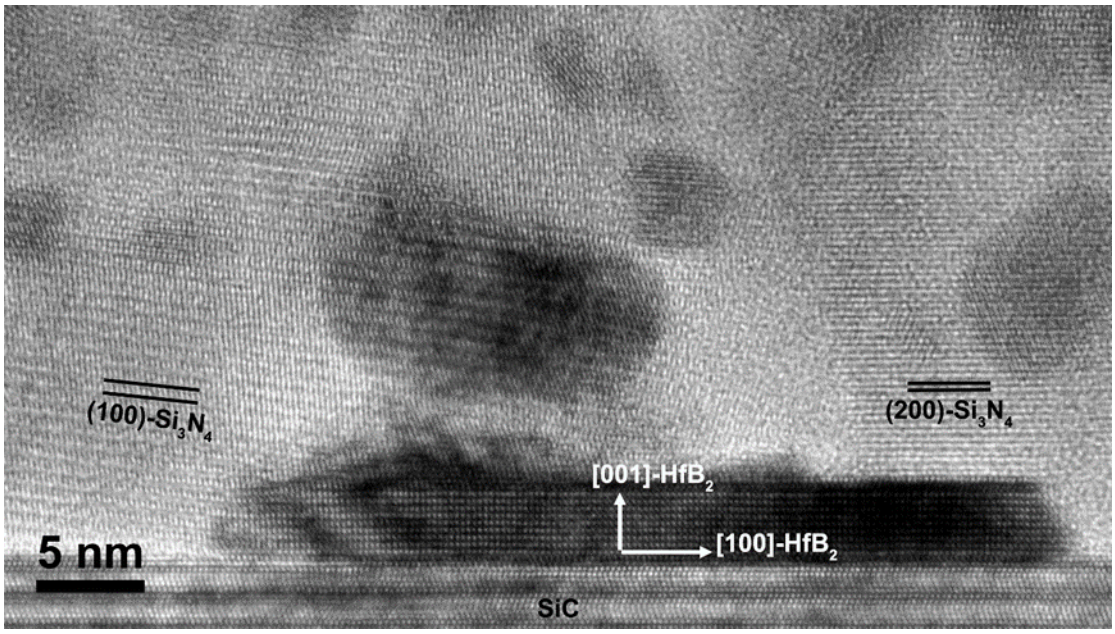

Fig.45 A HRTEM image taken from the interface between the substrate and $Hf_7B_{10}Si_{32}C_2N_{44}$ film illustrating HfB_2 and textured Si_3N_4 texture in this area.

Fig. 44a is a HRTEM image taken from the partially oxidized part of the nanocrystalline layer, illustrating the ot-HfO_2 crystalline structure. In the corresponding FFT pattern, both P1 and P2 correspond to lattice parameters that match with ot-HfO_2 only, which are ot-HfO_2 (111) of 2.95 Å and ot-HfO_2 (200)/(020) of 2.53 Å. In another HRTEM image taken at oxide-free part of the layer, lattice fringes of HfN (111) and (200) were identified, as shown in Fig. 44b. The matrix surrounding Hf-containing phases were h-Si_3N_4 across the whole nanocrystalline layer. Except for the very bottom part of this layer, no carbon or boron containing crystalline structure was observed. Carbon can

easily form solid solution within HfN, substituting N atoms without altering the fcc crystalline structure, forming Hf(C)N [63, 64], while boron, which is considerably small, could get into interstitials of other crystalline structures or grain boundaries. Fig. 45 illustrates the crystalline structures at the interface between the film and the substrate, which were different compared to the rest of the nanocrystalline layer. A HfB_2 strip, which was elongated along [100] direction similarly to those in $Hf_7B_{23}Si_{22}C_6N_{40}$ film could be identified. HfB_2 appeared exclusively at the interface, and the surrounding Si_3N_4 exhibited obvious texture unlike randomly oriented Si_3N_4 grains in the other part of the film. Textured Si_3N_4 was more noticeable in $Hf_6B_{10}Si_{31}C_2N_{50}$ film. As stated before, the bottom part of $Hf_6B_{10}Si_{31}C_2N_{50}$ film remained homogeneous amorphous, as shown in Figs. 46a and 46b, except for the interface between the film and the substrate, i.e., *Interface III*, where a thin crystalline sublayer formed. Crystalline HfB_2, HfN and Si_3N_4 could be found within this sublayer. Strong texture of Si_3N_4 was exhibited by diffraction pattern of Si_3N_4 taken at different locations of *Interface III*, as illustrated by Figs. 46d and 46e. Difference between the two electron diffraction patterns showed that despite having texture, Si_3N_4 grains was not oriented to the same direction. In Fig. 46d, the Si_3N_4 had $[1\bar{1}\bar{1}]$ zone axis oriented parallel to the beam, and (110), $(01\bar{1})$ and (101) planes were identified and marked by white arrow. While in Fig. 46e, [010] zone axis was identified being parallel to the beam, and diffraction spots of $(\bar{1}01)$, (201) and (102) planes were observable. In both $Hf_7B_{10}Si_{32}C_2N_{44}$ and $Hf_6B_{10}Si_{31}C_2N_{50}$ films the most frequently observed Si_3N_4 textures were (100) or (001) with respect to SiC-(001). However, they were usually several degrees off thus did not follow exact epitaxial

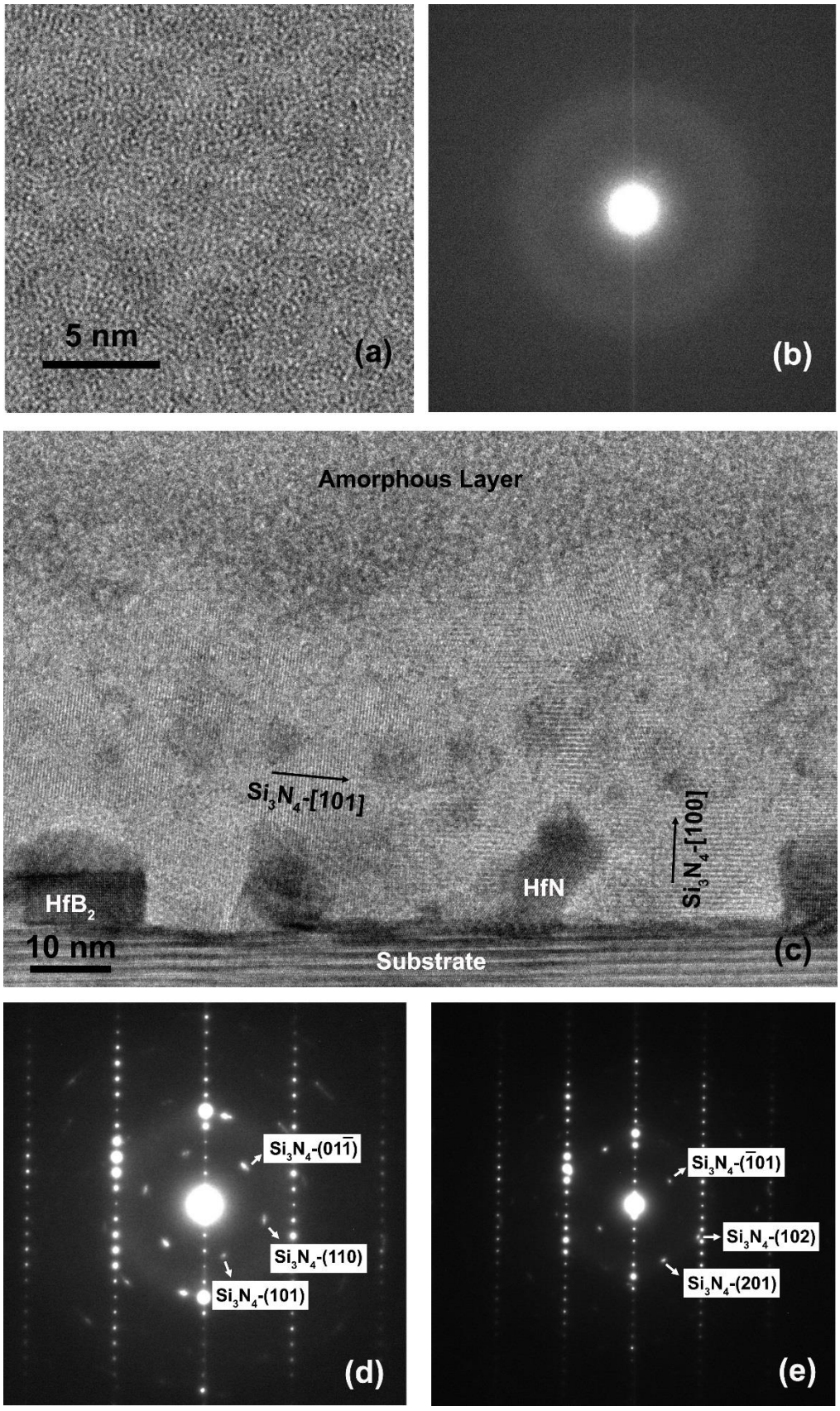

Fig. 46 TEM images and the corresponding SAED patterns of (a) & (b) the amorphous layer in $Hf_6B_{10}Si_{31}C_2N_{50}$ film and (c), (d) and (e) interface between the film and SiC substrate illustrating HfB_2, HfN and textured Si_3N_4 crystalline structures.

growth direction. Nevertheless, the crystal orientation of SiC would still be the most probable reason for the formation of Si_3N_4 texture. No oxide-containing phase was found in this area. The crystallization of this small sublayer is then likely not to be triggered by the oxidation process. One possible explanation is more efficient heat transfer along the interface than the thickness of the substrate or the film itself. The binding between the film and the substrate could evolve at high temperatures, which would change the local atomic binding static, resulting crystallization and formation of the crystalline sublayer. Fig. 47 is a HRTEM image illustrating the microstructure of this thin sublayer in $Hf_6B_{10}Si_{31}C_2N_{50}$ film. Combined HfN-HfB_2 could be observed atomically attached to the substrate. Also, the SiC substrate was not atomically flat and small dimples (circled in black) and bumps could be observed at the interface, which suggested strong binding interactions between the film and the substrate at high temperatures that would change the chemistry of this sublayer and resulted the crystallization in the end.

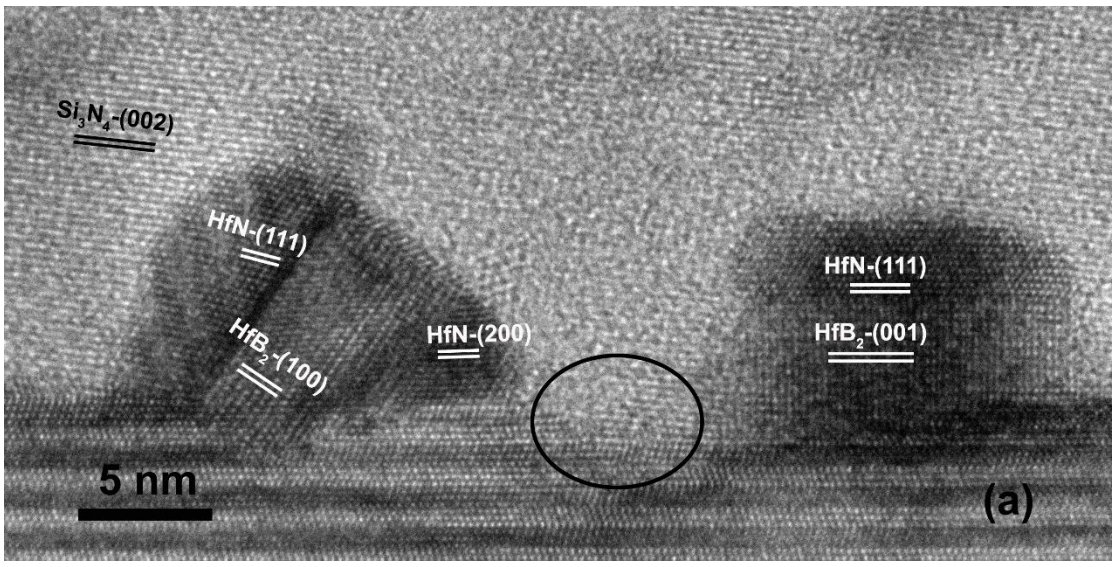

Fig. 47 A HRTEM image of the interface between the film and SiC substrate in $Hf_6B_{10}Si_{31}C_2N_{50}$ film.

4.4.2 Effect of Silicon vs Boron Ratio

In summary, the study subjects of this part, i.e. $Hf_7B_{10}Si_{32}C_2N_{44}$ film and $Hf_6B_{10}Si_{31}C_2N_{50}$ film have four major differences in the microstructure compared to $Hf_7B_{23}Si_{22}C_6N_{40}$ and $Hf_6B_{21}Si_{19}C_4N_{47}$ film:

- The thickness of the top oxide layer was reduced.
- A partially oxidized ENP layer formed underneath the top oxide layer.
- A thin crystalline sublayer formed at the interface between the film and the substrate.
- The nanocrystalline layer was partially oxidized in $Hf_7B_{10}Si_{32}C_2N_{44}$ film.

It was likely that higher silicon vs boron ratio played a major role in these changes, which would be explained in detail in the following paragraphs.

4.4.2.1 Formation of the ENP layer

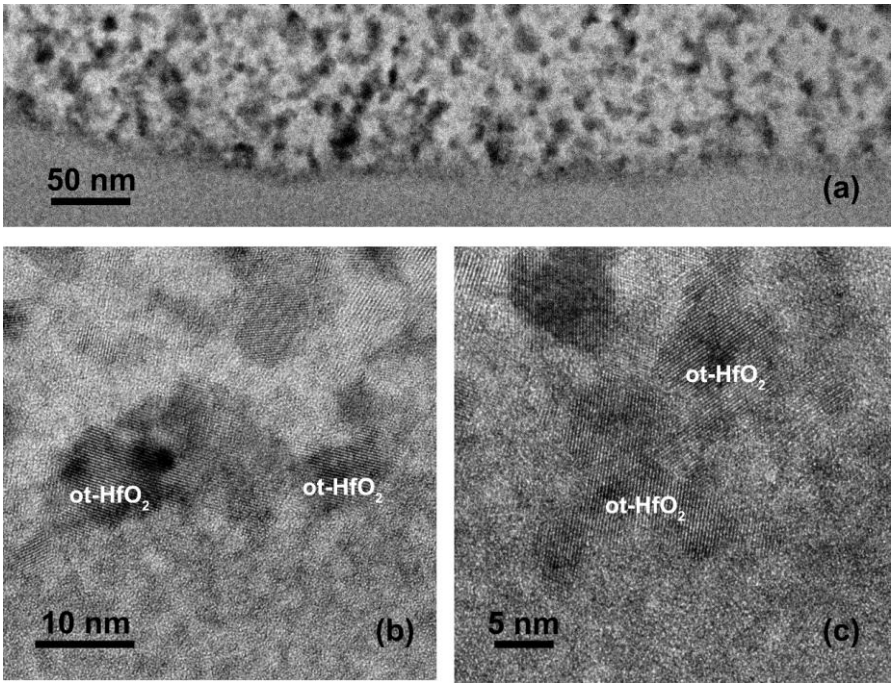

Fig. 48 TEM images of *Interface II* in $Hf_6B_{10}Si_{31}C_2N_{50}$ film, no nucleation site could be found.

The formation of the ENP layer was the most prominent microstructure difference among the four major differences mentioned above. To start with, TEM images of the interface between the ENP layer and the amorphous layer, i.e., *Interface II* in $Hf_6B_{10}Si_{31}C_2N_{50}$ film are presented in Fig. 48. There is no reason to believe that oxidation happened beyond this interface in the amorphous layer, thus, it was the initial point of oxidation in this film. The situation in $Hf_7B_{10}Si_{32}C_2N_{44}$ film was different and will be discussed later.

There was no visible nucleation site at *Interface II* as illustrated by HRTEM images (Fig. 48b and 48c). Instead, the "width" of the ot-HfO_2 grains was typically around 10 nm. It appeared that despite as the initial point of oxidation, ot-HfO_2 which was part of the reaction products assembled in coalescence to the existing grains, meaning the growth direction was downward (towards the substrate) instead of upward (towards the surface). Similarly, no Si_3N_4 nucleation site was observed at *Interface II* either. Thus, it is reasonable to conclude that the formation of the ENP layer initiated at *Interface I*, which was the interface between the top oxide layer and ENP layer, and it should be considered separately from the initial oxidation.

The reason behind the formation of the ENP layer rooted back at the original atomic structure of the film. As we discussed earlier, "nitrogen saturation" led to dominance of nitrogen-containing bonds. Similarly, higher silicon concentration would lead to more Si-Si bonds. In a recent study on the thermal stability of Si-B-C-N films [41-45], it was concluded that abundance of Si-Si bonds within Si-B-C-N network led to crystallization of Si_3N_4. It is because Si-Si bonds became unstable when the

temperature approached the melting point of Si (1414 °C), favoring the Si diffusion within the volume which could resulted in formation of new bonds and crystallization of the material. In the case of $Hf_6B_{10}Si_{31}C_2N_{50}$ film, Si-Si bonds were suppressed by more dominant and stable Si-N bonds. However, during the oxidation process, as some of the elements such as boron, carbon and nitrogen were being released from the film, reconfiguration of atomic bonds between the remaining elements, together with newly incorporated oxygen, would be expected where high silicon concentration would play a significant role. Silicon atoms with high mobility would grab the remaining nitrogen to crystallize into Si_3N_4. The crystallization might be heavily favored and led to fast growth of Si_3N_4 because the ratio of silicon vs nitrogen was close to 0.75, Si_3N_4's stoichiometry number. Meanwhile, the binding between Hf and O would be favored in the oxidizing environment, leading to the formation of HfO_2, as formation enthalpy of HfO_2 is -1113.2 kJ/mol, much lower than that of HfN at -369.2 kJ/mol [65]. At the same time, formation enthalpy of Si_3N_4 is -850.9 kJ/mol, in between HfO_2 and HfN [66]. Thus, thermodynamically speaking, co-existence of Si_3N_4 and HfO_2 is possible in the ENP layer. The downward growth of Si_3N_4 and HfO_2 grains would open fast diffusion path for oxygen within the grain boundaries. As a result, oxygen would diffuse through the ENP layer at a faster rate than through a dense and amorphous layer. After reaching the bottom of the ENP layer, it reacted with the atoms from the amorphous bottom layer, breaking the original atomic network and eventually led to formation of more Si_3N_4 and HfO_2 through coalescent growth. Thus, it effectively explains the elongation of the HfO_2 grains observed by TEM analysis.

In summary, higher silicon concentration of the film promoted the partial oxidation and growth of the ENP layer, when oxidation destabilized the original microstructure. Growth of HfO_2 in the ENP layer was likely restrained heavily by the geometry of rigid Si_3N_4 matrix, putting significant pressure on the HfO_2. As a result, only high energy form of HfO_2 could be observed throughout the ENP layer. It was concluded that some of these HfO_2 grains transformed into lower energy monoclinic form, once the pressure was released when Si_3N_4 was oxidized into amorphous SiO_x, which happened at *Interface I*. Also, amorphous SiO_x would be a glassy-like matrix at high temperature unlike Si_3N_4 which maintained its solid form. Thus, HfO_2 would transform into spherical particles in the top oxide layer in order to minimize the surface energy. As a final result, a completely different microstructure between fully oxidized top layer and partially oxidized ENP layer was observed.

4.4.2.2 Reduced thickness of the top oxide layer

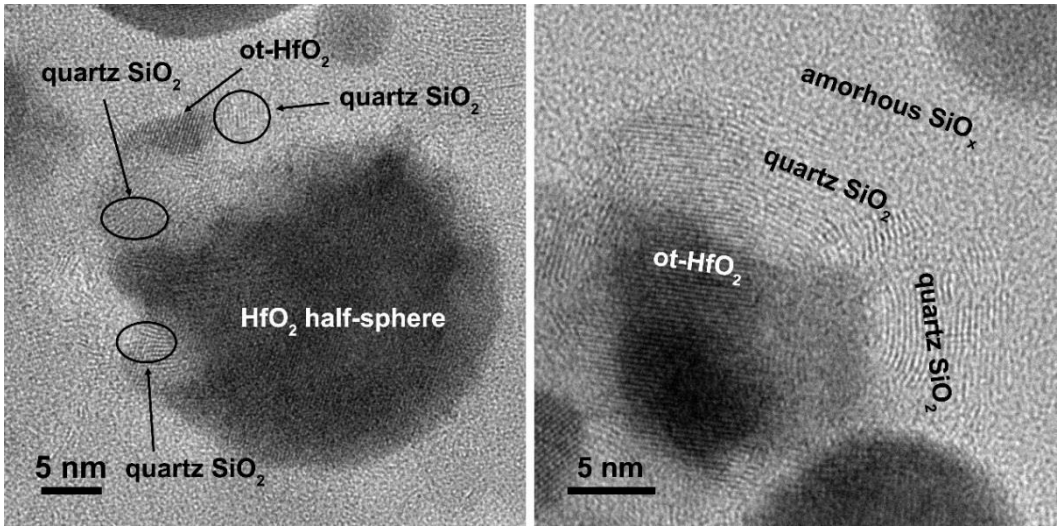

Fig. 49 HRTEM images of *Interface I* in $Hf_6B_{10}Si_{31}C_2N_{50}$ film illustrating the following microstructure: a HfO_2 half-sphere which was already released from the ENP layer, small ot-HfO_2 particles being restrained by quartz-SiO_2 and amorphous SiO_x in the top oxide layer.

In both $Hf_7B_{10}Si_{32}C_2N_{44}$ and $Hf_6B_{10}Si_{31}C_2N_{50}$ films, the thickness of the top oxide layer was reduced, which was directly related to increased concentration of silicon and the resulted Si_3N_4 formation in the ENP layer. Si_3N_4 was hard to oxidize and typically considered as a great oxidation resistant material. For example, the standard formation enthalpy of SiO_2, which is -910 kJ/mol, is considerably higher than that of HfO_2. Meanwhile, the standard formation enthalpy of Si_3N_4 (-850 kJ/mol), is much lower than that of HfN. As a result, the driving force of the oxidation of Si_3N_4 is lower, while the activation energy is higher, when compared to the oxidation of HfN. Thus, the fully oxidized top layer where Si_3N_4 completely oxidized into amorphous SiO_x, was a lot thinner in $Hf_7B_{10}Si_{32}C_2N_{44}$ and $Hf_6B_{10}Si_{31}C_2N_{50}$ film than $Hf_7B_{23}Si_{22}C_6N_{40}$ and $Hf_6B_{21}Si_{19}C_4N_{47}$ film. One noticeable microstructure feature in both samples is the size uniformity of the HfO_2 particles in the top oxide layer, which was related to the formation mechanism of these particles. Fig. 49a is a plan-view TEM image capturing a HfO_2 half sphere near *Interface I* in $Hf_6B_{10}Si_{31}C_2N_{50}$ film. In addition, a small ot-HfO_2 particle, in which (111) planes were clearly visible, can be observed surrounded by extensive quartz-SiO_2 (marked by black circle). Fig. 49b was another great visual representation of the microstructure of *Interface I* taken from a cross-section TEM sample illustrating a small ot-HfO_2 grain of which the entire upper part was surrounded by curved quartz-SiO_2. These quartz-SiO_2 crystalline structure was likely the immediate product of Si_3N_4 oxidation at *Interface I*. Highly intense quartz-SiO_2 would heavily regulate the shape and size of ot-HfO_2 at *Interface I*, just as shown in Figs. 49a and 49b. However, as *Interface I* progressed deeper into the film these quartz-SiO_2 would

quickly melt into amorphous SiO_x and release those HfO_2 grains which would then directly merge into the existing HfO_2 particles near *Interface I*. The spherical shape of HfO_2 would also start to form once the presence of surrounding crystalline SiO_2 was gone. Quartz-SiO_2, similarly to those existing in the previously studied films, would act as oxygen diffusion barrier and improve the oxidation resistance.

4.4.2.3 Partial oxidation of the nanocrystalline layer in $Hf_7B_{10}Si_{32}C_2N_{44}$ film

Partial oxidation of the nanocrystalline layer happened in the following sequence: first, the "recrystallization" of the original amorphous film into a nanocrystalline layer without oxidation, similarly to what happened in $Hf_7B_{23}Si_{22}C_6N_{40}$ film, then, the preferential oxidation of Hf-containing grains of the nanocrystalline layer. This would explain the notable microstructure difference between the ENP layer and the nanocrystalline layer despite both being partially oxidized. The formation of ENP layer was similar to what was discussed in the Part 4.4.2.1 despite only $Hf_6B_{10}Si_{31}C_2N_{50}$ film was used as an example. In the nanocrystalline layer of $Hf_7B_{10}Si_{32}C_2N_{44}$ film however, the oxidation took place after the crystalline structure already in place, oxidizing the Hf-containing grains (mostly HfN) into HfO_2. The prior transformation from amorphous structure to nanocrystalline structure could be referred to the previous discussion (Part 4.1) which started with nucleation across the whole bottom layer and did not prefer specific growth direction. The metastable nature due to lack of nitrogen abundance was the ultimate reason. It was likely that increased silicon further reduced the thermal stability by statically increasing Si-Si bonds. Preferential oxidation of HfN would not change the overall microstructure since all HfO_2 would have been confined

by existing Si_3N_4. However, significant amount of internal stress could be built up during the process as a consequence of unit cell size difference between HfO_2 and HfN. Each HfN unit cell accommodates 4 Hf and 4 N atoms, occupying space of 4.55 x 4.55 x 4.55 $Å^3$. While a t-HfO_2 unit cell accommodates 4 Hf and 8 O atoms, occupying much larger space of 5.14 x 5.14 x 5.25 $Å^3$. Orthorhombic HfO_2 is slightly smaller but is still 1.4 times larger than HfN. Internal pressure helped maintain the high energy phase of HfO_2, preventing the formation of m-HfO_2 across the partially oxidized part of the nanocrystalline layer. Also, it would offer another possible explanation to the difference in overall film thickness between $Hf_7B_{10}Si_{32}C_2N_{44}$ and $Hf_6B_{10}Si_{31}C_2N_{50}$ film. The thickness of $Hf_7B_{10}Si_{32}C_2N_{44}$ film was about 1.9 μm, which is about 600 to 700 nm larger than $Hf_6B_{10}Si_{31}C_2N_{50}$ film. For reference, the difference in thickness between $Hf_7B_{23}Si_{22}C_6N_{40}$ and $Hf_6B_{21}Si_{19}C_4N_{47}$ film was only about 320 nm. It was likely due to significant amount of volume increase, the nanocrystalline layer had to expand in order to accommodate larger HfO_2 crystalline structure. In addition, the oxide-free part of the nanocrystalline layer was very likely not “oxygen-free”. Small amount of diffused oxygen could migrate fast via grain boundaries without altering the crystalline structure. It was entirely possible that some of them had reached the substrate. Again, it demonstrated that polycrystalline structure is prone to oxidation when oxygen aggressively invades the structure.

4.4.2.4 Summary

If we consider oxygen diffusion distance as the sole factor determining the oxidation resistance of the film, then both $Hf_7B_{10}Si_{32}C_2N_{44}$ and $Hf_6B_{10}Si_{31}C_2N_{50}$ films did

not outperform the previously studied $Hf_7B_{23}Si_{22}C_6N_{40}$ and $Hf_6B_{21}Si_{19}C_4N_{47}$ films which had lower silicon vs boron ratio. In $Hf_6B_{10}Si_{31}C_2N_{50}$ film, oxygen diffused through 540 to 550 nm, In $Hf_7B_{10}Si_{32}C_2N_{44}$ film, it was at least 1.3 μm. In both $Hf_7B_{23}Si_{22}C_6N_{40}$ and $Hf_6B_{21}Si_{19}C_4N_{47}$ films, it was about 350 nm. The formation of ENP layer attributed to extended permeation distance in both $Hf_7B_{10}Si_{32}C_2N_{44}$ and $Hf_6B_{10}Si_{31}C_2N_{50}$ films. In addition, prior crystallization of the bottom layer in $Hf_7B_{10}Si_{32}C_2N_{44}$ film further promoted the fast oxygen permeation, while in $Hf_6B_{10}Si_{31}C_2N_{50}$ film it was stopped by the dense microstructure at *Interface II*. Oxygen diffusing rapidly through the grain boundaries of the existing crystalline structure was the main diffusion mechanism.

The initial idea of increasing silicon vs boron ratio was simple, as silicon was much harder to be oxidized compared to boron. The results of increasing the ratio from 1:1 to almost 3:1 changed the film chemistry so that formation of crystalline Si_3N_4 was heavily favored, which generated an undesired side effect. This side effect was not particularly related to Si_3N_4 itself, but rather related to the grain boundaries it created when forming polycrystalline structure. The direct consequence was the so-called “partial oxidation” as diffusion rate was so high that oxygen could reach into much deeper part of the film before Si_3N_4 was yet to be oxidized. The situation was made worse if the film was not thermally stable at high temperatures. The favorable reaction between permeated oxygen and HfN after its recrystallization from the original amorphous structure was heavily restrained by the rigid but oxidation resistant Si_3N_4 matrix. The combined result created unnecessary internal stress and led to cracking of the film surface. Despite that, the ideal of increasing silicon vs boron ratio is still

promising, which was demonstrated by the reduced thickness of the top oxide layer. It is suspected that a threshold value in between 1:1 and 3:1 may exist, so that better oxidation resistance could be achieved. The value is higher than 1:1, so a thinner top oxide layer, compared to $Hf_7B_{23}Si_{22}C_6N_{40}$ film and $Hf_6B_{21}Si_{19}C_4N_{47}$ film, could be expected. At the same time, the value is lower than 3:1 to prevent the favorable formation and fast growth of Si_3N_4 that "accelerate" the oxygen permeation and promote the growth of partially oxidized ENP layer. It will be also important to keep nitrogen concentration high enough to ensure thermal stability of the film. The goal is to prevent prior crystallization before the film was oxidized, so that volume expansion during oxidation is less likely to cause internal stress built-up, and structural integrity of the film will be preserved.

4.5 Effect of Rare Earth Additives on the Microstructure and Oxidation Resistance

4.5.1 Overall microstructure

Table 9 summarized the deposition conditions and composition difference between two Hf-B-Si-RE-C-N films and $Hf_7B_{10}Si_{32}C_2N_{44}$ films studied in the previous section. Deposition of both $Hf_6B_{12}Si_{29}Y_2C_2N_{45}$ and $Hf_5B_{13}Si_{25}Ho_3C_2N_{48}$ films is similar to the deposition of $Hf_7B_{10}Si_{32}C_2N_{44}$ film, only varied in metallic target composition. As a result, both $Hf_6B_{12}Si_{29}Y_2C_2N_{45}$ and $Hf_5B_{13}Si_{25}Ho_3C_2N_{48}$ films have slightly less Hf, giving room for 2 to 3 % of rare earth elements. It was worth noticing that in $Hf_6B_{12}Si_{29}Y_2C_2N_{45}$ film Y vs Hf ratio is 1:3, while in the $Hf_5B_{13}Si_{25}Ho_3C_2N_{48}$ film the Ho vs Hf ratio increased to 2:5, which was caused by reduced Hf and increased Ho concentration together. Also, for films with RE additives, boron and nitrogen increased while silicon concentration reduced. However, all these changes are relatively small.

Table 9 Deposition conditions of $Hf_6B_{12}Si_{29}Y_2C_2N_{45}$, $Hf_5B_{13}Si_{25}Ho_3C_2N_{48}$ and $Hf_7B_{10}Si_{32}C_2N_{44}$ film.

	$Hf_6B_{12}Si_{29}Y_2C_2N_{45}$	$Hf_5B_{13}Si_{25}Ho_3C_2N_{48}$	$Hf_7B_{10}Si_{32}C_2N_{44}$
Hf (% of the target)	15	15	20
Y (% of the target)	5	-	-
Ho (% of the target)	-	5	-
B_4C (% of the target)	30	30	30
Si (% of the target)	50	50	50
N (% of the gas flow)	25	25	25

TEM study of both RE-doped films showed that adding rare earth elements had significant impact on the microstructure of the annealed films. Figs. 50a and 50b illustrate the cross-section TEM image of $Hf_6B_{12}Si_{29}Y_2C_2N_{45}$ and $Hf_5B_{13}Si_{25}Ho_3C_2N_{48}$ film, respectively. Both films possessed similar morphology, with three layers clearly visible: a top layer with dark spherical particles embedded within a bright matrix, an elongated nanoparticle (ENP) layer and a fully crystallized nanocrystalline bottom layer. This structural layout was exceedingly close to the overall structure of $Hf_7B_{10}Si_{32}C_2N_{44}$ film given the fact that they shared similar deposition parameters. However, several noticeable differences could be observed. Generally speaking, the two RE-doped films were both about 2.1 to 2.2 μm in thickness, about 300 to 400 nm thicker than $Hf_7B_{10}Si_{32}C_2N_{44}$ film. However, the top oxide layer in both Hf-B-Si-RE-C-N films was considerably thinner compared to $Hf_7B_{10}Si_{32}C_2N_{44}$ film. In both cases the thickness of the oxide layer was less than 190 nm, which was about 70 nm thinner than non-dopant film. The ENP layer in $Hf_6B_{12}Si_{29}Y_2C_2N_{45}$ film was about 300 to 340 nm thick, while the similar ENP layer in $Hf_5B_{13}Si_{25}Ho_3C_2N_{48}$ film was about 280 to 300 nm thick. However, finding the exact interface between the ENP layer and the nanocrystalline bottom layer was deemed difficult, as in both RE-doped samples, the nanocrystalline bottom layer was not homogeneous. A trend of grain growth starting from the bottom could be observed, and at the top of the nanocrystalline layer, the morphology of the grain network was comparable with the ENP layer although it did not have preferred orientation. The nanocrystalline layer could be divided into three sublayers based on the overall microstructure, especially the grain size and density. At the bottom, high

density small grains could be observed, in which the area was denoted as *SL-I*. The smaller grains coarsened in areas denoted as *SL-II* and even bigger in *SL-III*. No clearly visible interface could be found in between the three sublayers, indicating that no major reactions that would cause violent crystallographic and morphological changes happened. Instead, the change in morphology was a result of grain coarsening process.

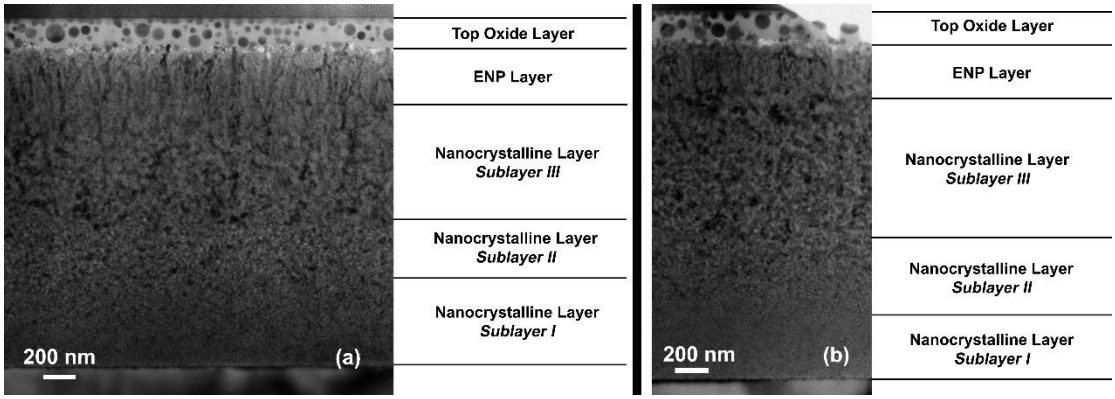

Fig. 50 Bright-field TEM image of the cross-section TEM foil of (a) $Hf_6B_{12}Si_{29}Y_2C_2N_{45}$ and (b) $Hf_5B_{13}Si_{25}Ho_3C_2N_{48}$ film.

XRD surveys of the two Hf-B-Si-RE-C-N films were used to extract crystallographic information from the samples and are presented in Fig. 51a. Low-angle XRD method was used to avoid the excessive signal from SiC substrate. Major peaks that resemble Hf-RE-O fluorite oxide were observed. Typically, cubic hafnium oxide (c-HfO_2) is only stable at temperatures higher than 2500 °C [62, 68]. However, by adding some of the rare earth elements, Hf, as well as Zr, will be able to form Hf(Zr)-RE-O solid solution that closely resembles the crystalline structure of fluorite or pyrochlore at lower temperatures (RE=La, Nd, Sm, Eu, Gd, Tb, Dy, Ho, Er, Tm, Yb and Y) [69-74]. For example, Stacy and Wilder who studied the Hf-Y-O system reported that addition of Y, as little as 5 mol% (2000 °C) to 10 mol% (1200 °C) would help maintain the cubic structure of HfO_2 [69]. The charge neutrality was preserved by formation of an anion vacancy

defect structure as Y randomly substitutes Hf within the lattice. Thus, these types of solid solutions were also called (RE oxide) stabilized hafnia (zirconia). It was found out that Y and Ho can form only fluorite oxide with HfO_2, while some other elements such as La could form pyrochlore structure ($La_2Hf_2O_7$), which is crystallographically more ordered and thus, more thermally stable. As the concentration of Y and Ho increases, the cell dimensions of these fluorite oxides also increase. For example, the unit cell of Hf-Y-O is around 5.13 x 5.13 x 5.13 $Å^3$ when Y_2O_3 reaches 10 mol%, and it increases to almost 5.22 x 5.22 x 5.22 $Å^3$ when Y_2O_3 concentration increased to 40 mol% [69]. Similar trend was observed in the Hf-Ho-O system as well. It was mostly due to larger ion radius of Y^{3+} and Ho^{3+} compared to Hf^{4+} [74]. In the XRD spectra of $Hf_6B_{12}Si_{29}Y_2C_2N_{45}$ film, the (111) peak of Hf-Y-O fluorite oxide is at 30.09˚ while the (200) peak is at 34.85˚, which mean the unit cell of Hf-Y-O had a length of 5.14 Å. For $Hf_5B_{13}Si_{25}Ho_3C_2N_{48}$ film, the peaks of Hf-Ho-O universally shift to lower angles, as shown in Fig. 51b, which illustrates part of the XRD spectra in the range between 28˚ and 36˚. The (111) peak of Hf-Ho-O fluorite oxide is at 29.96˚, while the (200) peak is at 34.64˚, which mean the unit cell of Hf-Ho-O was slightly larger, with a length of 5.17 Å. Higher Ho vs Hf ratio in $Hf_5B_{13}Si_{25}Ho_3C_2N_{48}$ film compared to Y vs Hf ratio in the other film might play a role. No trace of Y_2O_3 or Ho_2O_3 phase was found. Thus, it's reasonable to consider all oxidized rare earth elements had been oxidized into Hf-RE-O fluorite oxides. Less obvious peaks including the HfN (111) appeared in both films. Most rare earth elements, including Ho and Y, can form rare earth mononitride having a FCC NaCl crystalline structure, which is exactly the same as HfN despite having different lattice

parameters [75]. Studies showed that Y doped ZrN could maintain a ZrN crystalline structure with minor unit cell dimensions change without the presence of second phase maintaining a stoichiometry with N vs metal (Zr+Y) ratio of 1:1 [76, 77]. Very few studies have focused on the Hf-Y-N or Hf-Ho-N system, but it is reasonable to believe that they share similarities with the Zr-Y-N system. Peaks of Si_3N_4 were also found in both patterns. However, most of them are very weak compared to Hf-RE-O peaks.

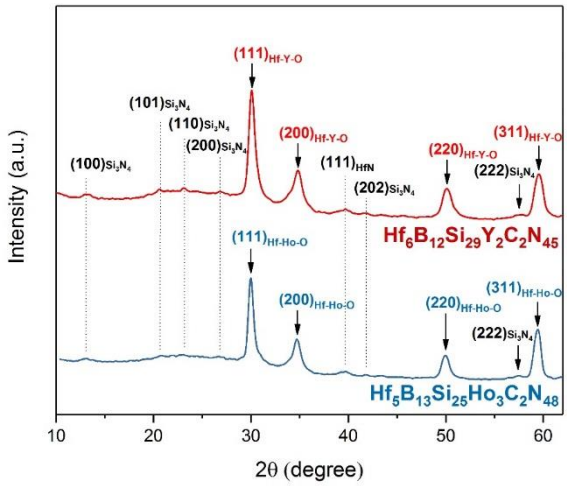

(a)

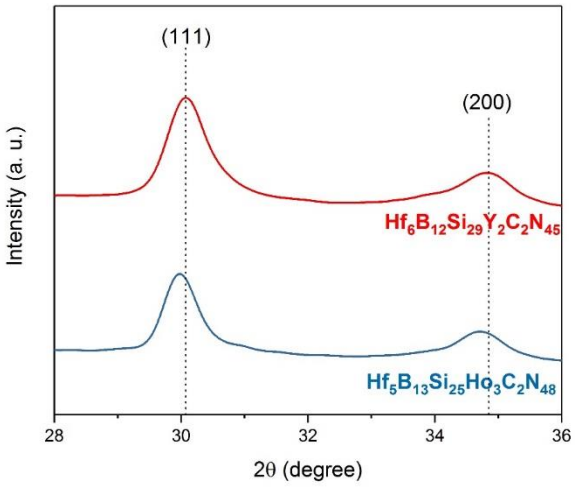

(b)

Fig. 51 (a) Low-angle XRD spectra of $Hf_6B_{12}Si_{29}Y_2C_2N_{45}$ and $Hf_5B_{13}Si_{25}Ho_3C_2N_{48}$ film and (b) the same spectra in the range of 28˚ and 36˚ exclusively showing the (111) and (200) peak of fluorite oxide.

4.5.2 Top Oxide Layer

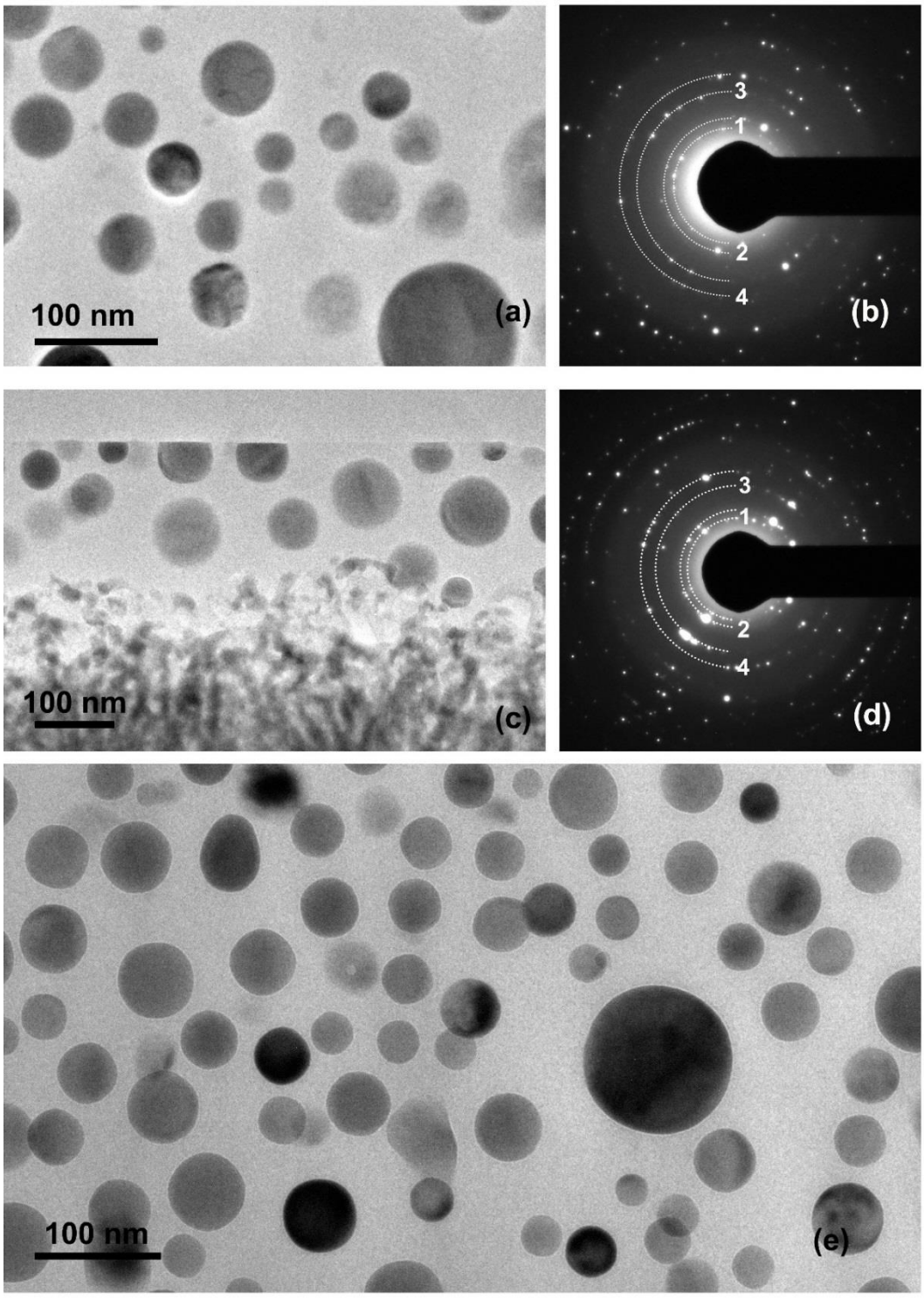

Fig. 52 (a) A plan-view TEM image and (b) the corresponding SAED pattern taken from the top oxide layer in $Hf_6B_{12}Si_{29}Y_2C_2N_{45}$ film, (c) a cross-section TEM image, (e) a plan-view TEM image and the corresponding SAED pattern taken from the top oxide layer in $Hf_5B_{13}Si_{25}Ho_3C_2N_{48}$ film.

Fig. 52 contains several TEM images and SAED patterns taken from the top oxide layer from either $Hf_6B_{12}Si_{29}Y_2C_2N_{45}$ film (Figs. 52a and 52b) or $Hf_5B_{13}Si_{25}Ho_3C_2N_{48}$ film (Figs. 52c, 52d and 52e). For example, Fig. 52a was taken from a plan-view TEM sample of $Hf_6B_{12}Si_{29}Y_2C_2N_{45}$ film revealing the microstructure of the oxide layer, and Fig. 52b is the corresponding SAED pattern. Four diffraction rings were identified and marked in the pattern, each corresponding to one of the lattice parameters in Hf-Y-O fluorite oxide. All four of them match with the XRD results as well. Figs. 52c and 52e were taken from a cross-section TEM sample and a plan-view TEM sample of $Hf_5B_{13}Si_{25}Ho_3C_2N_{48}$ film showing the typical spherical particles in the amorphous matrix. In the corresponding SAED pattern from the area, which is shown as Fig. 52d, four diffraction rings were identified. Again, all four rings match with XRD results and correspond to (111), (200), (220) and (311) planes of Hf-Ho-O fluorite oxde, respectively. In both films, the thickness of the oxide layer was around 180 to 190 nm, a value significantly smaller than any previous films. Also, the particle size was very ununiform. The largest particle had a diameter of 100 to 120 nm. However, most of these particles were way smaller, in the range between 30 to 60 nm. There were also particles having much smaller dimensions from 10 to 20 nm. Like the large ones, their numbers were relatively small. A significant size variation may indicate strong particle coarsening in the oxide layer. The detailed crystallographic information from individual fluorite oxide particles was also extracted by nanobeam diffraction (NBD). For example, Fig. 53a is a TEM image taken from the top oxide layer in $Hf_5B_{13}Si_{25}Ho_3C_2N_{48}$ film and the NBD pattern of two individual particles, denoted as P1 and P2, are presented in Figs. 53b and 53c,

respectively. Both P1 and P2 could be identified possessing a fluorite structure with different orientations. NBD of P1 was taken when one of the <103> zone axis was parallel to the beam, showing the diffraction from {200} and {311} planes. The NBD of P2 was taken when one of the <114> zone axis was parallel to the beam, showing the diffraction from {220} and {311} planes. Both these results match with XRD and SAED pattern analysis.

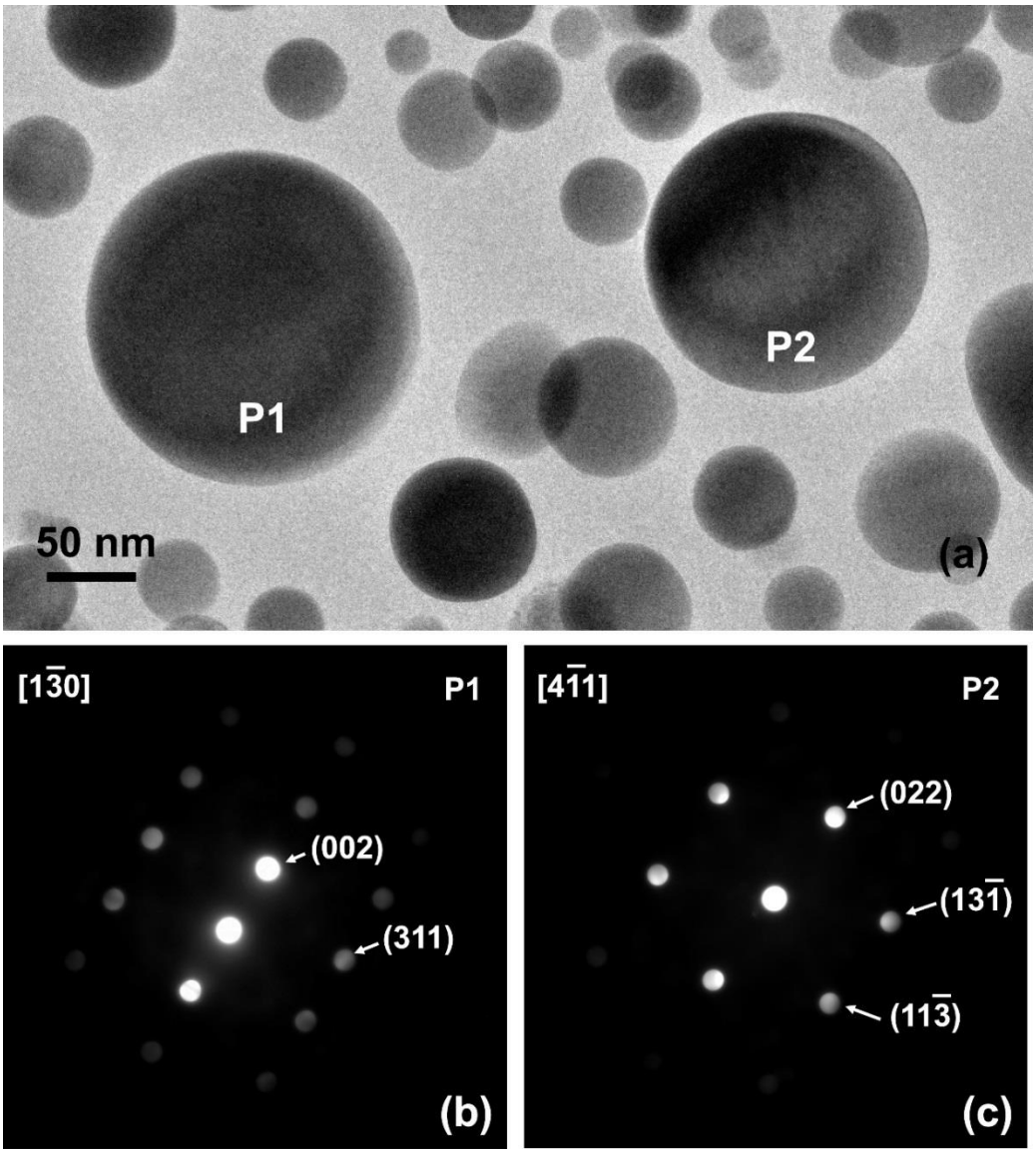

Fig. 53 (a) A PV-TEM image taken from the oxide layer in $Hf_5B_{13}Si_{25}Ho_3C_2N_{48}$ film and (b) & (c) two NBD patterns captured from the two particles denoted as P1 and P2 in the TEM image.

4.5.3 ENP Layer

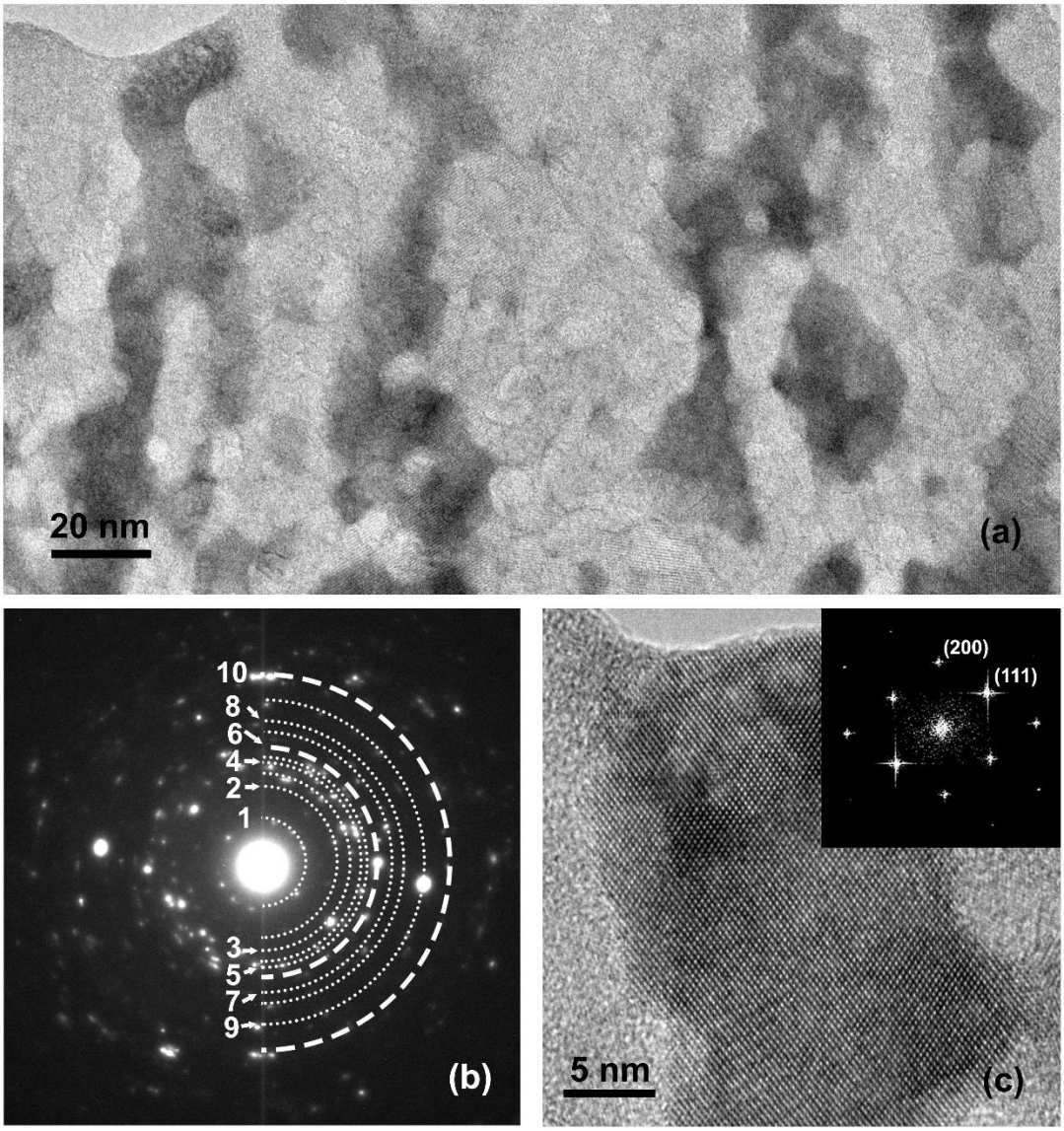

Fig. 54 (a) A bright-field TEM image, (b) the corresponding SAED pattern and (c) a HRTEM image showing the crystalline structure of the Hf-Ho-O fluorite oxide grains of the ENP layer in $Hf_5B_{13}Si_{25}Ho_3C_2N_{48}$ film.

The ENP layer was characterized as anisotropic extension of ot-HfO_2 grains towards the substrate within Si_3N_4 matrix induced by favored Si_3N_4 crystallization and accelerated oxygen diffusion in the discussion of $Hf_7B_{10}Si_{32}C_2N_{44}$ and $Hf_6B_{10}Si_{31}C_2N_{50}$ films. The general microstructure features of the ENP layers in the Hf-B-Si-RE-C-N films were similar. However, fluorite oxide was observed in this layer instead of HfO_2. Fig. 54

Table 10 Analysis results of the SAED pattern taken from the ENP layer in $Hf_5B_{13}Si_{25}Ho_3C_2N_{48}$ film.

Ring No.	Measured d-spacing (Å)	Index
1	6.71	Si_3N_4 (100)
2	3.91	Si_3N_4 (110)
3	3.33	Si_3N_4 (200)
4	2.97	Hf-Ho-O (111)
5	2.82	Si_3N_4 (002)
6	2.51-2.65	Si_3N_4 (210)/(102) Hf-Ho-O (200)
7	2.22-2.28	Si_3N_4 (300)/(112)
8	2.07	Si_3N_4 (301)
9	1.81	Si_3N_4 (103) Hf-Ho-O (220)
10	1.56-1.60	Si_3N_4 (320)/(312)/(222) Hf-Ho-O (311)

contains a low-magnification TEM image of the ENP layer in $Hf_5B_{13}Si_{25}Ho_3C_2N_{48}$ film illustrating the elongated fluorite oxide grains and the surrounding matrix and the corresponding SAED pattern. A total of ten diffraction rings were identified. A summary of the analysis results is given in Table 10. It was clear that both Si_3N_4 and Hf-Ho-O fluorite oxide co-existed in this layer. Fig. 54c is a HRTEM image taken from one of the fluorite oxide grains, illustrating its crystalline structure. The (111) and (200) planes of the fcc-cubic structure were identified, showing that it was in view of $[0\bar{1}1]$ zone axis. Fig. 55a is another TEM image taken from the ENP layer in $Hf_6B_{12}Si_{29}Y_2C_2N_{45}$ film, and Fig. 55b is the corresponding SAED pattern. They both show that despite adding a different rare earth element, the microstructure of the ENP layer was similar to the other film. Table 11, which summarizes the SAED pattern analysis results of Fig. 55b, contains crystallographic information of various lattice parameters of Si_3N_4 and Hf-Y-O fluorite oxide.

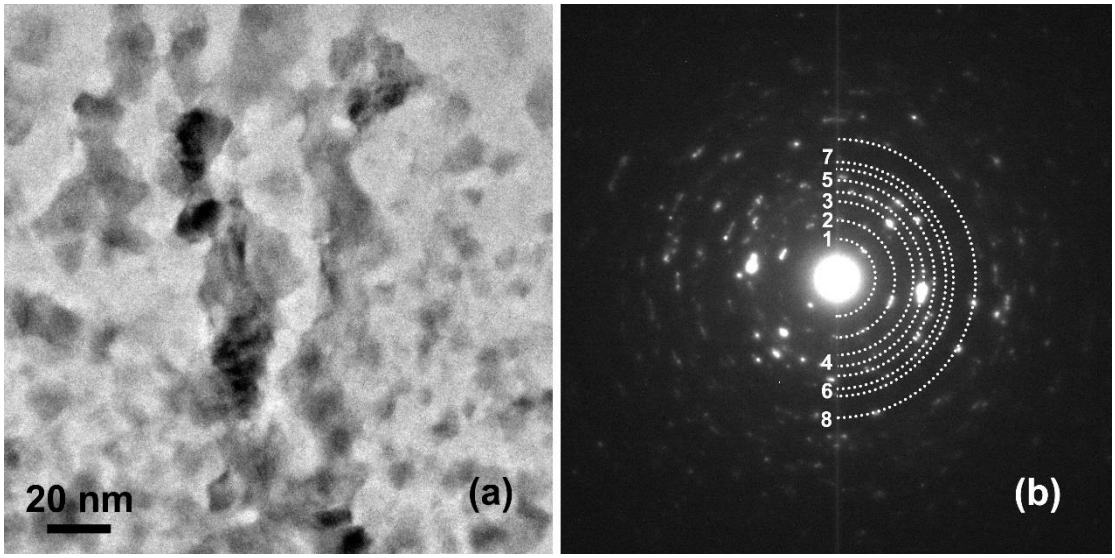

Fig. 55 (a) A bright-field TEM image and (b) the corresponding SAED pattern of the ENP layer in $Hf_6B_{12}Si_{29}Y_2C_2N_{45}$ film.

Table 11 Analysis results of the SAED pattern taken from the ENP layer in $Hf_6B_{12}Si_{29}Y_2C_2N_{45}$ film.

Ring No.	Measured d-spacing (Å)	Index
1	6.72	Si_3N_4 (100)
2	4.30	Si_3N_4 (101)
3	3.33	Si_3N_4 (200)
4	2.93	Hf-Y-O (111)
5	2.53-2.57	Si_3N_4 (210)/(102) Hf-Y-O (200)
6	2.27	Si_3N_4 (300)/(112)
7	2.15	Si_3N_4 (102)
8	1.80	Si_3N_4 (103) Hf-Y-O (220)

4.5.4 Nanocrystalline Layer

The formation of the nanocrystalline layer in both Hf-B-Si-RE-C-N film had similarities to the one in $Hf_7B_{10}Si_{32}C_2N_{44}$ film. Despite artificially divided into three sublayers, it was found out that progressive oxidation happened across the whole thickness of the nanocrystalline layer. Just like the case in $Hf_7B_{10}Si_{32}C_2N_{44}$ film, less

oxidation product was found in areas closer to substrate. However, in both RE-doped films, oxidation happened across the whole nanocrystalline layer even at the bottom and oxidation product, mainly Hf-RE-O, could be found in all three sublayers and there was no real oxide-free part in the nanocrystalline layer. $Hf_5B_{13}Si_{25}Ho_3C_2N_{48}$ film was used as an example in Fig. 56. Fig. 56a is a bright-field TEM image of the cross-section of the nanocrystalline layer. On the right side, three SAED pattern taken from *SL-III*, *SL-II* and *SL-I* are presented as Fig. 56b, 56c and 56d, respectively. Unlike the nanocrystalline layer in $Hf_7B_{10}Si_{32}C_2N_{44}$ film, which was relatively homogeneous, the distinguished microstructure features of different sublayers were clearly visible in Fig. 56a. No clear interface between these sublayers could be located, thus, to make the diffraction patterns representative, Fig. 56b was taken from the upper part of *SL-III*, which was very close to the ENP layer, while Fig. 56d was taken from the lower part of *SL-I*, which was near the substrate. The grains were dense and small in *SL-I* and grew progressively bigger in *SL-II* and *SL-III*. In *SL-III*, grains with much larger dimensions were clearly separated by the matrix, which also grew substantially. As a result, the intact diffraction rings in Fig. 56d were replaced by scattered diffraction spots in Fig. 56b. Meanwhile, Fig. 56c was taken in *SL-II*, an area lacking the representative microstructure features from either *SL-I* (small and dense grains) and *SL-III* (large and widely dispersed grains). The detailed crystallographic information extracted from the three SAED patterns is given in Tables 12, 13 and 14. Some important conclusion could be drawn from these results. First, the progressive coarsening of the grains was accompanied by the partial oxidation of Hf and rare earth elements, which formed

fluorite oxide. For example, the SAED pattern of *SL-I* does not contain Hf-Ho-O (111), which has a unique d-spacing of around 2.97 Å. This parameter could be extracted from both the SAED pattern of *SL-II* and *SL-III*. Meanwhile, as oxidation happened through the nanocrystalline layer, HfN gradually diminished. For example, ring 4 in *SL-I*, which was determined as HfN (111), is one of the major bright rings in Fig. 56d as it corresponds to the strongest diffraction from the fcc structure. However, in *SL-II*, ring 6, which corresponds to a similar lattice parameter, shifts towards a smaller value that departs from HfN (111) and is closer to Hf-Ho-O (200). Similarly, ring 5 in *SL-I*, which corresponds to HfN (200), shifts towards a larger value in *SL-II* (ring 7) and *SL-III* (ring 5) while the intensity greatly reduces. In both *SL-II* and S*L-III*, the value is then closer to Si_3N_4 (211)/(112), both of which have a larger d-spacing than HfN (200). Thus, despite having diffraction ring overlapping, the oxidation of HfN into fluorite oxide could still be verified. It is worth noticing that despite the absence of diffraction Hf-Ho-O was found in *SL-I*, HRTEM images show that there were sparse Hf-Ho-O grains forming in this sublayer, and as stated earlier, *SL-I* should not be considered oxide-free. In addition to that, rings 1, 2 and 3 in Fig. 56d which correspond to Si_3N_4 (101), (110) and (201) show patterns representing strong preferred orientation. Considering that this SAED pattern was taken just above the substrate, it indicates that similar Si_3N_4 texture forming at the film/substrate interface in $Hf_7B_{10}Si_{32}C_2N_{44}$ and $Hf_6B_{10}Si_{31}C_2N_{50}$ films formed in $Hf_5B_{13}Si_{25}Ho_3C_2N_{48}$ film as well. The detailed discussion of the microstructure and the formation mechanism can be found at the end of Part 4.4.1.

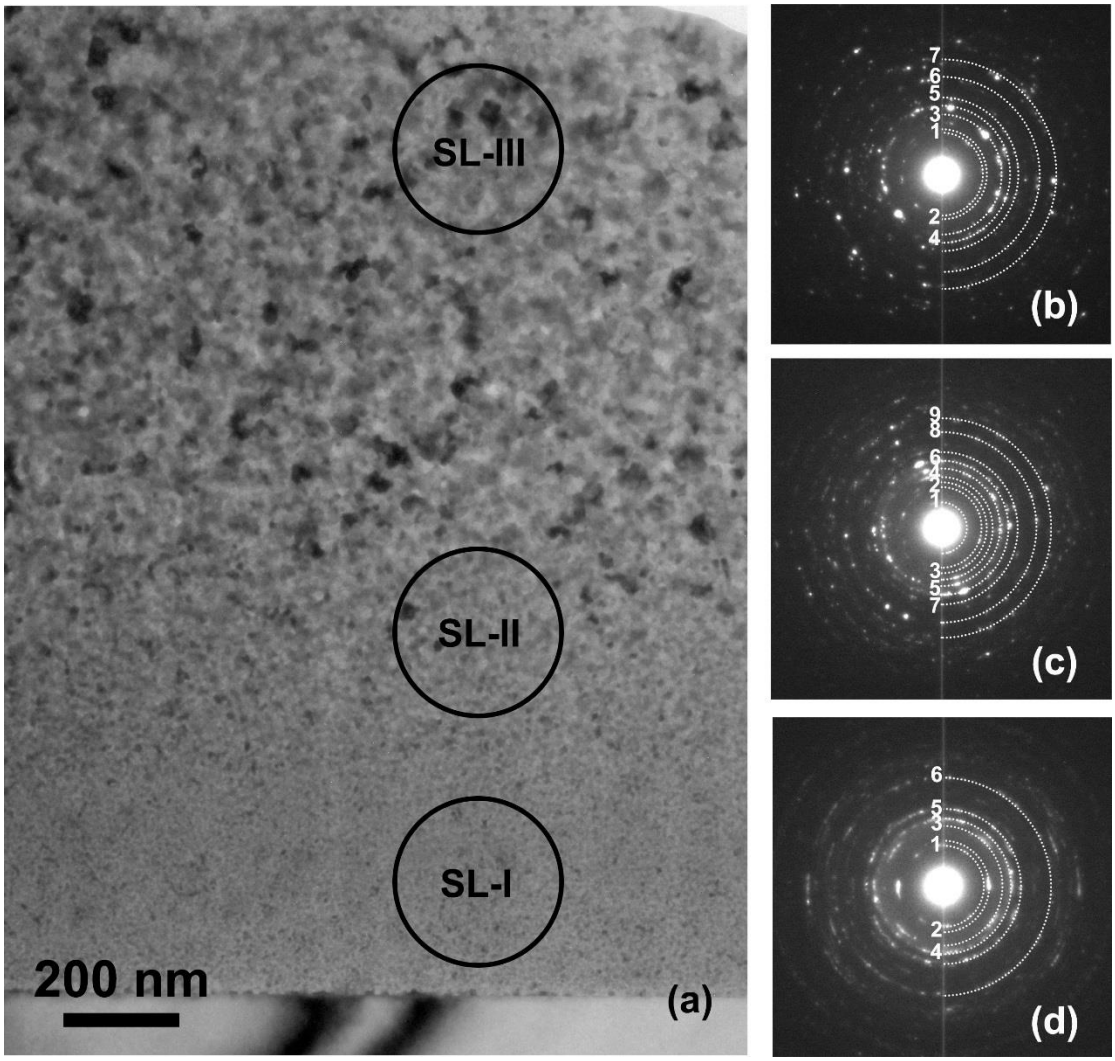

Fig. 56 (a) A bright-field TEM image of the nanocrystalline layer in $Hf_5B_{13}Si_{25}Ho_3C_2N_{48}$ film and the three SAED pattern taken from (b) *SL-III*, (c) *SL-II* and (d) *SL-I* respectively.

Table 12 Analysis results of the SAED pattern taken from *SL-III* of the nanocrystalline layer in $Hf_5B_{13}Si_{25}Ho_3C_2N_{48}$ film.

Ring No.	Measured d-spacing (Å)	Index
1	4.36	Si_3N_4 (101)
2	3.88	Si_3N_4 (110)
3	2.97	Hf-Ho-O (111)
4	2.58	Si_3N_4 (210)/(102) Hf-Ho-O (200)
5	2.30	Si_3N_4 (211)/(112)
6	1.81	Hf-Ho-O (220)
7	1.56	Si_3N_4 (320)/(312)/(222) Hf-Ho-O (311)

Table 13 Analysis results of the SAED pattern taken from *SL-II* of the nanocrystalline layer in $Hf_5B_{13}Si_{25}Ho_3C_2N_{48}$ film.

Ring No.	Measured d-spacing (Å)	Index
1	6.73	Si_3N_4 (100)
2	4.32	Si_3N_4 (101)
3	3.89	Si_3N_4 (110)
4	3.36	Si_3N_4 (200)
5	2.97	Hf-Ho-O (111)
6	2.57-2.61	Si_3N_4 (210)/(102) Hf-Ho-O (200) HfN (111)
7	2.29-2.32	Si_3N_4 (211)/(112) HfN (200)
8	1.81	Hf-Ho-O (220)
9	1.58	Si_3N_4 (320)/(312)/(222) Hf-Ho-O (311) HfN (220)

Table 14 Analysis results of the SAED pattern taken from *SL-I* of the nanocrystalline layer in $Hf_5B_{13}Si_{25}Ho_3C_2N_{48}$ film.

Ring No.	Measured d-spacing (Å)	Index
1	4.33	Si_3N_4 (101)
2	3.83	Si_3N_4 (110)
3	2.89	Si_3N_4 (201)
4	2.62	HfN (111)
5	2.25	Si_3N_4 (211)/(112) HfN (200)
6	1.58	Si_3N_4 (320)/(312)/(222) HfN (220)

In summary, the microstructure of the nanocrystalline layer was a combined result of partial oxidation and grain coarsening under high temperature. In this process, HfN grains were progressively oxidized into Hf-Ho-O fluorite oxide grains, and the dimensions of the grains extended gradually. To get a better understanding of this microstructure evolution, high-magnification images were taken and a few of them are presented in Fig. 57. When comparing Figs. 57a and 57b, which were taken from *SL-I*

and *SL-III,* respectively, it was obvious that the partial oxidation had great impact on the morphology of the grains. The grains in *SL-III*, which were identified as Hf-Ho-O, had almost polygonal shape with very clear transition between each side that formed sharp tips. These tips were seemly connected to the grain boundaries of Si_3N_4 matrix, and these boundaries possessed stronger contrast compared to the pale Si_3N_4 which were also interconnected, forming a boundary network. A clear HRTEM image illustrating these unique microstructure features is presented as Fig. 57d. Grain boundary network surrounding Hf-Ho-O and Si_3N_4 can be clearly seen. No such network could be found in "less oxidized" part of the film, as shown in Fig. 57a of *SL-I*.

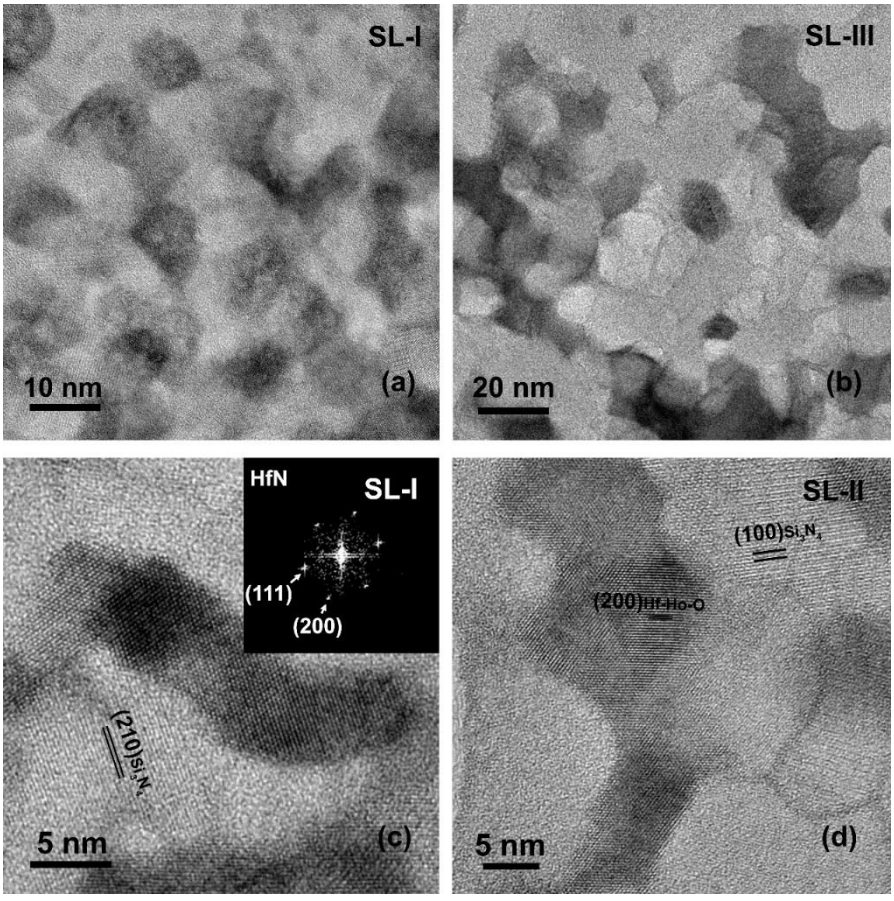

Fig. 57 TEM images taken from various locations of the nanocrystalline layer in $Hf_5B_{13}Si_{25}Ho_3C_2N_{48}$ film illustrating the distinguished microstructure between (a) & (c) "less oxidized" part and (b) & (d) "more oxidized" part, showing difference in grain shape, dimensions and grain boundaries.

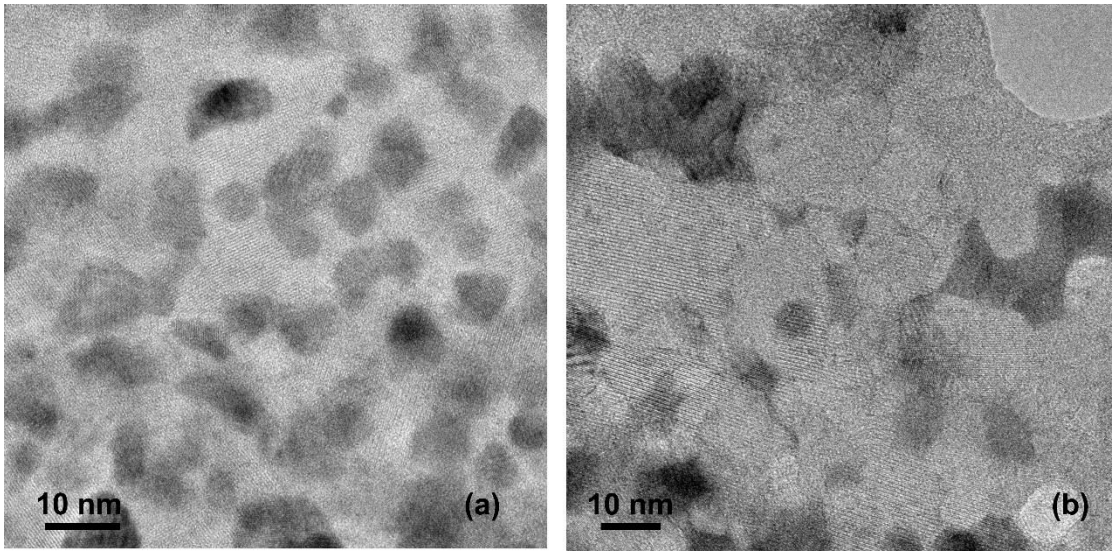

Fig. 58 TEM images of the nanocrystalline layer in $Hf_6B_{12}Si_{29}Y_2C_2N_{45}$ film taken from (a) *SL-I* and (b) *SL-III.*

The grains in *SL-I* have relatively smoother boundaries. In Fig. 57c, which is a HRTEM image taken from *SL-I*, one of such grains is presented. It could be identified as HfN in view of $[0\bar{1}1]$ zone axis. Also, Si_3N_4 was identified and there were no obvious grain boundaries with darker contrast surrounding them. Similar microstructure could be found in $Hf_6B_{12}Si_{29}Y_2C_2N_{45}$ film as well, as shown in Fig. 58. Again, more extensive oxidation and coarsening of the film caused changes in morphology, mostly grain shape and dimensions. Grain boundary network could also be observed in *SL-III*, as shown in Fig. 58b. However, it was not as extensive as in $Hf_5B_{13}Si_{25}Ho_3C_2N_{48}$ film. Fig. 59 contains several HRTEM images illustrating more details of the microstructure from the nanocrystalline layer in $Hf_5B_{13}Si_{25}Ho_3C_2N_{48}$ film. For example, Fig. 59a was taken from an area close to substrate, illustrating a unique HfN-HfB_2-HfN sandwich structure that was not found in other parts of the film. In the zoom-in TEM image (Fig. 59b), HfB_2-(001) could be observed joining coherently with HfN-(111). This specific structure was discussed in the earlier chapters. Again, it exclusively appeared in the lower part

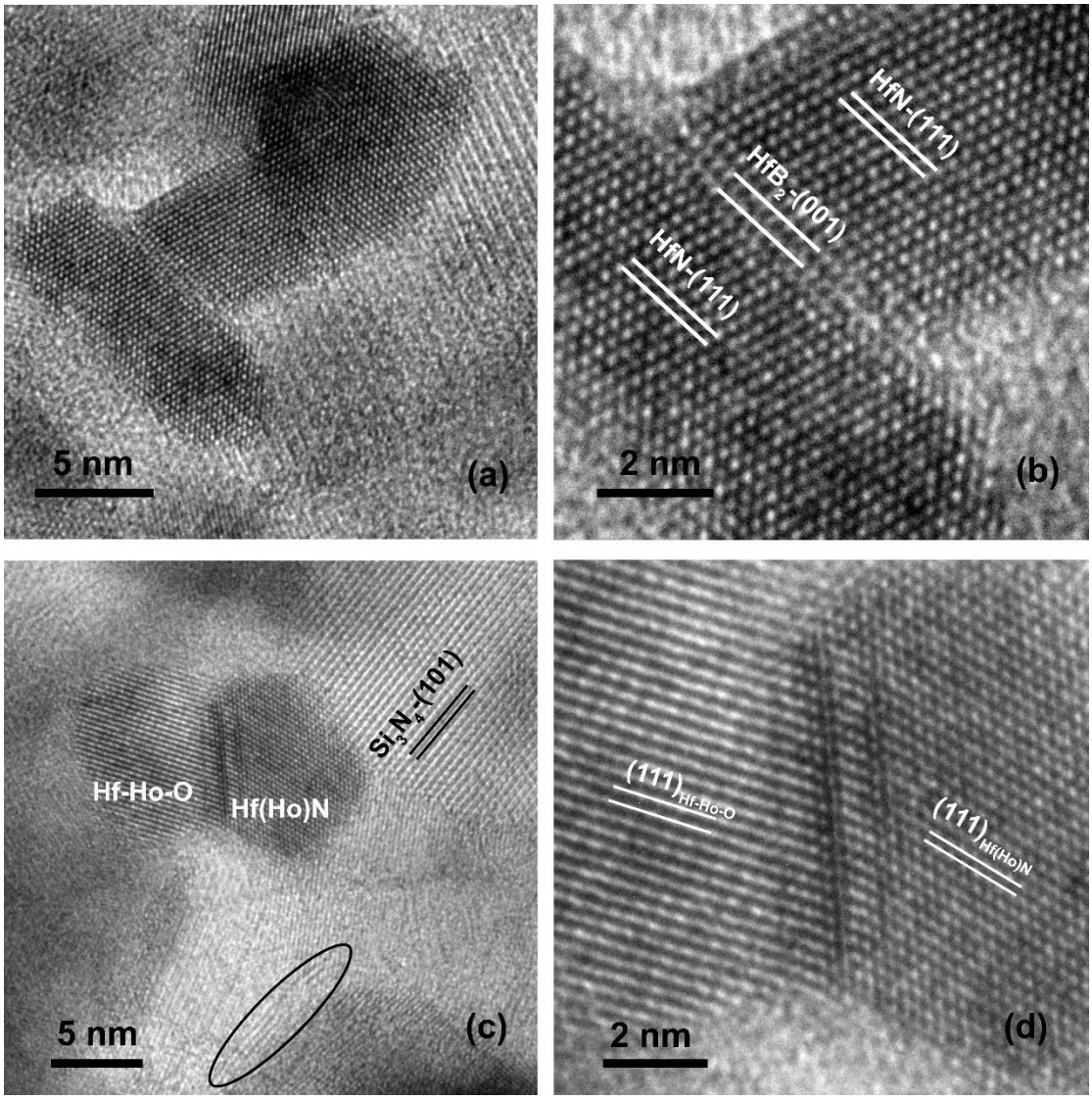

Fig. 59 HRTEM images taken from (a) & (b) *SL-I* illustrating a HfN-HfB_2-HfN sandwich structure and (b) & (d) *SL-II* illustrating a combined hafnium holmium nitride-oxide structure and quartz-SiO_2.

of *SL-I* only, surrounded by Si_3N_4 texture as shown in Fig. 59a. HRTEM images of a combined nitride-oxide structure were captured in *SL-II* as well, which are illustrated as Figs. 59c and 59d. It is highly likely this specific type of structure only existed during the process of oxidation. The distinguished lattice parameters of both Hf(Ho)N and Hf-Ho-O fluorite oxide were identified and marked in Fig. 59d. It was observed that [100] of Hf(Ho)N and [100] of Hf-Ho-O were almost parallel. It is likely that during the oxidation, the fcc-crystalline of Hf(Ho)N transformed directly into cubic fluorite

structure as nitrogen being replaced by oxygen. A transition region was observed between Hf-Ho-O and Hf(Ho)N, where a clear lattice distortion could be observed. The discovery of this combined nitride-oxide grains supports our conclusion that once prior crystallization finished, partial oxidation happened by directly transforming hafnium nitride into hafnium oxide, either with or without rare earth additives. In addition, crystalline structure of the grain boundaries surrounding Si_3N_4, which was possibly part of the grain boundary network observed in Figs. 57b and 57d, was captured in Fig. 59c (circled in black). The d-spacing matches with quartz SiO_2, thus the thickened boundaries were likely the oxidation product of Si_3N_4. This conclusion matches with the fact that this boundary network only appeared in areas with extensive partial oxidation, and was not found in areas such as *SL-I*.

4.5.5 Summary

The microstructure of Hf-B-Si-RE-C-N films shared many similarities with each other. The impact of different elements in the system seemed minimum. In addition, the microstructure of these two RE-doped films shared many similarities with $Hf_7B_{10}Si_{32}C_2N_{44}$ film as well, mainly due to the similar Si and N compositions. The latter one has been thoroughly discussed, and conclusion regarding how concentration of silicon and nitrogen impacted the microstructure after annealing to high temperatures was made. The original purpose of adding rare earth element was to increase the thermal stability. However, we believe that the goal was not achieved. According to

the TEM investigation no rare earth silicate formed during thermal oxidation, which ought to offer great thermal stability. Instead, oxygen preferentially combined with only the metallic elements, while crystallization of Si_3N_4 was heavily favored. Fluorite oxide, when compared with rare earth silicates, is inferior in terms of thermal stability, vastly due to its fundamental microstructure. As a solid solution, Hf-Y-O and Hf-Ho-O fluorite oxide do not have long-range order of atomic arrangement, making its overall thermal stability less appealing. To add on to that, fluorite oxide was oxygen-deficient since Y^{3+} and Ho^{3+} substitute Hf^{4+} creating extra oxygen vacancy which would open up oxygen diffusion path within the crystalline structure. These factors might have contributed to the fact that the partial oxidation was more extensive in the two RE-doped films than $Hf_7B_{10}Si_{32}C_2N_{44}$ film.

The overall idea of adding rare earth elements to the existing Hf-B-Si-C-N film did not bring a satisfying result. However, improvement could be made in the current system. Pyrochlore oxide has long-range order in terms of atomic arrangement and might offer better thermal stability. However, no Hf-Y-O nor Hf-Ho-O pyrochlore oxide exists, substituting Y and Ho with other elements, such as La, Nd would be required. Also, the concentration of the substituting rare earth elements has to be higher in order to form $RE_2Hf_2O_7$ pyrochlore oxide.

4.6 Conclusion

Annealing as-deposited amorphous $Hf_7B_{23}Si_{22}C_6N_{40}$ films to high temperatures (1100 to 1600 °C) in air led to significant microstructure changes. A two-layer structure was observed consisting of a top oxide layer and a bottom layer. The oxide layer formed by HfO_2 nanoparticles skeleton dispersed in borosilicate glass matrix. The thickness of the oxide layer and the average size of HfO_2 particles increased with increasing temperatures. The matrix was mostly amorphous and formed a dense and continuous layer covering the film which would offer great protection against oxidation. The bottom layer gradually transformed into a nanocrystalline composite structure between 1100 and 1300 °C, and then into a crystalline structure between 1400 and 1500 °C. This microstructure changes could then affect the oxidation kinetics at the interface and the microstructure of the oxide layer. On the other hand, annealing $Hf_7B_{23}Si_{22}C_6N_{40}$ films to high temperatures in helium led to the transition of the original amorphous structure to a nanocrystalline composite structure. In the meantime, annealing $Hf_6B_{21}Si_{19}C_4N_{47}$ film at 1500 °C in air did not change the amorphous structure of the unreacted film due to N-saturation in the bonding structure that prevented the recrystallization which could potentially exhibit better oxidation resistance at even higher temperatures. However, by post-deposition treatment, the N sub-saturated $Hf_7B_{23}Si_{22}C_6N_{40}$ films could offer enhanced hardness and good oxidation resistance at the same time, which will meet both requirement for certain applications.

Annealing $Hf_7B_{10}Si_{32}C_2N_{44}$ and $Hf_6B_{10}Si_{31}C_2N_{50}$ film to 1500 ℃ in air led to the formation of ENP layer and partial oxidation of hafnium in both films. It was caused by

increased silicon concentration thus favored Si-Si bonds in the atomic network in the original film, which led to destabilization of the original film network under high temperature oxidation and fast growth of Si_3N_4. The growth of Si_3N_4 promoted further oxidation by offering fast diffusion path for oxygen. We have concluded that higher silicon vs boron ratio does not necessarily improve the oxidation resistance, and fine tuning of it would be required to avoid the fast growth of crystalline Si_3N_4 while reduced the overall oxidation kinetics.

Adding rare earth elements to the current system did not result in the formation of rare earth silicates, which are great thermal barrier materials. Instead, fluorite oxides formed during oxidation. These materials did not have superior thermal stability due to the fundamental property of their crystalline structure. They would not become ideal oxygen diffusion barrier either because they are oxygen deficient. However, the oxidation resistance of Hf-B-Si-RE-C-N films could be improved by adding suitable rare earth element and fine tuning Hf vs RE ratio to form pyrochlore oxides which have better thermal stability and smaller oxygen permeation rate [78].

A "reaction layer" theory was proposed by Stoneham et al. to explain the oxidation of silicon [79-81]. Even though the Hf-B-Si-(RE)-C-N system is more complicated, the theory can still help us explain some of the key questions remained. For example, annealing $Hf_7B_{23}Si_{22}C_6N_{40}$ films did not cause partial oxidation even at 1600 °C when the bottom layer completely recrystallized. However, the oxidation rate was faster at 1500 °C and higher, no longer following the parabolic oxidation law. What is more important, the theory can also help us to determine the film that is most

resistant to thermal oxidation among all films we have studied.

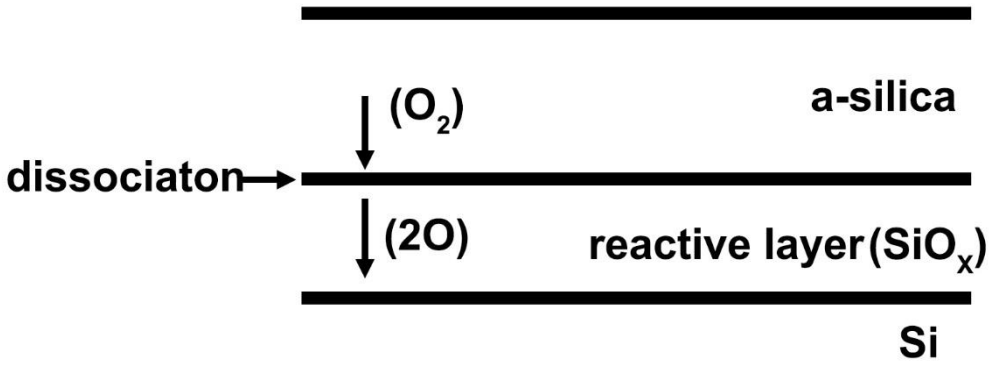

Fig. 60 Schematic illustration of the diffusion process at Si/oxide interface using a reaction layer model.

Fig. 60 is an illustration of the reaction layer that sits in between the base material (Si) and the oxide layer (silica). After oxygen molecules permeate through the oxide layer and reach the outer surface of the reaction layer, they dissociate, and oxygen atoms were incorporated into the atomic network of the reaction layer, which is the immediate product of oxidation. They are typically oxygen deficient, allowing oxygen atoms to jump through the defects and continue their diffusion to reach the base material. One of the most important characteristic features of the reaction layer is that it is “opaque” to oxygen molecules. To react with the base material, the oxygen molecules must break into atoms in order to reach the inner surface of the reaction layer. The thickness of this layer is typically several nanometers in the case of silicon oxidation. The existence of such reaction layer could be partially verified by the TEM image illustrating the microstructure of the interface. For example, in Fig. 30a, which is the TEM image of the interface between the oxide layer and bottom layer in $Hf_7B_{23}Si_{22}C_6N_{40}$ film annealed to 1400 °C in air, HfO_2 nuclei denoted as N1 and N2 were

actually located several nanometers below the interface. It is very likely that atomic oxygen has diffused past the interface to form HfO_2.

As discussed earlier, Si_3N_4 is harder to be oxidized, compared to HfN, HfB_2 and BN. However, this did not cause partial oxidation in $Hf_7B_{23}Si_{22}C_6N_{40}$ films. We propose that it is because the immediate oxidation product in the reaction layer can effectively incorporate atomic oxygen during the thermal oxidation of $Hf_7B_{23}Si_{22}C_6N_{40}$ films, thanks to the excessive boron content (HfB_2 and BN) easily being oxidized into B_2O_3. However, in films with higher silicon vs boron ratio, the reaction layer cannot limit the migration of oxygen through network diffusing, causing high concentration of oxygen at the inner surface of the reaction layer. These oxygen atoms can easily cause preferential oxidation of hafnium and jump through the grain boundaries into deeper part of the film.

When comparing the microstructure of the interface between the oxide layer and bottom layer illustrated in Figs. 30a and 30b, it is easy to conclude that the microstructure of the bottom layer has a significant impact. When the bottom layer was still amorphous, the interface was smooth and clear. It is because the oxidation happened by breaking the amorphous atomic network and as a result, the bottom layer was oxidized as a whole. On the other hand, when the bottom layer was a polycrystalline structure, the oxidation happened by oxidizing different crystalline structures individually. It created local oxidation rate variation since the oxidation of certain crystalline structures was slower compared to the others, as discussed earlier. As a result, it created a rough interface. This rough interface effectively extends the

reactive surface area, allowing oxygens to attack the bottom layer at multiple angles. We propose that it is the ultimate reason behind the accelerated oxidation of $Hf_7B_{23}Si_{22}C_6N_{40}$ films at temperatures higher than 1500 °C.

If the film can remain thermally stable and maintain the original amorphous structure, the oxidation rate will be uniform across the whole interface and the interface will be smooth, which help reduce the oxidation rate. Also, the immediate oxidation products at the interface have to create an atomic network that could incorporate as much as oxygen instead of generating defects. The oxide layer has to cover the whole interface continuously to provide full protection. Among the films discussed earlier, $Hf_6B_{21}Si_{19}C_4N_{47}$ film fits the description the best and we proposed that it is the film with the best oxidation resistance.

Chapter 5

JOURNAL PUBLICATIONS & FUTURE WORK

Part of the results of this research has been published in three following journal papers:

- Shen, Y., Jiang, JC., Zeman, P., Šímová, V., Vlček, J. & Meletis, E.I. Microstructure evolution in amorphous Hf-Si-B-C-N high temperature resistant coatings after annealing to 1500 ˚C in air. *Scientific Reports* **9**, 3603 (2019).
- Šímová, V., Vlček, J., Zuzjaková, Š., Houška, J., Shen, Y., Jiang, JC., Meletis, E.I. & Peřina, V. Magnetron sputtered Hf-B-Si-C-N films with controlled electrical conductivity and optical transparency, with ultra high oxidation resistance. *Thin Solid Films* **653**, 333-340 (2018).
- Zeman, P., Zuzjaková, Š., Čerstvý, R., Houška, J., Shen, Y., Todt, J., Jiang, JC., Daniel, R., Keckes, J., Meletis, E.I. & Vlček, J. Extraordinary high-temperature behavior of electrically conductive $Hf_7B_{23}Si_{22}C_6N_{40}$ ceramic film. *Surf. Coat. Technol.* **391**, 125686 (2020).

The oxidation resistance of $Hf_7B_{23}Si_{22}C_6N_{40}$ and $Hf_6B_{21}Si_{19}C_4N_{47}$ films, together with other properties, was thoroughly discussed in these papers, the oxidation resistance mechanism of other films will be discussed in other papers in the future.

Based on the discussion on the oxidation resistance mechanism of Hf-B-Si-(RE)-C-N coatings annealed to high temperatures, future development of this type of coatings will focus on the following aspects: first, the thermal stability needs to be further

improved. Amorphous coatings with great thermal stability have exhibited great oxidation resistance, as demonstrated by the thermal oxidation of $Hf_6B_{21}Si_{19}C_4N_{47}$ film. Furthermore, fine tuning of silicon vs boron ratio is needed to improve the oxidation resistance. Finally, the options to add rare earth elements should be further explored and new rare earth elements should be considered.

References

[1] Mitterer, C. Borides in thin film technology. *J. Solid State Chem.* **133**, 279-291 (1997).

[2] Fahrenholtz, W.G., Hilmas, G.E., Talmy, I.J. & Zaykoski, J.A. Refractory diborides of zirconium and hafnium. *J. Am. Ceram. Soc.* **90**, 1347–1364 (2007).

[3] Wuchina, E., Opila, E., Opeka, M., Fahrenholtz, W. & Talmy, I. UHTCs: ultra-high temperature ceramic materials for extreme environment applications. *Electrochem. Soc. Interface* **16**, 30-36 (2007).

[4] Fahrenholtz, W.G. & Hilmas, G.E. Ultra-high temperature ceramics: materials for extreme environment. *Scr. Mater.* **129**, 94-99 (2017).

[5] Monteverde, F., Bellosi, A. & Scatteia, L. Processing and properties of ultra-high temperature ceramics for space applications. *Mater. Sci. Eng., A* **485**, 415-421 (2008).

[6] Ghosh, D. & Subhash, G. Recent progress in $Zr(Hf)B_2$ based ultrahigh temperature ceramics in *Handbook of Advanced Ceramics (2nd Edition), Materials, Applications, Processing, and Properties* (ed. Somiya, S.) 267-269 (Academic Press 2013).

[7] Zapata-Solvas, E., Jayaseelan, D.D., Lin, H.T., Brown, P. & Lee, W.E. Mechanical properties of ZrB_2- and HfB_2- based ultra-high temperature ceramics fabricated by spark plasma sintering. *J. Eur. Ceram. Soc.* **33**, 1373-1386 (2013).

[8] Opeka, M.M., Talmy, I.G., Wuchina, E.J., Zaykoski, J.A. & Causey, S.J. Mechanical, thermal, and oxidation properties of refractory hafnium and

zirconium compounds. *J. Eur. Ceram. Soc.* **19**, 2405–2414 (1999).

[9] Levine, S.R., et al. Evaluation of ultra-high temperature ceramics for aeropropulsion use. *J. Eur. Ceram. Soc.* **22**, 2757-2767 (2002).

[10] Opeka, M.M., Talmy, I.G. & Zaykoski, J.A. Oxidation-based materials selection for 2000°C+ hypersonic aerosurfaces: theoretical considerations and historical experience. *J. Mater. Sci.* **9**, 5887–5904 (2004).

[11] Menteverde, F. & Bellosi, A. The resistance to oxidation of an HfB_2-SiC composite. *J. Euro. Ceram. Soc.* **25**, 1025-1031 (2008).

[12] Carney, C.M. Oxidation resistance of hafnium diboride-silicon carbide from 1400 to 2000°C. *J. Mater. Sci.* **44**, 5673–5681 (2009).

[13] Carney, C.M., Mogilvesky, P. & Parthasarathy, T.A. Oxidation behavior of zirconium diboride silicon carbide produced by the spark plasma sintering method. *J. Am. Ceram. Soc.* **92**, 2046–2052 (2009).

[14] Wuchina, E. *et al.* Designing for ultra-high temperature applications: the mechanical and thermal properties of HfB_2, HfC_x, HfN_x and αHf. *J. Mater. Sci.* **39**, 5939-5949 (2004).

[15] Opila, E., Levine, S. & Lorincz, J. Oxidation of ZrB_2- and HfB_2-based ultra-high temperature ceramics: effect of Ta additions. *J. Mater. Sci.* **39**, 5969–5977 (2004).

[16] Menteverde, F. Progress in Fabrication of Ultra-high temperature Ceramics: “in situ” synthesis, microstructure and properties of a reactive hot-pressed HfB_2-SiC composite. *Comp. Sci. Tech.* **65**, 1869-1879 (2005).

[17] Rezaie, A., Fahrenholtz, W.G. & Hilmas, G.E. Evaluation of structure during oxidation of zirconium diboride-silicon carbide in air up to 1500 °C. *J. Eur. Ceram. Soc.* **27**, 2495-2501 (2007).

[18] Monteverde, F. The thermal stability in air of hot-pressed diboride matrix composites for uses at ultra-high temperatures. *Corro. Sci.* **47**, 2020-2033 (2005).

[19] Mallik, M., Ray, K.K. & Mitra, R. Oxidation behavior of hot pressed ZrB_2-SiC and HfB_2-SiC composites. *J. Eur. Ceram. Soc.* **31**, 199-215 (2011).

[20] Opila, E.J. & Hann, R. Paralinear oxidation of CVD SiC in water vapor. *J. Am. Ceram. Soc.* **80**, 197-205 (1997).

[21] Opila, E.J. Variation in oxidation rate of silicon carbide with water-vapor pressure. *J. Am. Ceram. Soc.* **82**, 625-636 (1999).

[22] Opila, E.J. Oxidation and volatilization of silica formers in Water Vapor. *J. Am. Ceram. Soc.* **86**, 1238-1248 (2003).

[23] Tripp, W.C. & Graham, H.C Thermogravimetric study of the oxidation of ZrB_2 in the temperature range of 800 °C to 1500 °C. *J. Electrochem. Soc.* **118**, 1195-1199 (1971).

[24] Parthasarathy, T.A., Rapp, R.A., Opeka, M. & Cinibulk, M.K. Modeling oxidation kinetics of SiC-containing refractory diborides. *J. Am. Ceram. Soc.* **95**, 338-349 (2012).

[25] Carney, C.M., Parthasarathy, T.A. & Cinibulk, M.K. Oxidation resistance of hafnium diboride ceramics with additions of silicon carbide and tungsten boride or tungsten carbide. *J. Am. Ceram. Soc.* **94**, 2600-2607 (2011).

[26] Eakins, E., Jayaseelan, D.D. & Lee, W.E. Toward oxidation-resistant ZrB_2-SiC ultra high temperature ceramics. *Metall. Mater. Trans. A* **42**, 878-887 (2011).

[27] Zhang, S.C., Hilmas, G.E. & Fahrenholtz, W.G. Improved oxidation resistance of zirconium dibordie by tungsten carbide additions. *J. Am. Ceram. Soc.* **91**, 3530-3535 (2008).

[28] Zhang, X., Hu, P., Han, J., Xu, L. & Meng, S. The addition of lanthanum hexaboride to zircornium diboride for improved oxidation resistance. *Scr. Mater.* **57**, 1036-1039 (2007).

[29] Jayaseelan, D.D., Zapata-Solvas, E., Brown, P. and Lee, W.E. *In situ* formation of oxidation resistant refractory coatings on SiC-reinforced ZrB_2 ultra high temperature ceramics. *J. Am. Ceram. Soc.* **95**, 1247-1254 (2012).

[30] Guo, W., Vleugels, J., Zhang, G., Wang, P. & Van der Biest, O. Effects of Re_2O_3 (Re=La, Nb, Y and Yb) in hot-pressed ZrB_2-SiC ceramics. *J. Euro. Ceram. Soc.* 29, 3063-3068 (2009).

[31] Zhang, X., Li, X., Han, J., Han, W. & Hong, C. Effects of Y_2O_3 on microstructure and mechanical properties of ZrB_2-SiC ceramics. *J. Alloys Compd.* **465**, 506-511 (2008).

[32] Han, J., Hu, P., Zhang, X., Meng, S. & Han, W. Oxidation-resistant ZrB_2-SiC composites at 2200℃. *Compos. Sci. Technol.* **68**, 799-806 (2008).

[33] Corral, E.L. & Loehman, R.E. Ultra-high temperature ceramic coatings for oxidation protection of carbon-carbon composites. *J. Am. Ceram. Soc.* **91**, 1495-1502 (2008).

[34] Lee, K. N., Fox, D. S. & Bansal, N. P. Rare earth silicate environmental barrier coatings for SiC/SiC composites and Si_3N_4 ceramics. *J. Eur. Ceram. Soc.* **25**, 1705-1715 (2005).

[35] Al Nasiri, N., Patra, N., Horlait, D., Jayaseelan, D. D. & Lee, W. E. Thermal properties of rare-earth monosilicates for EBC on Si-based ceramic composites. *J. Am. Ceram. Soc.* **99**, 589-596 (2016).

[36] Xu, Y., Hu, X., Xu, F. & Li, K. Rare earth silicate environmental barrier coatings: present status and prospective. *Ceram. Int.* **43**, 5847-5855 (2017).

[37] Boakye, E.E., Mogilevsky, P., Hay, R.S. & Cinibulk M.K. Rare earth disilicates as oxidation resistant fiber coatings for silicon carbide ceramic-matrix composites. *J. Am. Ceram. Soc.* **94**, 1716-1724 (2011).

[38] Tian Z. *et al.* Theoretical and experimental determination of the major thermo-mechanical properties of RE_2SiO_5 (RE=Tb, Dy, Ho, Er, Tm, Yb, Lu and Y) for environmental and thermal barrier coatings applications. *J. Euro. Ceram. Soc.* **36**, 189-202 (2016).

[39] Kohout, J. *et al.* Hard multifunctional Hf–B–Si–C films prepared by pulsed magnetron sputtering. *Surf. Coat. Technol.* **257**, 301-307 (2014).

[40] Zhang, M.H. *et al.* Effect of the Si content on the microstructure of hard, multifunctional Hf-B-Si-C films prepared by pulsed magnetron sputtering. *Appl. Surf. Sci.* **357**, 1343-1354 (2015).

[41] Čapek, J. *et al.* Effect of the gas mixture composition on high-temperature behavior of magnetron sputtered Si-B-C-N coatings. *Surf. Coat. Technol.* **203**,

466–469 (2008).

[42] Kalaš, J. *et al.* High-temperature stability of the mechanical and optical properties of Si-B-C-N films prepared by magnetron sputtering. *Thin Solid Films* **518**, 174–179 (2009).

[43] Zeman, P., Čapek, J., Čerstvý, R. & Vlček, J. Thermal stability of magnetron sputtered Si-B-C-N materials at temperatures up to 1700°C. *Thin Solid Films* **519**, 306–311 (2010).

[44] Vlček, J. *et al.* Pulsed reactive magnetron sputtering of high-temperature Si–B–C–N films with high optical transparency. *Surf. Coat. Technol.* **226**, 34-39 (2013).

[45] He, J. *et al.* Microstructure characterization of high-temperature, oxidation resistant Si-B-C-N films. *Thin Solid Films* **542**, 167-173 (2013).

[46] Zeman, P. *et al.* Superior high-temperature oxidation resistance of magnetron sputtered Hf–B–Si–C–N film. *Ceram. Int.* **42**, 4853-4859 (2016).

[47] Zhang, M.H. *et al.* Study of the high-temperature oxidation resistance mechanism of magnetron sputtered $Hf_7B_{23}Si_{17}C_4N_{45}$ film. *J. Vac. Sci. Technol., A* **36**, 021505 (2018).

[48] Voorhees, P.W. Ostwald ripening of two-phase mixtures. *Annu Rev. Mater. Sci.* 22, 197-215 (1992).

[49] Yao, J.H., Elder, K.R., Guo, H. & Grant M. Theory and simulation of Ostwald ripening *Phys. Rev. B* **47**, 14110-14125 (1993).

[50] Madras, G. & McCoy, B.J. Distribution kinetics of Ostwald ripening at large

volume fraction and with coalescence. *J. Colloid Interface Sci.* **261**, 423-433 (2003).

[51] Zhao, X. & Vanderbilt, D. First-principle study of structural, vibrational, and lattice dielectric properties of hafnium oxide. *Phys. Rev. B* **65**, 233106 (2002).

[52] Wang, J., Li, H.P. & Stevens R. Hafnia and hafnia-toughened ceramics. *J. Mater. Sci.* **27**, 5397-5430 (1992).

[53] Deal, B.E. & Grove, A.S. General relationship for the thermal oxidation of silicon. *J. Appl. Phys.* **36**, 3770-3738 (1965).

[54] Massoud, H.M., Plummer, J.D. & Irene, E.A. Thermal oxidation of silicon in dry oxygen growth-rate enhancement in the thin regime: I. Experiment results. *J. Electrochem. Soc.* **132**, 2685-2693 (1985).

[55] Massoud, H.M., Plummer, J.D. & Irene, E.A. Thermal oxidation of silicon in dry oxygen growth-rate enhancement in the thin regime: II. Physical Mechanism. *J. Electrochem. Soc.* **132**, 2693-2700 (1985).

[56] Ogbuji, L.U.J.T. & Opila E.J. A comparison of the oxidation kinetics of SiC and Si_3N_4. *J. Electrochem. Soc.* **142**, 925-930 (1995).

[57] Šímová, V. *et al.* Magnetron sputtered Hf-B-Si-C-N films with controlled electrical conductivity and optical transparency, with ultra high oxidation resistance. *Thin Solid Films* **653**, 333-340 (2018).

[58] Mukhopadyay, A.B., Sanz, J.F. & Musgrave, C.B. First-principle calculations of structure and electronic properties of monoclinic hafnia surfaces. *Phys. Rev. B* **73**, 115330 (2006).

[59] Musil, J. Hard nanocomposite coatings: Thermal stability, oxidation resistance and toughness. *Surf. Coat. Technol.* **207**, 50-65 (2012).

[60] Musil, J., Zeman, P. & Baroch, P. Hard nanocomposite coatings in *Comprehensive Materials Processing* **4**, (ed. Hashmi, S.) 325-353 (Elsevier Ltd. 2014).

[61] Houška, J. *et al.* Dependence of characteristics of MSiBCN (M=Ti, Zr, Hf) on the choice of metal element: Experimental and ab-initio study. *Thin Solid Films* **616**, 359-365 (2016).

[62] Ohtaka, O., Fukui, H., Kunisada, T. & Fujisawa, H. Phase relations and volume change of hafnia under high pressure and high temperature. *J. Am. Ceram. Soc.* **84**, 1369-1373 (2001).

[63] Ushakov, S., Navrotsky, A., Hong, Q. & van de Walle. A. Carbides and nitrides of zirconium and hafnium. *Materials (Basel, Switzerland)* **12**, 2728 (2019).

[64] Binder, S. *et al.* Phase equilibria in the systems Ti-C-N, Zr-C-N and Hf-C-N. *J. Alloys Compd.* **217**, 128-136 (1995.)

[65] Humphrey, G. Heats of formation of hafnium oxide and hafnium nitride. *J. Am. Ceram. Soc.* **75**, 2806-2807 (1953).

[66] Liang, J., Topor, L., Navrotsky, A., & Mitomo, M. Silicon nitride: Enthalpy of formation of the α- and β-polymorphs and the effect of C and O impurities. *J. Mater. Res.* **14**, 1959-1968 (1999).

[67] Suni, I., Sigurd, D., Ho, K. & Nicolet. M-A. Thermal oxidation of reactive sputtered titanium nitride and hafnium nitride films. *J. Electrochem. Soc.* **130**

1210 (1983).

[68] Lee., T.A. & Navrotsky, A. Enthalpy of formation of cubic yttria-stabilized hafnia. *J. Mater. Res.* **19**, 1855-1861 (2004).

[69] Stacy, D.W. & Wilder D.R. The yttria-hafnia system. *J. Am. Ceram. Soc.* **58**, 285-288 (1975).

[70] Duwez, P., Brown Jr, F.H. & Odell, F. The zirconia-yttria system *J. Electrochem. Soc.* **98**, 356 (1951).

[71] Li, C. *et al.* Effect of Y doping on microstructure and thermophysical properties of yttria stabilized hafnia ceramics. *Ceram. Int.* **44**, 18213-18221 (2018).

[72] Roy, C.K., Noor-A-Alarm, M., Choudhuri, A.R. & Ramana, C.V. Synthesis and microstructure of Gd_2O_3-doped HfO_2 ceramics. *Ceram. Int.* **38**, 1801-1806 (2012)

[73] Andrievskaya, E.R. Phase equilibria in the refractory oxide systems of zirconia, hafnia and yttria with rare-earth oxides. *J. Eur. Ceram. Soc.* **28**, 2363-2388 (2008).

[74] Glushkova, V.B., Hanic, F. & Sazonova, L.V. Lattice parameters of cubic solid solutions in the systems uR2O3-(1-u)MO2. *Ceram. Int.* **11**, 137 (1985).

[75] Natalie, F. et al. Rare earth mononitrides. *Prog. Mater. Sci.* **58**, 1316-1360 (2013).

[76] Wu, Z., Qi, Z., Zhang, D. & Wang, Z. Evolution of the microstructure and oxidation resistance in co-sputtered Zr–Y–N coatings. *Appl. Surf. Sci.* **321**, 268-274 (2014).

[77] Musil, J. & Poláková, H. Hard nanocomposite Zr–Y–N coatings, correlation between hardness and structure. *Surf. Coat. Technol.* **127**, 99-106 (2000).

[78] Courtright, E., Prater, J., Henager, C. & Greenwell, E. WL-TR-91-4006: Oxygen Permeability for Selected Ceramic Oxides in the Range 1200 C - 1700 C. (1991).

[79] Lamkin, M.A. & Riley, F.L. Oxygen mobility in silicon dioxide and silicate glasses: a review. *J. Eur. Ceram. Soc.* **10**, 347-367 (1992).

[80] Mott, N.F., Rigo, S., Rochet, F. & Stoneham, A.M. Oxidation of silicon. *Philos. Mag. B* **60**, 189-212 (1989).

[81] Stoneham, A.M., Grovenor, C.R.M & Cerezo, A. Oxidation and structure of the silicon/oxide interface. *Philos. Mag. B* **55**, 201-210 (1987)